

Saturn's upper atmosphere during the Voyager era: Reanalysis and modeling of the UVS occultations

Ronald J. Vervack, Jr.

*The Johns Hopkins University Applied Physics Laboratory
11100 Johns Hopkins Road
Laurel, MD 20723-6099 (U.S.A.)*

Julianne I. Moses

*Space Science Institute
4750 Walnut Street
Suite 205
Boulder, CO 80301 (U.S.A.)*

Copyright © 2014 Ronald J. Vervack, Jr.

Number of pages: 104

Number of tables: 4

Number of figures: 18

Proposed Running Head:

Saturn's upper atmosphere during the Voyager era

Please send Editorial Correspondence to:

Ronald J. Vervack, Jr.

The Johns Hopkins University

Applied Physics Laboratory

11100 Johns Hopkins Road

Laurel, MD 20723-6099, USA.

Email: Ron.Vervack@jhuapl.edu

Phone: (443) 778-8221

Fax: (443) 778-1641

ABSTRACT

The Voyager 1 and 2 Ultraviolet Spectrometer (UVS) solar and stellar occultation dataset represents one of the primary, pre-Cassini sources of information that we have on the neutral upper atmosphere of Saturn. Despite its importance, however, the full set of occultations has never received a consistent, nor complete, analysis, and the results derived from the initial analyses over thirty years ago left questions about the temperature and density profiles unanswered. We have reanalyzed all six of the UVS occultations (three solar and three stellar) to provide an up-to-date, pre-Cassini view of Saturn's upper atmosphere. From the Voyager UVS data, we have determined vertical profiles for H_2 , H , CH_4 , C_2H_2 , C_2H_4 , and C_2H_6 , as well as temperature. Our analysis also provides explanations for the two different thermospheric temperatures derived in earlier analyses (400-450 K versus 800 K) and for the unusual shape of the total density profile noted by Hubbard et al. (1997). Aside from inverting the occultation data to retrieve densities and temperatures, we have investigated the atmospheric structure through a series of photochemical models to infer the strength of atmospheric mixing and other physical and chemical properties of Saturn's mesopause region during the Voyager flybys. We find that the data exhibit considerable variability in the vertical profiles for methane, suggesting variations in vertical winds or the eddy diffusion coefficient as a function of latitude and/or time in Saturn's upper atmosphere. The results of our reanalysis will provide a useful baseline for interpreting new data from Cassini, particularly in the context of change over the past three decades.

Keywords: Saturn, Atmosphere; Occultations; Aeronomy; Atmospheres, Structure; Ultraviolet Observations

1 Introduction

The Voyager 1 and 2 spacecraft encountered the Saturn system during November 1980 and August 1981, respectively. During these encounters, the Ultraviolet Spectrometer (UVS) on the two spacecraft performed six occultation experiments at Saturn. Voyager 1 carried out ingress and egress solar occultations and an egress stellar occultation of the star ι Herculis, while Voyager 2 performed an ingress solar occultation and both an ingress and egress occultation of the star δ Scorpii. The geometry of these occultations is summarized in Fig. 1 and Table 1.

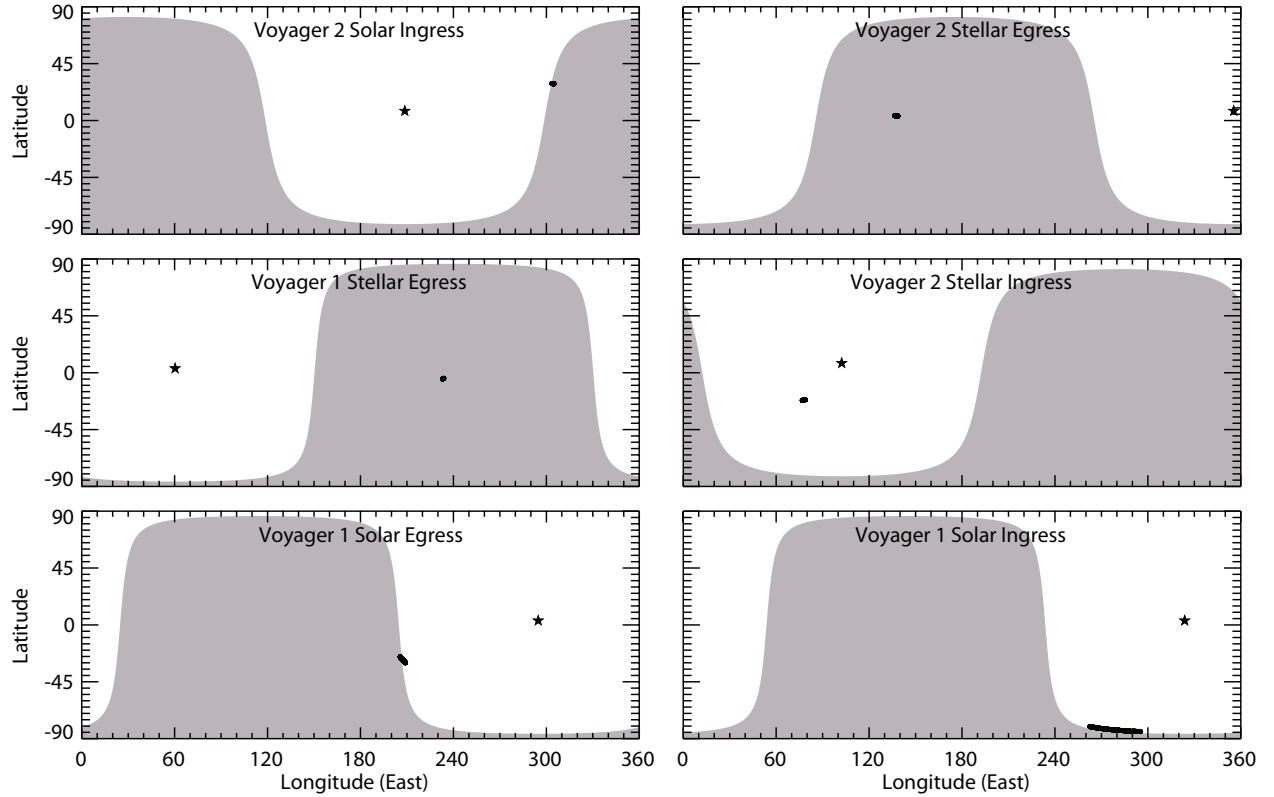


Fig. 1. Geometry of the six Voyager 1 and 2 UVS Saturn occultations. The planetocentric latitude and longitude of the tangent point (the point of closest approach) of each observed spectrum is plotted as a circle, resulting in a line spanning the range of latitude and longitude probed during a given occultation. The subsolar point is indicated by a star in each panel, and the shaded region indicates the night side of Saturn. For most occultations, the range probed is small, but owing to the rapid trajectory changes during the Voyager 1 solar occultations, the ranges are larger. Of note is the Voyager 2 stellar ingress, which is the only occultation that occurred completely on the day side of Saturn.

Table 1

Summary of Geometry for the Voyager 1 and 2 UVS Saturn Occultations

Occultation	UT	Planetocentric	Sub-Solar	Local Time ^a
	Date	Latitude Range	Latitude	
	Time Range	Longitude Range	Longitude	
Voyager 2 solar ingress	26 Aug 1981	29° to 29°	8.1°	8.23 to 8.26
	04:05:49 to 04:07:57	304° to 305°	209°	
Voyager 2 stellar egress	25 Aug 1981	3.5° to 3.9°	8.1°	9.60 to 9.66
	23:44:17 to 23:48:21	137° to 139°	355°	
Voyager 1 stellar egress	12 Nov 1980	-5.0° to -4.5°	3.9°	10.55 to 10.57
	22:58:09 to 23:00:14	233° to 233°	60°	
Voyager 2 stellar ingress	25 Aug 1981	-21.4° to -21.9°	8.1°	4.62 to 4.68
	20:34:15 to 20:38:21	77° to 79°	102°	
Voyager 1 solar egress	13 Nov 1980	-30° to -25°	3.9°	2.72 to 2.82
	02:39:34 to 02:44:46	206° to 209°	295°	
Voyager 1 solar ingress	13 Nov 1980	-84° to -80°	3.9°	3.55 to 4.53
	01:47:57 to 01:53:21	262° to 295°	324°	

^a Local time is defined using a Saturn rotational period of 10.76 hours (i.e., “noon” is 5.38 and “midnight” is 10.76).

The UVS occultation data consist of spectra taken before and during atmospheric attenuation, from which the line-of-sight optical depth can be determined. From the wavelength and altitude variation of this optical depth information, it is possible to infer both the densities of the absorbing species and temperature information. The early analyses of the occultation data were reported by Broadfoot et al. (1981a) and Sandel et al. (1982b). These analyses were followed by the more in-depth work of Festou and Atreya (1982) and Smith et al. (1983).

Although the above analyses provided some information on the density profiles of H_2 and CH_4 , a disagreement in the value of the thermospheric temperature has been the more profound result. The analyses of Broadfoot et al. (1981a) and Festou and Atreya (1982) inferred a temperature of 800–850 K, while those of Sandel et al. (1982b) and Smith et al. (1983) found a value between 400–450 K. Currently, the lower value is favored, particularly in light of the Cassini results (Shemansky and Liu, 2012; Koskinen et al., 2013); however, the discrepancy has never been satisfactorily explained and is puzzling given that it arises from analysis of the same data.

Ground-based measurements conducted in the 1990’s have added additional concerns about previous analyses of the UVS Saturn occultations. The occultation of 28 Sgr by Saturn has been analyzed by Hubbard et al. (1997), who find that the total density profile (and, correspondingly, the temperature profile) in Saturn’s mesosphere inferred by Smith et al. (1983) deviates significantly from the profiles derived for Saturn’s mesosphere from ground-based stellar occultations (see Hubbard et al. Figure 13). Because the Hubbard et al. profiles merge well with the profile at lower altitudes derived from the Voyager radio science investigation, and because the lowest 200 km of the UVS profile

exhibits unusual structure compared to the Hubbard et al. results, we suspect a problem likely exists in the older analyses of the UVS data.

Illustrations of the potential significance of reanalyzing the Saturn UVS occultation data are provided by the work of Yelle et al. (1996) and Vervack et al. (2004). These authors reanalyzed the UVS occultations of the star α Leonis by Jupiter and the Sun by Titan. Their results were notably different from those of previous analyses (Broadfoot et al., 1981b; Festou et al., 1981; Smith et al., 1982), particularly regarding the temperatures in the upper atmosphere. Although derived from the same datasets, the improved processing and retrieval techniques utilized by Yelle et al. and Vervack et al., in combination with other measurements (Marten et al., 1994; Hubbard et al., 1995; Liu and Dalgarno, 1996) in the case of Yelle et al., resulted in significantly different temperature structures in both the newer analyses. The large temperature gradient in Jupiter’s lower thermosphere derived by Yelle et al. was subsequently confirmed by the Galileo probe (Seiff et al., 1997), while the Vervack et al. results for Titan were confirmed by Cassini INMS observations (Waite et al., 2004). Furthermore, the newer processing and retrieval techniques have allowed density profiles for additional species to be inferred from the data.

With the results from the Cassini Ultraviolet Imaging Spectrograph (UVIS) stellar and solar occultation data now becoming available (Shemansky and Liu, 2012; Gustin et al., 2012; Koskinen et al., 2013), it would be valuable to compare the state of the atmosphere in the current era with what was observed thirty years ago. The results may help further our understanding of the source of the unexpectedly high temperatures on all the giant planets, the details of the chemistry and dynamics in thermosphere and middle atmosphere of

Saturn, and the response of Saturn’s atmosphere to seasonal radiative forcing.

Deriving improved information on atmospheric structure and composition in Saturn’s upper atmosphere is important for many reasons. The mesopause region probed in the lower portion of the occultations, i.e., the boundary between the middle atmosphere and thermosphere, is a very interesting region from a physical and chemical standpoint. At deeper levels, atmospheric motions act to keep the lower atmosphere well mixed, and the main stratospheric constituents — hydrogen, helium, and methane — have mole fractions that are roughly constant with altitude. The “eddy” diffusion coefficient provides a means for parameterizing the strength of this mixing in one-dimensional models. In the region probed by the UVS occultations, the mean free path of the atmospheric molecules becomes large, and molecular diffusion begins to dominate over eddy diffusion. The pressure level at which the molecular diffusion coefficient equals the eddy diffusion coefficient is termed the “homopause”. Within several scale heights of the homopause, the atmospheric composition varies dramatically with height, as the concentration of each species becomes diffusively controlled and begins to follow its own scale height. Because most atmospheric constituents are heavier than the background H_2 gas, species concentrations drop off sharply near the homopause.

Coincident with the dramatic change in upper-stratospheric composition is a dramatic change in thermal structure, as temperatures switch from being low and nearly isothermal in the middle atmosphere to having a large temperature gradient transitioning into the high-temperature thermosphere. The composition and thermal changes are related: complex hydrocarbons like ethane and acetylene that are produced from methane photochemistry help cool the stratosphere, and that cooling is ineffective once the concentrations

of these species drop off due to molecular diffusion (see Yelle et al., 2001). In addition, local thermodynamic equilibrium breaks down in the low-density, high-altitude regions, and the corresponding less effective cooling through the ro-vibrational bands of the hydrocarbons may contribute to the dramatic temperature increase (e.g., Bézard et al., 1997). Better constraints on the location and properties of the temperature structure in the homopause region would allow investigators to examine the relative role of these two processes. In addition, the location of the homopause influences atmospheric chemistry through pressure-dependent reactions (e.g., Moses et al., 2005), and the UVS occultations help pinpoint the homopause level and thus help constrain the photochemical models. The UVS occultations provide important constraints for theoretical models of middle-atmospheric chemistry, ionospheric chemistry, radiative transport, energy balance, and atmospheric dynamics.

Given the unique insights into physical and chemical processes the Voyager UVS datasets can provide, the improvements in analysis techniques demonstrated by Yelle et al. (1996) and Vervack et al. (2004) (see also Koskinen et al., 2013), and the problems noted by Hubbard et al. (1997), there are a number of reasons to reanalyze the UVS occultations at Saturn. Perhaps the dominant reason, however, is that the full set of six UVS occultations at Saturn has never received a complete and consistent analysis owing to a variety of complicating factors. Therefore, we have revisited the entire Voyager UVS occultation dataset to resolve the outstanding issues. Using the retrieved density and temperature information from our reanalysis, we have also investigated the structure of Saturn's atmosphere through photochemical modeling to provide a more complete picture of Saturn's upper atmosphere during the Voyager 1 and 2 flybys and to set the stage for comparisons of Voyager and Cassini

observations.

2 UVS Occultation Observations and Data Reduction

The theoretical basis for absorptive occultations is the relatively simple Lambert-Beer law,

$$I(\lambda) = I_o(\lambda) e^{-\tau(\lambda)}, \quad (1)$$

where $I(\lambda)$ is the intensity of light at wavelength λ after attenuation by some amount of absorbing material (in our case, the atmosphere of Saturn), $I_o(\lambda)$ is the unattenuated intensity, and $\tau(\lambda)$ is the optical depth of the absorbing material (see Smith and Hunten (1990) for a more detailed discussion of the general theory of absorptive occultations). In the case of each Voyager UVS occultation, the UVS obtained a series of attenuated spectra (referred to by I) as the line of sight to the source — either the Sun or a star — moved through Saturn’s atmosphere. These spectra can be divided by unattenuated reference spectra (referred to by I_o) acquired outside of Saturn’s atmosphere to construct a series of transmission spectra (the ratio I/I_o) that are independent of the absolute UVS calibration. The variation of these transmission spectra with wavelength and altitude can be analyzed to determine the abundance of UV absorbers in Saturn’s upper atmosphere. However, these spectra are the convolution of the transmission of Saturn’s atmosphere with several instrumental and observational effects related to the Voyager UVS. These effects must be removed from the observed spectra before analysis can begin.

2.1 *Description of the UVS*

The Voyager 1 and 2 UVS instruments are compact, Wadsworth-mounted, objective grating spectrometers covering slightly different wavelength ranges: approximately 530–1700 Å for Voyager 1 and 510–1680 Å for Voyager 2. They were designed to cover diagnostic wavelength regions relevant to the major UV absorbers predicted or known to constitute the upper atmospheres of the giant planets and some of their satellites. Detailed information on the design and operation of the UVS may be found in Broadfoot et al. (1977), Broadfoot and Sandel (1977), Vervack (1997), and Vervack et al. (2004).

Light enters the UVS through one of two ports and passes through a mechanical collimator consisting of thirteen baffles before undergoing a single normal incidence reflection from the concave diffraction grating. The airglow port is used to observe extended sources and stars, whereas the occultation port is used to observe the Sun. The reflected light is then simultaneously focused and dispersed onto the detector assembly, where all photons reaching the active area undergo a three-stage process to convert the photon energy to detector counts. Photons are first converted to charge using a semi-transparent photocathode and two microchannel plates (MCP) in series. The UVS can operate in several different MCP gain states to enable it to observe sources over a wide range of intensities. The charge emitted from the MCPs is collected by the detector, which is a self-scanned anode array with 126 active elements spanning a wavelength interval of 9.26 Å each. Finally, the measured charge is converted to detector counts via a low-resolution (3-bit) A-to-D converter.

Several effects related to the UVS design must be considered in the analysis

of UVS occultation spectra. The use of a mechanical collimator leads to only a fraction of the incoming light reaching the grating as the source moves off-axis, and the reduction is described by an instrumental “slit function”. The resolution of UVS spectra varies with the source, being $\sim 30 \text{ \AA}$ for extended (i.e., slit-filling) sources and $\sim 18 \text{ \AA}$ for point sources. The Sun is too large to be a point source but not large enough to be an extended source because it does not fill the slit. The Sun is thus a “finite” source with a spectral resolution that falls between these values. Imperfections in the grating and the collimator result in the scattering of some photons. These “scattered light” photons are not properly focused and result in radiation of wavelength X contaminating the image of the source for wavelength Y and vice versa for all wavelengths. Finally, when the observed source moves off-axis, the nominal wavelength range of the measured spectra shifts because of changes in the incidence angle of the incoming light at the grating. These last two effects are particularly important in interpreting the wavelength-dependent absorption features in the transmission spectra.

2.2 Spectral Processing

Processing of UVS spectra prior to generating the I/I_o spectra requires the removal of several instrumental effects, including anode-to-anode variations in detector sensitivity, the charge-dependent spreading of the MCP-generated electron cloud, and the presence of instrumentally scattered light. For solar occultations the UVS response is nonlinear owing to the high solar intensities and must be corrected for the ratio of I to I_o to be an accurate measure of the atmospheric transmission. Additionally, the even-numbered channels of both

the Voyager 1 and 2 UVS detectors suffer from a problem at high counting rates. The cause is unknown but it results in fewer counts being recorded than should be and the problem can be particularly severe for solar observations. Except for scattered light, all these effects were removed through the use of a detailed model of the UVS detector assembly. Only a brief summary of the processing is provided here; detailed descriptions of the procedures and the detector assembly model may be found in Vervack (1997) and Vervack et al. (2004).

Detector assembly model. In order to relate the number of incoming photons at the grating to the recorded counts on the detector, we have developed a mathematical model of the entire detector assembly operation. This model is based on Monte Carlo methods that realistically simulate the passage of a photon from the triggering event at the MCPs that initiates the electron cascade, the spreading of the resulting electron cloud onto the detector anodes, and the collection and conversion of those electrons to detector counts. The parameters of the model are based on a rigorous study of both laboratory and in-flight measurements. In particular, the model utilizes laboratory measurements of the charge spreading that have not been fully incorporated previously and observations that have revealed changes in the MCP gains in-flight, most likely a result of normal lifetime degradation of the MCPs. The latter effect is particularly severe in the case of the Voyager 1 UVS, owing to the harsh radiation environment suffered during the Jupiter encounter (see Holberg et al., 1982, for a discussion).

For the Voyager 1 egress solar occultation, an intentional mid-occultation change from the low (HVL 2) gain state to the high (HVL 3) gain state made

accurate knowledge of the detector gain particularly important. In the high gain state, solar spectra are sufficiently bright to saturate the UVS at many wavelengths; thus, all the reference I_o spectra and roughly half of the I spectra were obtained in HVL 2. Changing to HVL 3 midway through the occultation after the brightest parts of the solar spectrum were attenuated avoided saturation in all but a few instances at H Lyman α (none in absorption or utilized reference spectra regions) and allowed the occultation to probe deeper into Saturn's atmosphere. To ensure continuity in the transmission spectra with altitude, this change had to be handled carefully.

Fortunately, two types of observations enabled the gains of the MCPs to be inferred in-flight. The UVS can operate in two counting modes: pulse counting in which a single count is recorded when the charge exceeds a single threshold and pulse height (also called pulse integration) in which a series of counting thresholds allows counts to range from 0 to 7. Observations of the stars β Centauri and ϵ Persei in the two counting modes allowed us to pin down the HVL 3 gain across the detector. We note that these stellar observations occurred in 1983 and 1985, so we checked the stability of the UVS by comparing these observations to observations made in 1980 (but only in the normal stellar observation mode of pulse counting). The differences were less than 5%, consistent with the analysis of post-Jupiter stability by Holberg et al. (1982). However, stars are too weak to use the HVL 2 gain, so we used special observations of the Sun to relate the two gain states. In these solar observations, which occurred roughly a month before and after the Saturn occultations, the UVS slit was slewed across the Sun in HVL 2 and then back across the Sun in HVL 3. The HVL 2 gain was determined by iteratively adjusting it until the processed HVL 2 and HVL 3 spectra were as consistent as possible. These

solar observations were also used to make small corrections to the current limiting function of the UVS detectors, necessary because the original function was determined for conditions at Jupiter distances from the Sun.

A final and important element of the detector model is an empirical correction for a problem with the even-numbered anodes of the detector. The problem manifests itself as a reduction in the counts on even-numbered channels when the total signal on the detector exceeds a certain threshold. The primary effect is a factor of two reduction in the number of channels that can be used to study the atmosphere. Although the exact cause of this anomaly is unknown, we were able to use solar calibrations to develop a simple empirical parameterization to correct for the effect and restore the even channels to the appropriate counting levels. This correction is remarkably successful in reproducing the problem, and the first application to Voyager UVS occultation data by Vervack (1997) and Vervack et al. (2004) allowed us to recover the full wavelength resolution of the UVS during the Titan solar occultations. Previous analyses either neglected the even spectral channels or averaged the adjacent odd channels, effectively halving the resolution.

With the above modeling approach we are not able to infer the proper intensity in a channel that is saturated. Fortunately, the only occultation where saturation was an issue was the Voyager 1 solar egress occultation, and the gain change eliminated this concern in all but a small number of unused spectra (see above).

Removal of scattered light. Modeling of scattered light is a difficult task; therefore, the removal of instrumentally scattered light from the spectra was

accomplished through the application of a linear matrix based on laboratory measurements (see Broadfoot et al. (1981b) for a description). However, using in-flight data, we have made minor changes to the matrix that were revealed as necessary in light of our improved processing techniques. These alterations are described by Vervack (1997).

It is important to note that the Monte Carlo model we employ is an iterative forward-model method: we start with a guess at the photon spectrum input to the UVS, generate the resulting counts spectrum via our forward model of the detector system, compare the modeled counts to the observed counts, and finally make changes to the input photon spectra based on the differences. This means the scattered light matrix is applied in the forward direction and adds scattered light to the modeled spectra for comparisons to what is actually observed. The forward scattering matrices are what were measured in the lab pre-flight, and there are potentially issues regarding the accuracy of the inverse versions of these matrices (i.e., the ones that would be applied to remove scattered light from observed spectra) when applied to bright solar observations. The approach we utilize makes use of the preferred matrices to provide the best accuracy in the resulting processed spectra.

The use of this detector model in removing the instrumental effects from UVS data significantly improves the accuracy of the spectral processing. In particular, corrections that have been neglected in the past are now included. The Monte Carlo approach allows for a detailed calculation of the associated uncertainties in the resulting spectra by including the inherent randomness of the charges generated in the MCPs and propagating that randomness through the processing procedure. The resulting dataset of occultations is of higher quality than previously available and is a primary factor in the differences

between our analysis and earlier analyses.

2.3 Generation of Transmission Spectra

Generation of transmission spectra is conceptually simple: we just need to divide the processed I spectra by the I_o spectra. However, because the measured wavelength range and spectral intensity of UVS spectra vary with the position of the source in the slit (see section 2.1), we must account for the effects of the limit cycle (attitude control) motions of the spacecraft. It is therefore critical that the I and I_o spectra be obtained at the same relative position in the UVS slit for the I/I_o spectra to represent the true absorption of Saturn's atmosphere and not the absorption convolved with observational circumstances.

Slit positions are characterized by two quantities: ΔW and ΔL . The primary quantity of importance is ΔW , a measure of position along the width (dispersion) direction, because the two effects of concern are both connected to ΔW . The other position indicator ΔL pertains to the length direction of the slit, and the only effect along the length of the slit is a variation of the detector sensitivity. Because both ΔW and ΔL are relative measures of the source position, it is difficult to impossible to ascertain where along the length direction the source is absolutely positioned. Thus, although variations with ΔL are known to exist, it is generally not possible to correct for them. For the Saturn occultations, the motion in ΔL is small enough that the effects should be minimal, and we have neglected them.

Values of ΔW for each I and I_o spectrum are calculated from the roll, pitch,

and yaw angle information in the engineering telemetry. Reference spectra are then binned using a ΔW step size of 0.001° . This value is large enough to ensure acceptable signal-to-noise in each bin but small enough to be only a fraction of a spectral channel (each channel subtends 0.0286°) so that spectral shifts from bin to bin are minimized. Each bin is normalized by the number of spectra in the bin to generate an average reference I_o spectrum at each bin-center ΔW . Finally, each I spectrum is divided by the appropriate reference spectrum to generate the final I/I_o transmission spectra.

For the final step in generating transmission spectra, the line-of-sight geometry for each spectrum is calculated. Note that we use radius and not altitude because Saturn is not a true ellipsoid but rather has latitudinal variations superimposed on the bulk ellipsoidal surface (Lindal et al., 1985). By providing results as a function of radius, they are independent of any assumptions about the surface shape. To calculate the geometry, we adopt the method described by Nicholson et al. (1990), in which all geometry calculations are performed in a saturnocentric reference frame. This approach allows the motion of the source (Sun or star), Saturn, and the spacecraft to be taken into account in a relatively simple fashion. The necessary vectors are determined using NAIF (Navigation and Ancillary Information Facility) SPICE (Spacecraft Planet Instrument “C-Matrix” Events) library routines obtained from NASA’s Jet Propulsion Laboratory. For each spectrum, the vectors are determined using the ephemeris time of the observation calculated from the spacecraft event time (SCET). All times and vectors are referenced to the J2000 inertial reference frame that is used by the SPICE routines. For details of the method and the calculations, refer to Nicholson et al. (1990) and Vervack (1997), respectively.

The uncertainties in the final light curves are generated by propagating the uncertainties in the measured raw spectra through all the spectral processing steps, reference spectra binning, and transmission spectra generation using the standard methods for propagation of uncertainties as outlined by Bevington and Robinson (1992). They are statistical in nature only (i.e., primarily the result of channel-to-channel and spectrum-to-spectrum counting variations) and do not account for systematic uncertainties that may be associated with certain elements of the processing procedure (e.g., uncertainties in the scattered light matrices are not known). Fortunately, owing to the use of transmission spectra that are a ratio of two spectra, any systematic uncertainties are likely minimized.

3 Retrievals of Density Profiles

Two separate approaches have typically been adopted to infer atmospheric density profiles in previous analyses of UVS occultation data. In the first approach, a physically plausible atmosphere is generated, the transmission spectra that would result from the model are calculated, and adjustments to the atmospheric model are made until the modeled transmission spectra provide the best possible match to the measured spectra. This approach was used in the original Saturn occultation analyses of Smith et al. (1983) and Festou and Atreya (1982), as well as in some modern-day occultation analyses of the giant planets (e.g., Greathouse et al., 2010; Shemansky and Liu, 2012). In the second approach, mathematical inversion techniques are used to obtain direct retrievals of the atmospheric densities from the transmission spectra (e.g., the approach used in the Neptune occultation analysis of Yelle et al.

(1993)). The first “forward-modeling” approach has the advantage that the resulting atmospheric solution is consistent with physical laws, but the computational time can be long if many iterations are required for convergence, and the results are nonunique owing to unconstrained model input parameters. The second “mathematical-inversion” approach is computationally more efficient and provides better uncertainty estimation, but the method relies on mathematical relationships that do not always approximate reality.

In this work, we employ the hybrid approach of Vervack et al. (2004) (see also Koskinen et al., 2013). As in the first method, we use a forward-modeling technique to calculate the transmission spectra, but rather than providing a fixed input atmosphere, we rely on an iterative inversion technique to derive the atmospheric densities directly from the data. The main advantage of this approach is that the transmission spectra can be accurately modeled by including such effects as atmospheric attenuation, wavelength blending (i.e., the measurement of many wavelengths in a single detector channel), and, for solar occultations, the finite size of the Sun in both the I and I_o spectrum *prior* to dividing the two. In contrast, the direct inversion approach requires approximations of these effects (i.e., through parameterizations and cross-section weightings) because the measured I/I_o spectrum that is the starting point of the inversions has the effects already combined and inseparable.

The following discussion tracks that of Vervack et al. (2004) but is provided here in a sufficient amount of detail for a reader to understand how the densities were retrieved. For a more detailed description, see Vervack et al. (2004). We retrieve densities through a two-step process. In the first step, each transmission spectrum is independently fit using the Marquardt-Levenberg minimization technique described by Press et al. (1992) to yield the line-of-sight

column densities. The chi-squared spectral mismatch between the fitted and observed transmission spectra is given by

$$\Delta S = \sum_c \frac{[M(c) - D(c)]^2}{[\sigma_D(c)]^2}, \quad (2)$$

where ΔS is the mismatch function to be minimized, $M(c)$ and $D(c)$ are the values of the model and observed transmission spectra for channel c , $\sigma_D(c)$ is the uncertainty of the observed transmission spectrum for channel c , and the summation is over the c channels of the spectra. Once the spectral mismatch ΔS is minimized, both the column densities and their associated covariance matrix are returned by the Marquardt-Levenberg procedure.

In the second step, the line-of-sight column densities for each species are inverted to yield the vertical number densities using a constrained linear technique similar to that described by Twomey (1977). We employ a second difference smoothness constraint (see Twomey, 1977) to provide a physical continuity to the vertical profiles and assume a spherically symmetric atmosphere with a 5-km radial grid spacing. Linear quadrature is used to describe the variation of the number densities within each layer, and the profile falls off exponentially above the uppermost layer. The assumption of spherical symmetry is reasonably valid despite Saturn's oblateness because the occultations generally probe along lines of constant latitude where the geometry is approximately circular (as opposed to elliptical). The uncertainties associated with the final vertical density profiles are calculated by propagating the column density covariance matrix through the inversion (see Menke, 1989).

Modeling the attenuated I spectrum during the retrieval procedure is a key step in the process. We start with an input solar spectrum, determine the

line-of-sight optical depth τ at each wavelength, and apply Eq. 1 to attenuate the spectrum. The optical depth τ is defined such that

$$\tau(\lambda, r_{pca}) = \sum_i \int_{-\infty}^{\infty} \sigma_i(\lambda, s) n_i(s) ds, \quad (3)$$

where r_{pca} is the radial distance from the center of Saturn to the point of closest approach along the line of sight, $n_i(s)$ is the local number density of species i along the line-of-sight direction (denoted by s with origin at the point r_{pca}), and $\sigma_i(\lambda, s)$ is the total extinction cross section at wavelength λ along the line of sight. In our case, the σ are simply photoabsorption cross sections. The integral in Eq. 3 may be replaced with a summation over the layers j of our atmosphere to give

$$\tau(\lambda, r_{pca}) = \sum_i \sum_{j_{low}}^{j_{max}} [\sigma(\lambda)]_{ij} N_{ij}, \quad (4)$$

where N_{ij} is the column density for species i in layer j . We solve for the column densities directly, so we replace Eq. 4 with

$$\tau(\lambda, r_{pca}) = \sum_i [\sigma(\lambda)]_i N_i, \quad (5)$$

where N_i and $[\sigma(\lambda)]_i$ are the total line-of-sight column density (i.e., the sum of N_{ij} over all j) and the photoabsorption cross section for species i . Although $[\sigma(\lambda)]_i$ should in general be appropriately weighted to account for line-of-sight temperature variations, cross section measurements at temperatures relevant to Saturn's atmosphere over the altitude range of the UVS occultations are few. We therefore use cross sections corresponding to the temperature at the point of closest approach, where the largest relative amount of absorption occurs along the line of sight. Our standard temperature profile (see section 4.1) is used to establish the cross sections to use.

Variations in the temperature profile from occultation to occultation are likely, but the variations in most cross sections with the likely variations in temperature *at a given radius* are small enough that we do not consider them here. A more significant variation with temperature is probable for H₂ absorption near the bottom of the derived profiles where the temperature profile is changing rapidly from the thermospheric value to the mesopause value. However, the majority of the H₂ profile is derived from the region of nearly constant temperature in the thermosphere and therefore is affected only to a small degree. Even at the bottom of the profile, runs assuming fixed temperatures of 100 K and 500 K (bracketing the extremes of thermosphere and mesosphere) yield H₂ retrievals that differ only at the level of 10% or less.

The SC#21REFW reference spectrum of Hinteregger et al. (1981) is used as the input source spectrum in the solar occultation retrievals, taking into account the heliocentric distance of Saturn. Adjustments needed to model the solar spectrum for the actual flyby dates are made using appropriate factors as provided by K. Fukui (personal communication, 1996). Higher resolution spectra are available, but the Hinteregger et al. spectrum was developed for the actual time period covered by the Saturn occultations. It is thus a more accurate representation of the relative flux levels across the wavelength range of the Voyager UVS, which has a more significant effect on the model spectra owing to scattered light than the resolution does. For the stellar occultations, an absolutely calibrated average spectrum of the star obtained from the unattenuated I_o reference spectra region is used for the source spectrum. The sources of the cross sections used in the retrievals are listed in Table 2; note that only some of the species were included in the retrievals (further discussed in section 5.1). Both the source spectra and the cross sections were interpo-

lated (appropriately weighted) onto a 0.5 \AA grid prior to the calculations to ensure a small spacing in the wavelengths of the input spectrum relative to the 9.26 \AA width of the UVS spectral channels. Further details of the construction of both the source spectra and cross section datasets may be found in Vervack (1997).

Table 2

Sources for Photoabsorption Cross Section Data

Species	Source
H ₂ (continuum)	Samson and Haddad (1994); Chan et al. (1992) Ford and Browne (1973); Dalgarno and Allison (1969)
H ₂ (bands)	Yelle et al. (1993)
H	Sadeghpour and Dalgarno (1992); Samson (1966)
CH ₄	Au et al. (1993); Samson et al. (1989); Mount and Moos (1978); Mount et al. (1977)
C ₂ H ₂	Cooper et al. (1995a); Smith et al. (1991); Xia et al. (1991); Suto and Lee (1984)
C ₂ H ₄	Cooper et al. (1995b); Zelikoff and Watanabe (1953)
C ₂ H ₆	Au et al. (1993); Mount and Moos (1978)
C ₄ H ₂ ^a	Okabe (1983)
CH ₃ C ₂ H ^b	Ho et al. (1998)
C ₃ H ₆ ^b	Samson et al. (1962); Orkin et al. (1997)
C ₃ H ₈ ^b	Au et al. (1993)

^a C₄H₂ was included in the Voyager 2 solar ingress and the Voyager 1 solar egress retrievals but profiles were not statistically significant and are not reported.

^b These species were not included in the retrievals but were used in the test discussed in section 5.1 to demonstrate their exclusion.

After attenuation, each I spectrum is degraded to UVS resolution. We account for the UVS optical line shape, the slit function (an improved version for the occultation port determined from a special series of observations), and the limit-cycle-induced spectral shift. For solar occultations, we also account for the finite size of the Sun. After applying these effects to each wavelength of the input spectrum, the resulting spectrum is integrated over the wavelength range of each spectral channel. The I_o spectrum is modeled in the same fashion by degrading the unattenuated source spectrum, and the ratio of the two spectra is taken to yield the transmission spectrum.

The results of our density retrievals for each occultation, along with details particular to a given occultation, are presented below in section 5. In the next section, we discuss the general method we employed for the generation of photochemical models that simulate atmospheric conditions at each occultation location.

4 Forward models

The direct inversion technique has the benefit of providing the best mathematical fit to the data. However, the results can occasionally be unphysical, such as when the derived methane mixing ratio appears to increase with increasing altitude or when the ethane concentration approaches the methane concentration in the lower part of the occultation light curve for some of the noisier occultations (see below). The first situation is unphysical for a methane source from deeper in the atmosphere, and our current understanding of methane photochemistry on Saturn (e.g., Moses et al., 2000, 2005; Ollivier et al., 2000; Dobrijevic et al., 2003; Dobrijevic et al., 2011) precludes the second possibil-

ity. Such problems can be avoided by using a physics-based forward-modeling technique, but the forward models have their own weaknesses, such as being poorly constrained and inherently nonunique. By using a combination of forward modeling and data inversion, we can check for physical consistency and can exploit the strengths of both methods to derive more realistic atmospheric structure information for Saturn. In this section, we add a forward modeling component to the investigation in order to better determine the implications of the UVS occultation results with regard to chemistry and transport in Saturn’s upper atmosphere during the Voyager era.

The goal of the forward modeling is to reproduce the variation of species densities with radius determined from the occultation light curves and density retrievals and to make resulting inferences about chemical and physical processes and properties in the homopause region. The H_2 density profile in Saturn’s atmosphere depends on the temperature structure, mean molecular mass, and gravity variation with radius, none of which are well constrained below the regions probed by the ultraviolet occultations. This is a significant yet underappreciated weakness of forward modeling that may be one cause of the widely varying results on thermospheric temperatures from UVS occultation analyses in the past (cf. Festou and Atreya, 1982; Smith et al., 1983), as we discuss further in section 5.3 (see also Appendix A). Transforming the radius scale to a more meaningful pressure scale for interpreting the underlying chemical and physical processes occurring in the atmosphere is particularly difficult for the oblate giant planets. Saturn’s unusual shape, rapid rotation, strong zonal winds, uncertain radius at any reference pressure level as a function of latitude, and uncertain mean molecular mass variation with altitude complicate the derivation of the gravity and density structure. We often must extrapolate

the densities from the upper troposphere, where the planetary radius, zonal winds, and temperatures are better known (and thus better constrain the density at a particular radius), to the upper stratosphere and thermosphere, where the UVS occultations and ground-based stellar occultations provide information. In the intervening region, temperatures, wind speeds, and other information are uncertain, particularly during the Voyager encounter. The Cassini mission has provided a wealth of information on stratospheric temperatures (e.g., Flasar et al., 2005; Fletcher et al., 2007; Fletcher et al., 2008, 2010; Fouchet et al., 2008; Liming et al., 2008; Li et al., 2013; Guerlet et al., 2009, 2010, 2011; Sinclair et al., 2013, 2014), but the results show significant seasonal and interannual variability, effectively preventing us from using Cassini information to characterize stratospheric temperatures at the time of the Voyager encounter. Moreover, there is still a data gap between the lowest pressure (highest altitude) that the Cassini Composite Infrared Spectrometer (CIRS) data can probe during the limb observations (e.g., Guerlet et al., 2009) and the pressures that the ultraviolet occultations probe.

In any case, many plausible temperature profiles and other model parameters can be considered that reproduce the H_2 density structure derived from the inversion of the UVS occultation data — the forward-modeling solutions are simply nonunique. It is also possible that the H_2 is not in local thermodynamic equilibrium (Shemansky and Liu, 2012), resulting in poorly understood population states that are difficult to model (e.g., Hallett et al., 2005b), affecting the analysis of the occultation light curves in the H_2 Lyman and Werner bands in particular. We develop multiple plausible models for several of the occultations to better illustrate the uncertainties in the forward-modeling technique.

The variation of the hydrocarbon concentrations with radius depends not only

on the background atmospheric structure and H₂ density, but also on chemistry and transport processes. For the forward modeling part of this investigation, we use the Caltech/JPL KINETICS code (Allen et al., 1981) to develop one-dimensional models of photochemistry and diffusion that define the variation of hydrocarbon abundances with altitude on Saturn. The adopted chemistry follows that of Model C of Moses et al. (2005). We keep the models consistent, to the highest extent possible, with Earth-based and spacecraft observations concerning the stratospheric hydrocarbon abundances below the region of sensitivity of the UVS occultations. The key unknown input parameters in the photochemical models for our purposes, aside from some uncertain reaction rate coefficients, are the temperature profile, which controls the density variation with altitude and can affect reaction rates, and the eddy diffusion coefficient profile, which affects the variation of species concentrations (and mean molecular mass) with altitude. Other uncertainties such as the planetary shape and the zonal wind speed and its variation with altitude contribute significant uncertainties to the gravity field and the background atmospheric structure, which can lead to systematic errors in the models. The kinetic reaction rate coefficients, photolysis cross sections, and other chemistry inputs also have some effect on the results, but only for the complex hydrocarbons. Methane itself is controlled mainly by diffusion or vertical transport in this portion of the atmosphere; chemistry has only a minor influence on the CH₄ profile.

We begin the forward modeling by specifying a radius at the 1-bar level and a temperature and mean-molecular-mass profile as a function of pressure from the 1-bar level on up to $\sim 3 \times 10^{-9}$ mbar. The hydrostatic equilibrium equation is then solved to define a background atmospheric grid with full pressure,

temperature, radius, gravity, and density structural information. The gravitational acceleration is determined for a rapidly rotating, fluid planet as described in Lindal et al. (1985). We assume gravitational harmonic coefficients $J_2 = 0.016331$, $J_4 = -0.000914$, and $J_6 = 1.08 \times 10^{-4}$ (Nicholson and Porco, 1988) and consider a latitude-dependent rotation velocity that includes the zonal winds. The latitude-dependent 1-bar radius and cloud-top zonal winds are obtained from W. B. Hubbard (personal communication, 2004), and are based on the Ingersoll et al. (1984) wind fields and an assumption of a strictly barotropic atmosphere, with wind speeds constant on a cylindrical surface aligned with the rotation axis. Table 3 describes the 1-bar radii and rotation rate assumptions for our forward models.

Table 3

Radius and Rotation-Rate Assumptions for Forward Models

	Planetocentric	Assumed Radius	Local Rotation
Occultation	Latitude	at 1 bar (km)	Period (hr)
Voyager 2 solar ingress	29°	58556	10.60
Voyager 2 stellar egress	3.8°	60232	10.18
Voyager 1 stellar egress	-4.8°	60213	10.22
Voyager 2 stellar ingress	-21.5°	59260	10.41
Voyager 1 solar egress	-27°	58771	10.56

Note: Our solution to the hydrostatic equilibrium equation requires knowledge of the local angular velocity (i.e., the angular velocity corresponding to the interior rotation period plus the angular velocity due to the zonal wind). As long as the winds were determined in a consistent manner relative to the assumed interior rotation period, our solution is independent of the exact interior rotation period — it is the local atmospheric rotation period that is used in the equations.

For lack of better information, we assume that the zonal winds derived at the cloud tops are constant with height. Note that this assumption differs from our data inversion described in the previous sections, in which we assume that zonal winds have dropped to zero at these high altitudes, so some differences exist between the density-temperature-radius profiles derived from the forward modeling and inverse retrievals. Hubbard et al. (1997) provide evidence for the zonal winds in the equatorial region being strong up to at least the microbar region. However, recent Cassini and ground-based data show some evidence that Saturn’s zonal thermal wind structure contains vertical shear, especially in the near-equatorial region where there appears to be a kind of ~ 15 -year oscillation similar to the Earth’s semi-annual oscillation (Fouchet et al., 2008; Orton et al., 2008; Liming et al., 2008; Li et al., 2011; Guerlet et al., 2011).

The preliminary background hydrostatic atmosphere is then combined with an eddy diffusion coefficient profile derived from previous photochemical modeling (Moses et al., 2005) and is used to develop a new preliminary photochemical model for the equatorial region. The resulting abundance profiles are used to derive a mean molecular mass profile (see Fig. 2) and a refractivity versus radius profile for comparison with the Hubbard et al. (1997) stellar occultation data (reported for the equatorial region). In the case of a poor fit to the Hubbard et al. refractivity values, the temperature profile is tweaked and the entire process iterated, until the Hubbard et al. refractivity profile in their 60830-61040 km region is reproduced. Note that we elect to compare with the Hubbard et al. refractivity profile rather than their derived temperature profile because of differences in our assumptions about the atmospheric composition and mean molecular mass. At the lower boundary of our model (5 bar), we assume a helium mole fraction of 10%. This value is at the lower

end of the $12(\pm 2)\%$ range derived by Conrath and Gautier (2000) from an analysis of Voyager IRIS spectra but is higher than the combined Voyager IRIS-RSS derivation of $3.4(\pm 2.4)\%$ (Conrath et al., 1984) and higher than the preliminary combined Cassini RSS-CIRS derivation of $\sim 7\%$ (Flasar et al., 2008; Fouchet et al., 2009) or the Hubbard et al. (1997) assumption of 6%. The tropospheric helium abundance on Saturn remains uncertain. Throughout the modeling, we also assume a CH_4 mole fraction of 4.5×10^{-3} (Flasar et al., 2005) at the lower boundary (5 bar) of our models (cf. Fletcher et al., 2009).

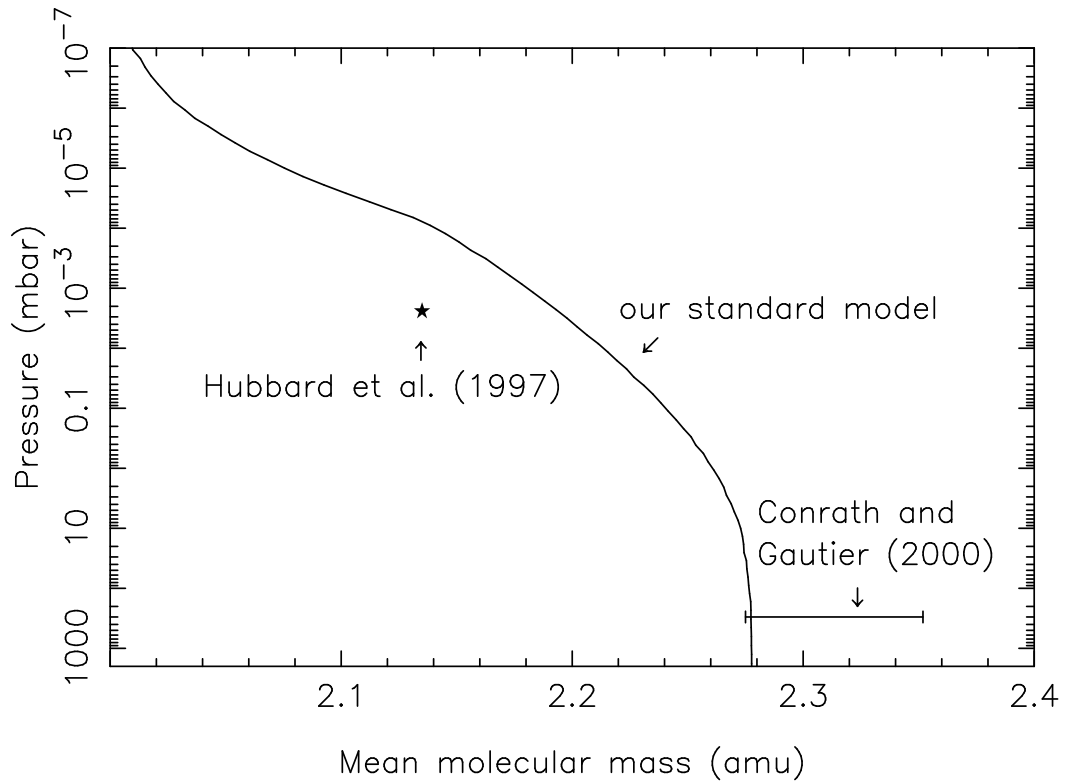


Fig. 2. The mean molecular mass variation with pressure, as derived from our standard photochemistry/diffusion model with an assumed He mole fraction of 10% at the 5-bar lower boundary (solid line), is compared with the Voyager IRIS derivation (range with error bars) of Conrath and Gautier (2000) and the 2.135 amu assumption (star) of Hubbard et al. (1997). Note that although we expect the mean molecular mass to drop off with altitude, the exact profile will depend on uncertain vertical transport parameters.

4.1 Temperature structure adopted in the forward models

The thermal structure of Saturn is well enough understood to define three distinct regions based on the temperature profile: (1) the troposphere, below the temperature minimum at ~ 100 mbar, in which radiative-convective exchange controls the temperatures, (2) the middle atmosphere, between ~ 100 and a few $\times 10^{-5}$ mbar, in which radiative processes control temperatures and in which the atmosphere is stable against convection, and (3) the thermosphere, above a few $\times 10^{-5}$ mbar (but depends on latitude and/or time), in which the temperature begins to increase dramatically with altitude up to a nearly isothermal exospheric region. The heating mechanisms for the thermosphere are currently not well understood (e.g., Yelle and Miller, 2004; Müller-Wodarg et al., 2006; Müller-Wodarg et al., 2012; Smith et al., 2007; Smith and Aylward, 2008). Throughout this paper, we use the term “stratosphere” to refer to the entire middle atmosphere, and the term “mesopause” to refer to an ill-defined region marking the base of the thermosphere.

Saturn’s stratosphere above ~ 0.01 mbar and the thermosphere are difficult regions to access from remote-sensing methods. The three techniques of (1) Earth-based observations of stars being occulted by Saturn (e.g., Hubbard et al., 1997; Cooray et al., 1998; French et al., 1999; Harrington et al., 2010), (2) spacecraft ultraviolet observations of stars or the Sun being occulted by Saturn (e.g., Sandel et al., 1982a; Festou and Atreya, 1982; Smith et al., 1983; Feng, 1991; Feng et al., 2005; Shemansky and Liu, 2012; Koskinen et al., 2013, this work), and (3) observations of the planet’s airglow and auroral emission (e.g., Sandel et al., 1982b; McGrath and Clarke, 1992; Emerich et al., 1993; Geballe et al., 1993; Ben Jaffel et al., 1995; Gérard et al., 1995, 2004;

Gérard et al., 2009; Parkinson et al., 1998; Miller et al., 2000; Hallett et al., 2005a; Melin et al., 2007; Melin et al., 2011; Gustin et al., 2009; Stallard et al., 2012; O’Donoghue et al., 2014) have provided our only constraints on the atmospheric density/temperature structure in Saturn’s thermosphere and mesopause region. However, deriving temperatures and densities from these methods requires several assumptions about atmospheric properties that are not well known. For the forward modeling part of this investigation, we consider the upper atmospheric temperature to be a free parameter, and we adjust the temperature profile until we find a good fit to the H₂ density profile derived from our inversion of the UVS occultation data.

Although we started with temperature profiles consistent with the Lindal et al. (1985) Voyager radio occultation results and/or the Voyager IRIS analysis of Conrath and Gautier (2000), we found that we needed to increase temperatures in the middle atmosphere and/or troposphere in order to match either the Hubbard et al. (1997) refractivity data or the UVS H₂ density inversions (see below), given our assumptions about the 1-bar radius and the mean molecular mass. Our warmer profiles are consistent with the temperatures derived for late spring and early summer latitudes from current-day mid-infrared observations (e.g., Greathouse et al., 2005; Flasar et al., 2005; Fletcher et al., 2007; Guerlet et al., 2009) but are warmer than has been typically assumed or derived from observational analyses from the Voyager era or Infrared Space Observatory (ISO) era (e.g., Lindal et al., 1985; Conrath and Gautier, 2000; Moses et al., 2000; Lellouch et al., 2001). Although our result is dependent on initial assumptions, especially with regard to the 1-bar radius and the helium abundance, we have developed numerous models and covered enough parameter space to form the general conclusion that the colder stratospheric temper-

atures derived from the analysis of the global-average ISO data (Moses et al., 2000; Lellouch et al., 2001) are too cold to be accommodated by our UVS data-model comparisons — the stratosphere at 29° N latitude at the time of the Voyager 2 solar ingress occultation was warmer and more expanded in an average sense than is indicated by the ISO analysis (see the journal supplemental material and section 5.3 for the forward-model profiles). It is difficult to quantify the temperature uncertainty from the forward modeling, but one should not place too much reliance on the actual assumed profile. The “average” temperature below the occultation altitudes needs to be relatively warm to account for the H₂ abundance at large radial distances, but neither the vertical profiles nor the location and temperature of the mesopause are uniquely constrained by the comparisons of our forward models with the UVS data.

5 Results and Discussion: Comparison of Retrievals and Models

In this section we present the results of both our retrievals (data inversions) and our photochemical models (forward models). We begin with the occultation of highest quality, the Voyager 2 solar ingress, and proceed through the occultations in order of decreasing quality. For each occultation, we present density profiles from both the retrievals and models, as well as comparisons of the measured light curves to light curves simulated using both the retrieved and model densities. For each occultation, we discuss the implications and limitations of the comparisons, as well as the details that are particular to each of the occultations.

5.1 *Voyager 2 Solar Ingress*

5.1.1 *Data Retrievals*

Owing to the high signal-to-noise ratio that results from using the Sun as a source and to problems with the Voyager 1 solar occultations (see below), the Voyager 2 solar ingress occultation represents the best dataset available from the Voyager UVS occultations at Saturn, and the profiles are of excellent quality.

Figure 3 shows the density profiles retrieved from the Voyager 2 solar ingress occultation. For clarity, only every other point is shown for H₂ and H. Note that the hydrocarbon profiles were retrieved using a tighter smoothing constraint than was used for the H₂ and H profiles, which explains their smoother nature relative to the profiles for H₂ and H. This smoothing was necessary because of the higher noise levels in the transmission spectra at the wavelengths of hydrocarbon absorption. In this and all similar figures for the other occultations, the error bars on the density profiles represent the one-sigma level.

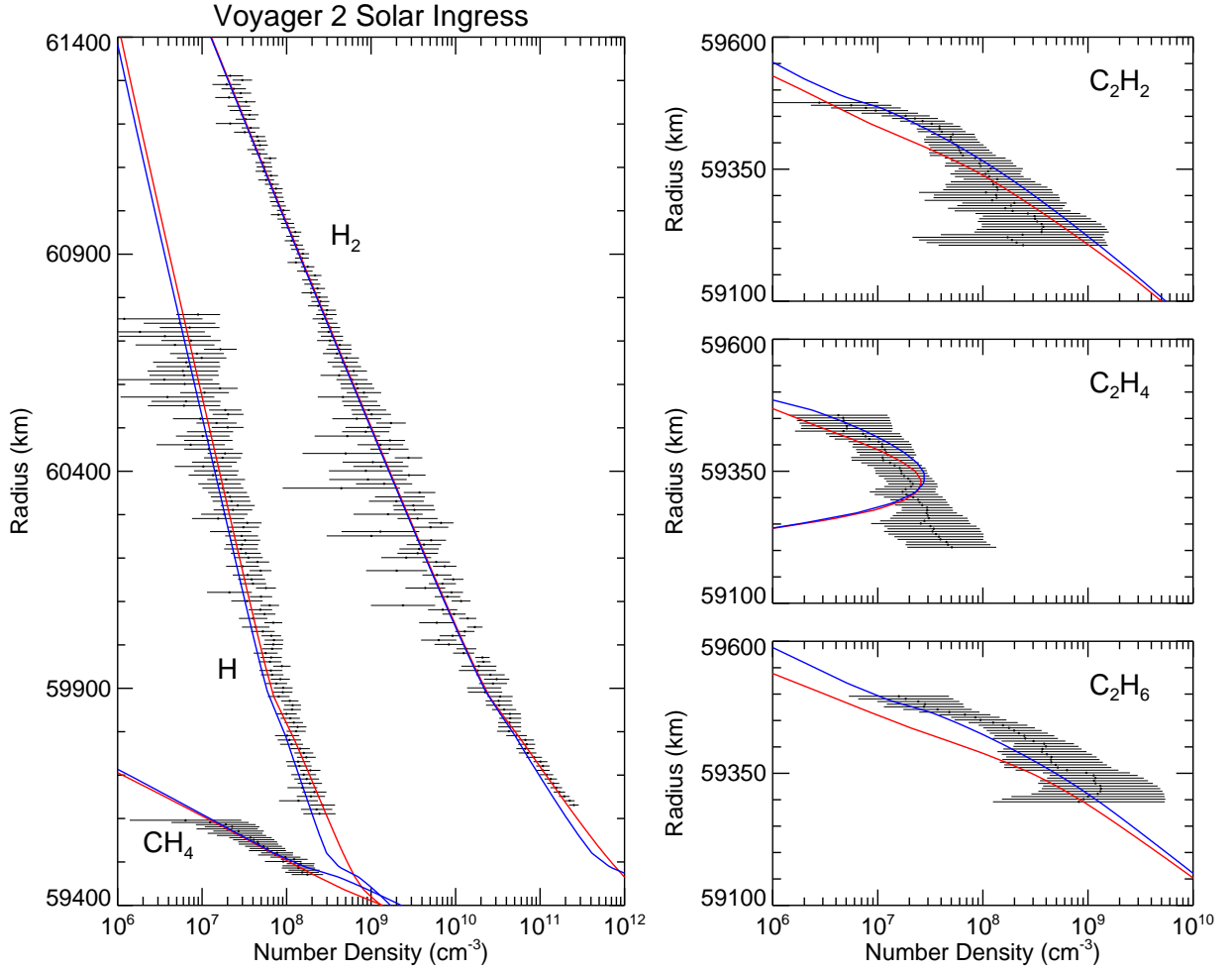


Fig. 3. The density profiles from our standard model (red curve) and “best-fit hydrocarbon model” (blue curve) are compared with the densities retrieved from the data inversions of the Voyager 2 solar ingress occultation at 29° latitude (black symbols, with associated one-sigma uncertainties). The left figure is for H_2 , H , and CH_4 , while the right panels are for C_2H_2 (top), C_2H_4 (middle), and C_2H_6 (bottom). Only every other point is shown for the H_2 and H profiles for clarity.

The jittery nature near the middle of the H_2 profile represents the altitude region where the density information transitions from the H_2 continuum to the H_2 bands. Because the continuum region is almost completely absorbed whereas the band region is only beginning to show absorption, the retrieved profile exhibits more variation than at altitudes above and below. This “noisiness” is consistent with the fact that the retrievals at these altitudes are derived from data that are at the extremes of transmission (i.e., either small residuals near complete absorption or small absorptions near complete transmission). Note that the H_2 profile shows just a hint of curvature at the lowest altitudes, indicating that the temperature is changing to smaller values. This result is consistent with the earlier analysis of Smith et al. (1983) and, as we will see in section 5.5, with the model of Hubbard et al. (1997).

Figure 4 shows a series of light curves to demonstrate how well the retrieved densities reflect the observed transmission. In each panel, a data light curve representing the uncertainty-weighted average of the light curves probing the specified wavelength range (including shifts induced by ΔW motion) is shown, and the corresponding synthetic light curve generated using the retrieved density profiles is overplotted (light blue curve). The one-sigma uncertainties shown for the data curves represent the simple average uncertainty over the same range rather than the weighted uncertainty. The average uncertainty is used to give the reader a better feel for the uncertainties in the individual light curves that were averaged to generate the shown data curve. The weighted uncertainties would, of course, be smaller. The relatively small size of the uncertainties indicates the high quality of the Voyager 2 solar occultation.

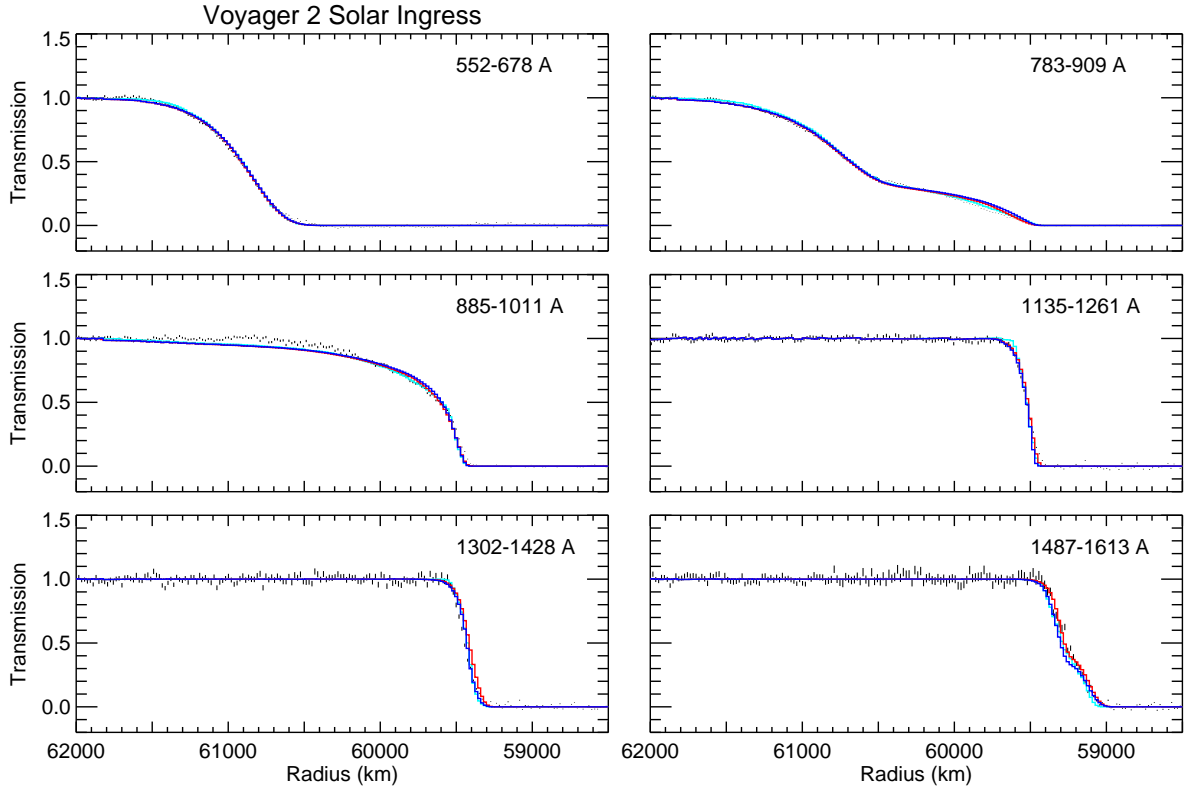


Fig. 4. Light curves from our reanalysis of the Voyager 2 UVS solar ingress occultation (black bars representing the one-sigma uncertainty levels at each point) compared with synthetic light curves generated from our “standard” photochemical model (red) and “best-fit hydrocarbon” model (blue). A synthetic light curve is also shown for the retrieved densities (light blue). These curves are averages of several channels and span the wavelength ranges indicated in each panel (including limit-cycle-induced shifts). Only every third point is shown for clarity. The top two panels represent absorption due primarily to H_2 and H . The middle left panel is dominated by H_2 absorption at higher radii and CH_4 at lower radii, while the middle right panel is dominated by CH_4 absorption at all altitudes. The bottom two panels show absorption largely caused by complex hydrocarbons.

Owing to channel-to-channel noise in the data, synthetic light curves resulting from the retrieved density profiles can be poor fits on an individual channel basis. Because the retrieved profiles result from spectral fits across many wavelength channels, it is better to compare against an averaged light curve such as those we show here. Note that the level of the observed light curves exceeds one for some data points because these curves represent the ratio of two measured spectra. The average level along the light curves is generally equal to or less than one, but any given point may be greater than one because of uncertainties in the measured spectra.

The wavelength ranges were chosen to span a variety of absorption regimes. The upper left panel is dominated by H_2 continuum absorption. The upper right panel is a combination of H_2 and H continuum absorption with some H_2 band absorption. The middle left panel is dominated by H_2 band absorption for the most part before absorption by CH_4 becomes important at the end. The middle right panel is primarily represents absorption by CH_4 . The lower left and lower right panels are dominated by absorption from C_2H_2 , C_2H_4 , and C_2H_6 . As can be seen, the structure in the data light curve in each panel is fit well by the synthetic light curve (light blue curve in Fig. 4). The worst fit is obtained for the H_2 band region shown in the middle left panel. This mismatch is possibly a reflection of small changes being needed in the temperature profile used in the retrievals or perhaps small changes in the modeled H_2 band absorption cross sections. Nevertheless, the overall fit is still excellent and the deviations are relatively minor. Tests done to examine the sensitivity of the retrievals to changes in temperature and therefore the H_2 band absorption show that the deviations between the data and synthetic light curves represent less than a 5% change in density.

5.1.2 Photochemical Modeling

Because the Voyager 2 solar ingress occultation had the highest signal-to-noise of all the Voyager UVS occultations, we have devoted a major part of our effort to modeling this particular occultation. We present two different forward models for this occultation that both provide a good fit to the retrieved H₂ and CH₄ density profiles and the occultation lightcurves. Both models assume the “Model C” chemistry of Moses et al. (2005). Our standard model has an eddy diffusion coefficient profile derived from the following expression:

$$\begin{aligned}
 K_{zz} &= 1.6 \times 10^7 (2.0 \times 10^{-4}/p)^{0.85} && \text{For } p < 2.0 \times 10^{-4} \text{ mbar} \\
 &= 1.6 \times 10^7 (2.0 \times 10^{-4}/p)^{0.79} && \text{For } 2.0 \times 10^{-4} \leq p < 0.5 \text{ mbar} \\
 &= 3.3094 \times 10^4 (0.5/p)^{0.78} && \text{For } 0.5 \leq p < 100 \text{ mbar} \\
 &= 5.0 \times 10^2 && \text{For } 100 \leq p < 640 \text{ mbar} \\
 &= 2.5 \times 10^4 && \text{For } p > 640 \text{ mbar}
 \end{aligned}$$

for eddy diffusion coefficient K_{zz} in cm² s⁻¹ and pressure p in mbar. As is shown in Fig. 3, this model (red curves) provides a good fit to the retrieved H₂ and CH₄ density profiles but not to the profiles for the C₂H_{*x*} hydrocarbons. The other model (blue curves), dubbed the “best-fit hydrocarbon” model, provides a statistically better fit to the hydrocarbon data but not to the H₂ density data. In this “best-fit hydrocarbon” model,

$$\begin{aligned}
 K_{zz} &= 1.56 \times 10^7 (2.0 \times 10^{-4}/p)^{0.87} && \text{For } p < 2.0 \times 10^{-4} \text{ mbar} \\
 &= 1.56 \times 10^7 (2.0 \times 10^{-4}/p)^{0.79} && \text{For } 2.0 \times 10^{-4} \leq p < 0.5 \text{ mbar} \\
 &= 3.2267 \times 10^4 (0.5/p)^{0.78} && \text{For } 0.5 \leq p < 100 \text{ mbar} \\
 &= 5.0 \times 10^2 && \text{For } 100 \leq p < 640 \text{ mbar} \\
 &= 2.5 \times 10^4 && \text{For } p > 640 \text{ mbar} \quad .
 \end{aligned}$$

Three other changes were made to the “best-fit hydrocarbon model”: (1) the low-pressure limiting rate constant for the reaction $\text{CH}_3 + \text{CH}_3 + \text{M}$ was increased, using the expression recommended by Smith (2003), (2) the adopted molecular diffusion coefficients for the stable C_2H_x hydrocarbons (see Moses et al., 2000) were reduced by 30%, and (3) the constraint for reproducing the Hubbard et al. (1997) refractivity profile was relaxed when constructing the model temperature profile.

Figure 3 shows how the density profiles from the two photochemical models compare with the retrievals, whereas Fig. 4 compares synthetic light curves created from the photochemical model results with the observed light curves. The standard model does an excellent job of reproducing the H_2 and CH_4 density profiles, as well as reproducing the observed light curves in the regions where the absorption is dominated by H_2 and CH_4 (the top four panels of Fig. 4). The standard model accurately predicts the C_2H_2 and C_2H_4 abundances near the midpoint altitude of the retrieved profiles but underpredicts the C_2H_6 density at most altitudes, and does not accurately predict the slopes of the profiles. Although the data retrieval process may be misassigning some of the contributions (e.g., some of the absorption attributed to C_2H_4 may actually be due to C_2H_2 , and/or some of the absorption attributed to C_2H_6 may actually be due to CH_4), the light curve comparisons in Fig. 4 suggest that the standard model has slightly insufficient hydrocarbon absorption, at least at the upper altitudes of the retrievals. The “best-fit hydrocarbon” model does a better job reproducing both the retrieved densities and the light curves in the regions dominated by the heavier hydrocarbons (lower two panels) although the model still slightly underpredicts the C_2H_x hydrocarbon absorption at high altitudes and underpredicts the hydrocarbon absorption at the lowest

altitudes extracted from the retrievals.

These model-data comparisons will aid photochemical modelers in constraining model inputs or otherwise interpreting the observed behavior. For example, the rate coefficients for the relevant hydrocarbon reactions are not well known at low pressures (and temperatures), and it is not surprising that the slopes of the model profiles do not exactly reproduce the data. Both the retrieved slopes and the overall retrieved $C_2H_2/C_2H_4/C_2H_6$ ratio will help modelers distinguish the dominant chemical pathways occurring in the homopause region of Saturn and the other giant planets (e.g., Moses et al., 2005; Nagy et al., 2009; Fouchet et al., 2009).

Additional insight into the implications for chemistry/transport in Saturn's homopause region can be gained from looking at the mixing ratio profiles as a function of pressure (see Fig. 5). Note that the conversion from a density-radius profile, which is the primary product from the UVS data inversion, to a mixing ratio-pressure scale is problematic. The main problem is that the ultraviolet wavelengths that are sensitive primarily to H_2 extinction become completely absorbed by the time the longer-wavelength CH_4 absorption becomes significant, so that no overlap exists between the radius levels for the H_2 and CH_4 density retrievals. That complicates the derivation of both pressures and mixing ratios. Converting from radius to pressure is thus very model dependent, with the temperature profile being the biggest uncertainty in the models. For Fig. 5, we have converted radius to pressure using our model grid from our "best-fit hydrocarbon" model.

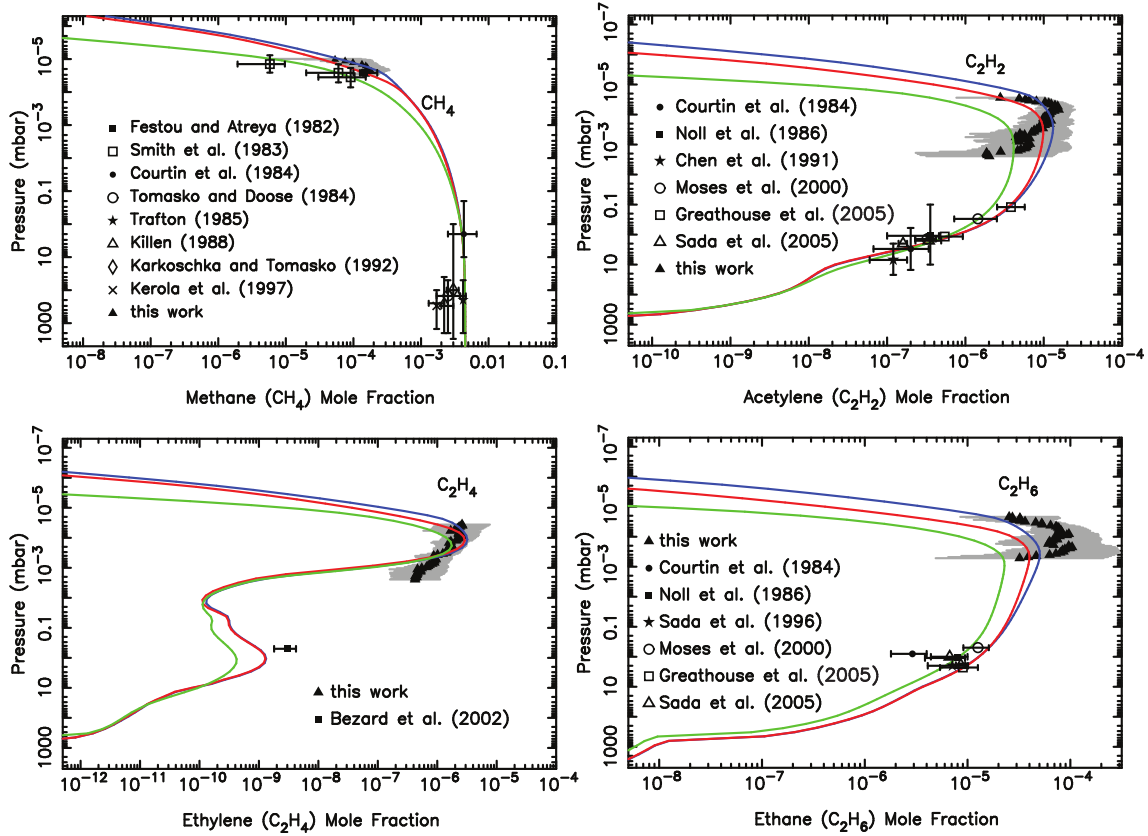


Fig. 5. The mixing ratios of CH₄ (top left), C₂H₂ (top right), C₂H₄ (bottom left), and C₂H₆ (bottom right) in our standard model (red) and “best-fit hydrocarbon” model (blue), as compared with the retrievals from the Voyager 2 solar ingress occultation (solid triangles) and various other pre-Cassini observations (as labeled). The pressure scale for the UVS retrievals plotted here is taken from the radius-vs-pressure grid from the “best-fit hydrocarbon” model and is very model dependent. The green curve is Model C from Moses et al. (2005).

Although a detailed and thorough discussion of the implications of our model-data comparisons with regard to chemistry and transport in Saturn’s homopause will be deferred to future work, we can make a few general statements regarding the comparisons. Figure 5 illustrates that methane and the C_2H_x hydrocarbons are being carried to very low pressures (high altitudes) in Saturn’s atmosphere at 29° latitude at the time of the Voyager 2 solar ingress occultation, implying strong vertical mixing or upward winds in Saturn’s upper atmosphere. This result is qualitatively in accord with previous analyses from various Voyager UVS data (e.g., Sandel et al., 1982a; Festou and Atreya, 1982; Atreya, 1982; Smith et al., 1983; Atreya et al., 1984; Ben Jaffel et al., 1995; Parkinson et al., 1998). A direct quote of the value of K_{zz} at the homopause in our model is not very helpful here because our assumed slope of K_{zz} at high altitudes is so large (e.g., in the extreme case of our “best-fit hydrocarbon” model, the official homopause level would be at $\sim 7 \times 10^{-7}$ mbar, with a K_{zz} of $\sim 2 \times 10^9$ $\text{cm}^2 \text{s}^{-1}$). A better comparative measure is the value of K_{zz} at the half-light point for the occultation at the wavelengths for which methane absorption dominates the light curve. For the Voyager 2 solar ingress occultation at 29° latitude, that radius is ~ 59463 km (907 km above the 1-bar radius). The corresponding pressure in our “best-fit hydrocarbon” model is $\sim 2.4 \times 10^{-5}$ mbar, at which point $K_{zz} \approx 1.0 \times 10^8$ $\text{cm}^2 \text{s}^{-1}$. In our standard model, the corresponding pressure is $\sim 3.1 \times 10^{-5}$, at which point $K_{zz} \approx 7.9 \times 10^7$ $\text{cm}^2 \text{s}^{-1}$. As can be seen from Fig. 5, our analysis suggests that atmospheric vertical mixing at 29° latitude at the time of the Voyager 2 UVS solar ingress occultation was as strong or even stronger than has been inferred from the previous UVS analyses for the Voyager 2 stellar egress occultation of δ Sco (Festou and Atreya, 1982; Smith et al., 1983) at 3.8° latitude.

The implications with regard to chemistry in the homopause region are harder to pin down, and more modeling will be required to fully investigate this issue. The standard model appears to have insufficient hydrocarbon absorption at the highest altitudes probed by the occultations. The fit cannot be improved by simply altering some of the uncertain chemical reaction rate coefficients from the Moses et al. (2005) model, as the molecules are in the diffusion-dominated regime at these pressures. Changes to chemistry inputs have little effect at these low pressures. The molecular diffusion coefficient for methane in H₂ and He has been measured (e.g., see the review of Marrero and Mason, 1972). Moses et al. (2000) used strategies outlined in Reid et al. (1987) to scale the expression for methane to derive molecular diffusion coefficients for the other hydrocarbons, and we follow those expressions. If we arbitrarily assume a ~30% error for these expressions and reduce the C₂H_x molecular diffusion coefficients by 30%, as we did in our “best-fit hydrocarbon” model, we can increase the hydrocarbon densities at high altitudes. Alternatively, we could have modified the slope of the temperature profile going into the thermosphere to obtain a better fit, or assumed that the profiles are controlled by an upward vertical wind.

Again, non-uniqueness problems affect the forward-modeling analysis, as it is possible to tweak several model free parameters to get the desired answer. However, we can safely say that the hydrocarbon model-data mismatch at the highest altitudes is likely due to transport effects or the temperature structure being inaccurately reproduced in the model rather than being due to chemical processes. These slight model-data mismatches do not detract the general firm conclusion of vigorous mixing in Saturn’s upper atmosphere at this particular location and time.

Diffusion time scales in the models are greater than a saturnian day at all pressures greater than a few $\times 10^{-6}$ mbar. Chemical loss time scales for the observed hydrocarbons are also greater than a saturnian day at the observed altitudes, but the chemical loss time scales are less than a saturnian season. Therefore, we do not expect any diurnal variations in insolation or diffusion to affect the modeled abundances. However, sufficiently strong diurnally variable winds might affect the species profiles (see section 6), and seasonal variations in the species profiles and vertical winds are expected based on seasonal variations in solar insolation (see Moses and Greathouse, 2005; Friedson and Moses, 2012).

In the lower portion of the density retrievals, the models again depart from the abundances derived from the inversions. The most obvious departure is for C_2H_4 , for which the models apparently greatly underpredict the C_2H_4 abundance at the lowest points of the occultations. This model-data mismatch occurs below the main hydrocarbon production region in which H Lyman α photolysis of CH_4 dominates the chemistry; the problem may be due to incorrect photolysis quantum yields for methane or the other hydrocarbons at wavelengths longer than H Lyman α , may be due to an incorrect description of reactions that convert C_2H_2 to C_2H_4 at these altitudes, or may be due to some other problem with the adopted chemistry. A similar model-data mismatch occurs for the other Voyager UVS occultations, as described below. Furthermore, Nagy et al. (2009) find that the same type of model-data mismatch occurs when models developed with the same basic chemistry inputs are compared to hydrocarbon profiles derived from the preliminary Cassini UVIS occultation analysis (Shemansky et al. (2005); see also Shemansky and Liu (2012)), lending credence to the suggestion that there are problems with the adopted C_2H_4 chemistry in the models below the H Lyman α production peak. As is consis-

tent with the discussion in Nagy et al. (2009), the chemical reaction list for Model A of Moses et al. (2005) does a better job of reproducing the slopes of the C_2H_x hydrocarbons as compared to the occultation retrievals, especially in terms of the narrowness of the C_2H_2 mixing-ratio peak shown in Fig. 5 and the C_2H_4 abundance in the microbar region. Similarly, models that take into account seasonal variation in solar insolation (based on Moses and Greathouse, 2005) also provide a better fit than the 1-D steady-state models shown in the figures here.

The mismatch between the model and data profiles may also, in theory, result from an incorrect attribution of absorption to C_2H_4 , which would increase its density at the expense of other species. At the resolution of the Voyager UVS, and once the absorption has progressed to such a large extent that most of the diagnostic wavelength range is completely absorbed, the similarity in the photoabsorption cross sections of the various hydrocarbons considered here makes this a possibility. Retrieval techniques will always try to find the best statistical match to the data, and the retrieved C_2H_4 profile presented here represents that best match. Close examination of numerous individual model and data spectra (not shown) does reveal that the C_2H_4 cross section is favored. However, as demonstrated by the comparison of the model light curves in Fig. 4 to the data at the longest wavelengths, very different density profiles (see Fig. 3) can yield similar light curves. Therefore, it may be the retrieved profiles for C_2H_2 and C_2H_4 , considered together, represent the total opacity of both species rather than the individual opacity, and some trade between C_2H_2 and C_2H_4 is possible in the retrieved density profiles. Nevertheless, the fact that similar data-model mismatches result from analysis of the higher resolution Cassini UVIS data indicates that this issue is unlikely to be the only

factor involved and that some photochemistry-related problem still exists.

An additional possibility is that other hydrocarbon species that were not included in the data retrievals contribute to the opacity at the wavelengths of the Voyager UVS. To test this possibility, we modeled light curves using our “best-fit hydrocarbon” model for this occultation including the full range of species listed in Table 2. These added species contributed less than 2% over the entire range of wavelengths longer than H Lyman α , and most of that was confined to only a few channels of the Voyager UVS. These model light curves are indistinguishable from those in Fig. 4 at the scale of the figures and are not shown. This test indicates that the hydrocarbon species retrieved from the Voyager occultations are by far the dominant species, to the extent the photochemical models are valid, and that inclusion of additional species in the retrievals is not warranted. Species not considered in Table 2 (e.g., C_4H_{10} and C_6H_6) are of sufficiently low abundance at relevant altitudes in the models that they were not considered. We note that C_4H_2 *was* included in the data retrievals but resulted in a statistically insignificant profile in all cases and thus is not shown in the figures. The contribution of C_4H_2 is, however, included in the light curves based on the photochemical models. On the other hand, if ion chemistry, which is not considered in our photochemical models, contributes to the high-altitude production of complex hydrocarbons, as it does on Titan (e.g., Waite et al., 2007), then further models that include ion chemistry should be developed to better address the possible abundance of complex neutrals in the occultation regions. Note also that the Cassini near-infrared stellar occultations show evidence for high-altitude hazes (Nicholson et al., 2006; Bellucci et al., 2009; Kim et al., 2012), which could potentially be affecting the Voyager UVS light curves.

Turning to the final hydrocarbon retrieved from the Voyager 2 solar ingress, we note that the inferred decrease in the C_2H_6 density and mixing ratio in the lower portion of the retrievals is unlikely to be real because C_2H_6 is a relatively stable molecule in this altitude region. The models predict that it should diffuse smoothly into the lower atmosphere, and a reduction in the C_2H_6 density with decreasing altitude is not expected based on what we know about the hydrocarbon chemistry and atmospheric transport. It is possible that strong winds are affecting the profile, but it is more likely that the mathematical inversion process used to retrieve this profile has difficulty in correctly attributing the source of the absorption in this region. This conclusion is supported by the fact that C_2H_6 absorption can be only be distinguished from absorption by other hydrocarbons only over a very narrow range of wavelengths. Within the uncertainties in the retrievals, however, the data profiles are mostly consistent with the model profile for the “best-fit hydrocarbon” model.

5.2 Voyager 1 Solar Egress

5.2.1 Data Retrievals

The Voyager 1 solar egress occultation, while providing similar information to that of the Voyager 2 solar ingress, was much different for a number of reasons. A mid-occultation gain change (already noted above) combined with large excursions in the pointing complicate the generation of the transmission spectra. However, because this occultation is the primary origin of the higher thermospheric temperature noted by Broadfoot et al. (1981a), we have endeavored to handle it as carefully as possible.

Figures 6 and 7 show the retrieved density profiles and data and synthetic light curve comparisons, respectively, for the Voyager 1 solar egress occultation. As with the Voyager 2 solar ingress, only every other point is shown for H₂ and H for clarity, the hydrocarbons profiles are retrieved using a tighter smoothing constraint than was used for the H₂ and H profiles, and the data light curves and uncertainties are averages over the specified wavelength ranges. The same general features in the retrieved density profiles as were noted for the Voyager 2 solar ingress retrievals are also present in the Voyager 1 solar egress case below the dashed horizontal line at 61200 km. Above this line, however, the H₂ profile for the Voyager 1 solar egress occultation is different from that for the Voyager 2 solar ingress.

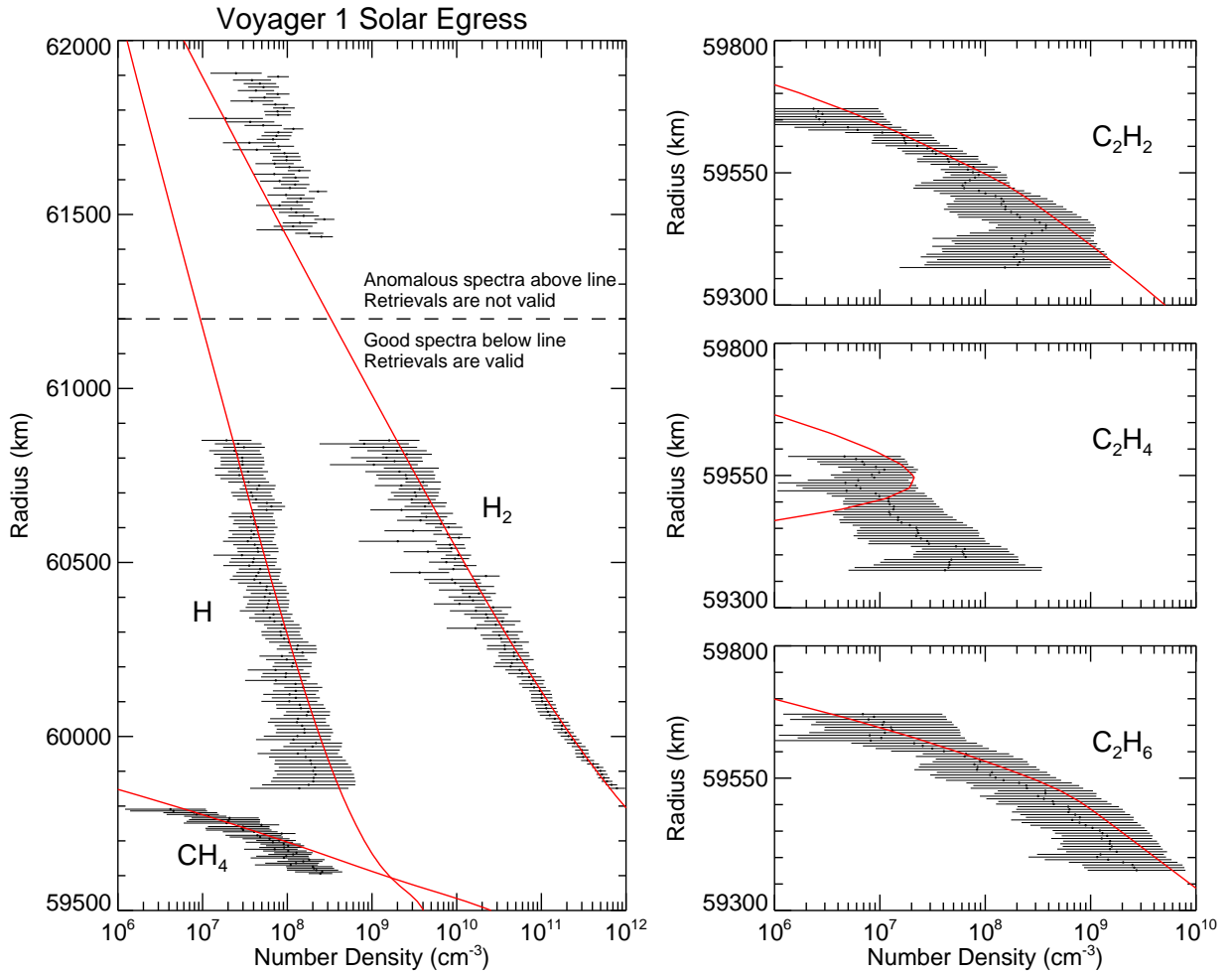


Fig. 6. The density profiles from our forward model (red curve) for the Voyager 1 solar egress occultation at -27° latitude are compared with the densities retrieved from our data inversions (black symbols, with associated one-sigma uncertainties). The left figure is for H_2 , H, and CH_4 , while the right panels are for C_2H_2 (top), C_2H_4 (middle), and C_2H_6 (bottom). Only every other point is shown for the H_2 and H profiles for clarity. See text for a discussion of the anomalous spectra and the implications of the retrieved H_2 profiles above and below the dashed line.

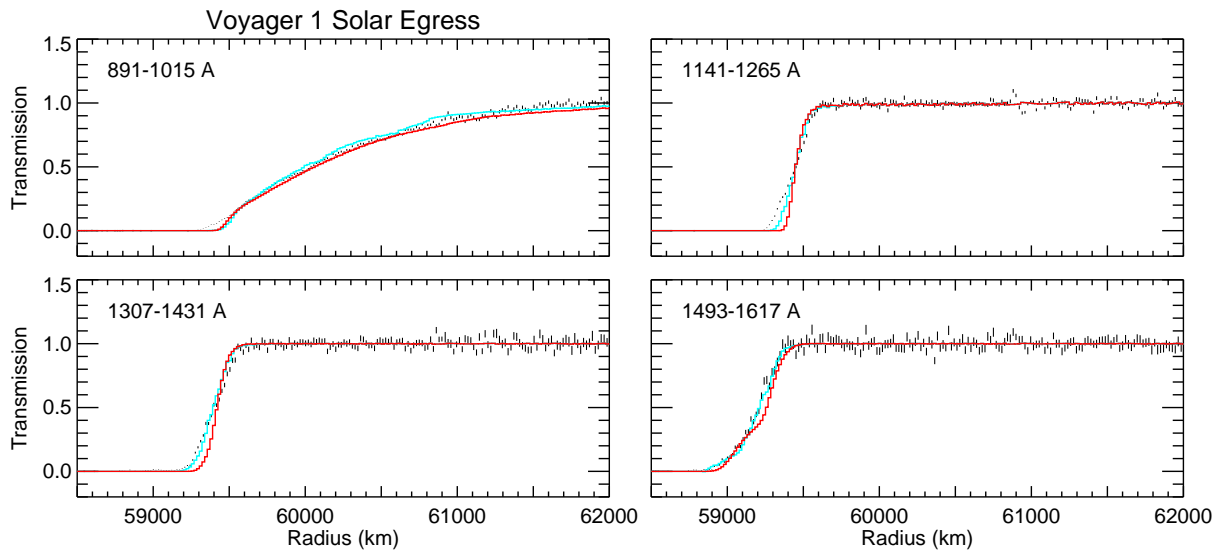


Fig. 7. Light curves from our reanalysis of the Voyager 1 UVS solar egress occultation compared with synthetic light curves generated from our photochemical model (red) and from the retrieved density profiles (light blue). The data are shown as black bars representing the one-sigma levels at each point. These curves are averages of several channels and span the wavelength ranges indicated in each panel (including limit-cycle-induced shifts). Only every sixth point is shown for clarity. The top left panel is dominated by H_2 absorption at higher radii and CH_4 at lower radii, while the top right panel is dominated by CH_4 absorption at all altitudes. The bottom two panels show absorption largely caused by complex hydrocarbons.

Clearly, the scale height of the Voyager 1 solar egress H₂ profile above 61200 km changes, which leads us to several possible scenarios: (1) the change in scale height may reflect a real change in temperature; (2) H₂ opacity has been mistaken for H opacity (notice the similarity to the H profile scale height); or (3) the data are bad. Scenario 2 can be ruled out because the cross sections for the H₂ and H continua are different enough to tell the two apart. Furthermore, because the cross sections for H₂ are larger than those for H at the wavelengths from which these densities are determined, the implied H densities at these altitudes would be even higher (roughly a factor of three) than the H₂ densities shown, leaving a significant discontinuity between the H densities above 61200 km and those measured below and shown in Fig. 6. The spectral fits at lower altitudes cannot support such a high H density, so a large discontinuity would be unavoidable and difficult to explain on a physical basis.

The first scenario — a temperature change — cannot be completely ruled out, and it is most likely this enhanced scale height at higher altitudes that led to the 850 K temperature determined in the earlier analysis (Broadfoot et al., 1981a). In fact, a simple fit of an exponential curve to these highest altitude density data yields a temperature of 798 ± 57 K. However, we consider it unlikely and favor the third scenario: bad data. The lack of a similar change in the higher-quality Voyager 2 solar ingress H₂ profile supports this conclusion, but there is further evidence that makes the scenario more certain. As noted by Vervack et al. (2004) for the Voyager 1 UVS egress occultation at Titan (which occurred before the Saturn occultations), the Voyager 1 UVS exhibited peculiar behavior at the shorter wavelengths, and that strongly appears to be the case here. Many of the channels in the H₂ continuum region between

600 and 850 Å for Voyager 1 are systematically low relative to neighboring channels when compared to the nominal solar spectrum shape generally observed by the Voyager 1 UVS. The net effect of these low signals is to force the retrieval to higher densities to find the best overall match to the data.

Additional evidence for anomalous behavior is that absorption at the shortest wavelengths is complete long before absorption at wavelengths greater than 850 Å is observed, leading to the large gap in the H₂ density profile in Fig. 6. Line-of-sight column densities over this range would all be equal because there is no changing absorption signature. This clearly is not the case in the Voyager 2 solar ingress occultation, and it makes no physical sense in the Voyager 1 solar egress occultation because it implies decreasing H₂ densities with decreasing altitude. We have therefore chosen only to show the retrieved H₂ densities above and below this problem region: above to illustrate the likely origin of the Broadfoot et al. (1981a) 850 K temperature from bad spectra, and below where the retrieved densities are derived from valid spectra. Note that from this point on, we will not discuss the Broadfoot et al. (1981a) results further.

We note that Smith et al. (1983) concluded that pointing issues and the gain change led to the higher temperatures in the initial analyses, but they did not elaborate. The ΔW motion of the spacecraft at this point in the Voyager 1 solar egress occultation did place the Sun close to the edge of the slit, therefore leading to a smaller input signal to the UVS simply due to the mechanical collimator. This fact, coupled with the lower HVL 2 gain of the UVS at the time of these observations, would have led to very few counts in the region of the solar spectrum where the anomalous behavior is observed and might possibly mimic the problems seen in the solar spectra. However, the pointing

and gain change affect all channels of the spectrum, and comparisons of HVL 2 solar spectra from regular solar calibration observations when the Sun is at the same point in the slit do not show the same spectral shape as observed in the Voyager 1 solar egress before absorption set in (i.e., in the reference spectra range). Therefore, we believe the answer to the anomalous behavior lies elsewhere, at least in part.

A possible explanation is that the observed behavior is connected to part of the UVS detector. The detectors were fabricated in sections of sixteen channels, and the problem channels appear to be confined to one or two adjoining sections. Whether it is a possible problem with the detector itself or the read-out electronics associated with these sections, we cannot say, but there is enough evidence to suggest that this region of the UVS detector was unreliable during the Saturn and Titan encounters, at least at the high signal levels of a solar occultation. Luckily, Saturn was the last planetary encounter for Voyager 1.

The net result of this problem with the spectra at short wavelengths is that the usable portion of the Voyager 1 solar egress retrievals does not probe to as large radial distances as the Voyager 2 solar ingress. Therefore, no panels corresponding to the upper left and upper right panels of Figure 4 are shown in Figure 7. However, the light curves and retrievals corresponding to lower radial distances are of good quality and provide the second-best set of Voyager UVS occultation data from Saturn.

5.2.2 Photochemical Modeling

The Voyager 1 solar egress occultation differs from the Voyager 2 solar ingress occultation mainly in that absorption due to methane and the other hydro-

carbons sets in at a lower altitude relative to the H₂ absorption, suggesting a lower-altitude homopause level and less vigorous atmospheric mixing. We developed several forward models for the Voyager 1 solar egress occultation; the temperature profile from our best-fit model can be found in the journal’s supplementary material and section 5.3. Although we still require a relatively warm lower stratosphere to provide enough H₂ density in the microbar region to compare with the occultation light curves, we find that our models fit the density retrievals better when the mesopause is located at relatively low altitudes (high pressures) as compared with the Voyager 2 solar ingress occultation. This solution makes sense physically, as the hydrocarbons appear to be diffusing out at higher pressures at the latitude of this occultation (−27°), leaving no efficient cooling agents at higher altitudes.

Our favored model for the Voyager 1 solar egress occultation has an eddy diffusion coefficient profile that fits the following expression:

$$\begin{aligned}
K_{zz} &= 1.0 \times 10^7 (2.0 \times 10^{-4}/p)^{0.5} && \text{For } p < 2.0 \times 10^{-4} \text{ mbar} \\
&= 1.0 \times 10^7 (2.0 \times 10^{-4}/p)^{0.78} && \text{For } 2.0 \times 10^{-4} \leq p < 0.5 \text{ mbar} \\
&= 2.237 \times 10^4 (0.5/p)^{0.68} && \text{For } 0.5 \leq p < 150 \text{ mbar} \\
&= 5.0 \times 10^2 && \text{For } 150 \leq p < 630 \text{ mbar} \\
&= 2.5 \times 10^4 && \text{For } p > 630 \text{ mbar}
\end{aligned}$$

for K_{zz} in cm² s^{−1} and p in mbar. The other model assumptions are similar to those from our “standard” model for the Voyager 2 solar ingress occultation.

Figure 6 shows how the density profiles from this forward model compare with our retrievals, and Fig. 7 shows how synthetic light curves generated from the model results compare with the observed light curves. In both instances, the high-altitude behavior is well reproduced, but problems exist at

lower altitudes. Although the observed half-light point in the light curves at methane-sensitive wavelengths is at roughly the same radius in this occultation (-27° latitude) as compared with the Voyager 2 solar ingress occultation (29° latitude), the gravity field and atmospheric structure are very different at these two latitudes, and the same radius translates to a different altitude and pressure. The greater centrifugal acceleration and the stronger zonal winds at -27° as compared to 29° latitude act such that the 1-bar radius is at least 150 km larger at -27° latitude than at 29° latitude (e.g., Lindal et al., 1985; Sanchez-Lavega et al., 2000). From either an extrapolation of the H_2 densities or from our forward modeling, we infer the half-light point for methane to be at a higher pressure in the -27° occultation than the 29° occultation, implying less vigorous atmospheric mixing at -27° latitude at the time of the occultation. For the Voyager 1 solar egress model at -27° latitude, the methane half-light point is 59452 km (681 km above the 1-bar level) or a pressure of $\sim 1.2 \times 10^{-3}$ mbar, at which point $K_{zz} \approx 2.5 \times 10^6 \text{ cm}^2 \text{ s}^{-1}$. The half-light point for methane is therefore inferred to be at a pressure roughly 40-to-50 times larger at -27° latitude than at 29° latitude (i.e., about one and a half scale heights deeper), at which point the eddy diffusion coefficient is 30-to-40 times smaller.

The model-data comparisons are not good in the lower portion of the occultations, especially at hydrocarbon-sensitive wavelengths. Unlike the situation for the 29° latitude modeling, our -27° latitude model produces too much hydrocarbon absorption (except for C_2H_4) at low altitudes compared to what can be allowed from the observations. The methane concentration, in particular, is too great. As can be seen from Fig 8, the inferred CH_4 mixing ratio drops with altitude from a peak near 10^{-4} mbar. This behavior is not possible

with diffusion alone; if real, the observed structure must be caused by wave activity or other winds with vertical shear. In contrast, the C_2H_4 concentration is greatly underpredicted by the models at low altitudes. As discussed earlier, the similar nature of this problem for all the occultation model-data comparisons here and with the Cassini UVIS analysis (see Shemansky and Liu, 2012; Nagy et al., 2009) suggests a shortcoming in the photochemical model. In particular, the model seems to be missing an effective pathway for converting C_2H_2 to C_2H_4 in the microbar region on Saturn.

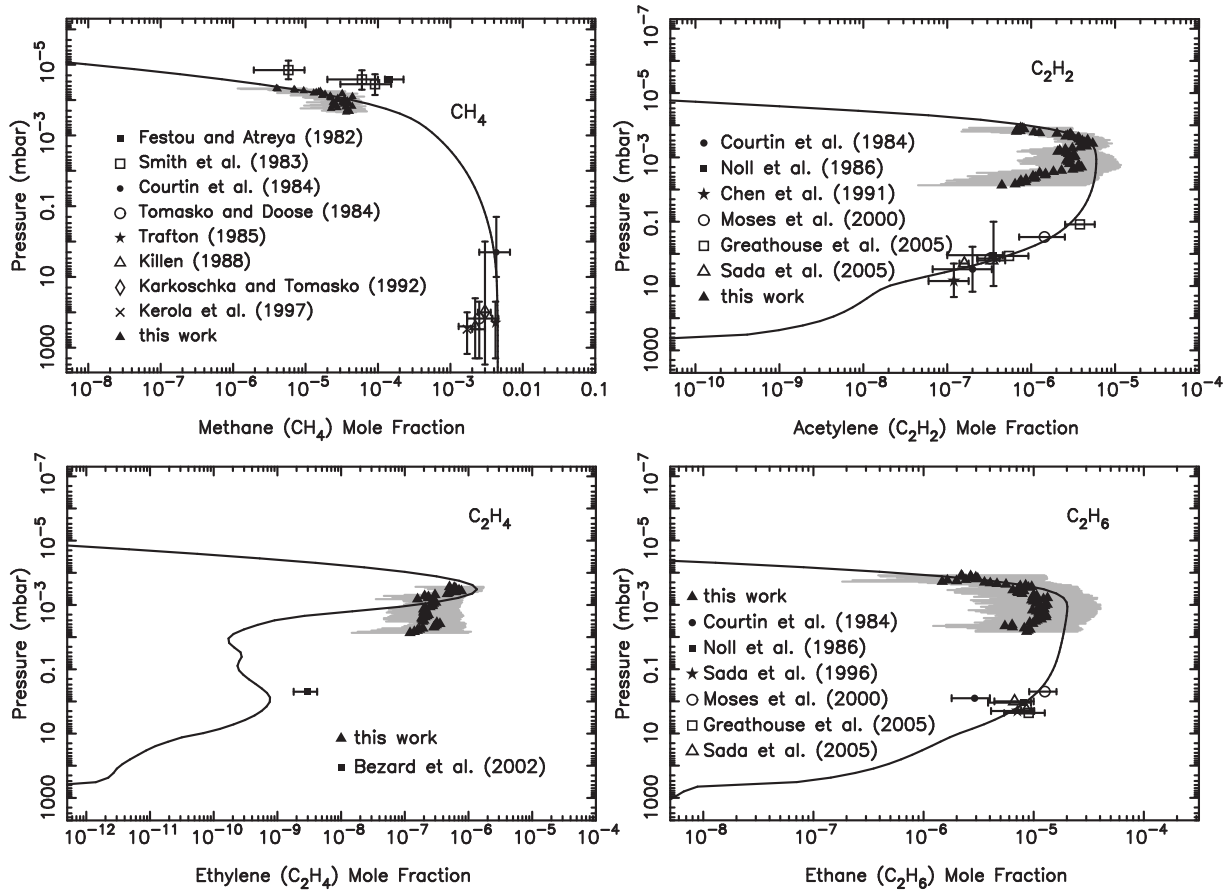


Fig. 8. The mixing ratios of CH_4 (top left), C_2H_2 (top right), C_2H_4 (bottom left), and C_2H_6 (bottom right) in our forward model (red) of the Voyager 1 solar egress occultation, as compared with our retrievals (solid triangles) and various other pre-Cassini observations (as labeled). The pressure scale for the UVS retrievals plotted here is taken from the radius-vs-pressure grid from the forward model and is very model dependent. Note that the inferred CH_4 homopause in this occultation is at higher pressures than that inferred from the Voyager 2 solar ingress occultation at 29° latitude.

5.3 *Voyager 1 and 2 Stellar Occultations*

5.3.1 *Data Retrievals*

The Voyager 1 and 2 stellar occultation data are of lower signal-to-noise than the solar occultation data owing to the vastly different intensity of the stars versus the Sun. The star used for the Voyager 2 stellar occultations was δ Scorpii (spectral type B0.2IV with $m_B=2.2$ and $m_V=2.3$); the star ι Herculis (spectral type B3IV with $m_B=3.6$ and $m_V=3.7$) was used for the Voyager 1 stellar egress occultation. Nevertheless, by averaging channels across wavelengths, we are able to retrieve H_2 and CH_4 density profiles for each of the three stellar occultations. However, meaningful retrievals of C_2H_x hydrocarbon densities have not been obtained (the resulting uncertainties are too large) although the light curves at those wavelengths can still provide some level of check on the heavier hydrocarbons in models if they are heavily averaged in both altitude and wavelength. Owing to absorption by interstellar H below 912 Å in the stellar spectra, H could not be retrieved.

In order to carry out the retrievals for these occultations, it is necessary to average the data in wavelength. For the Voyager 2 stellar ingress and egress, the data are averaged in groups of three adjacent wavelength channels; however, for the Voyager 1 stellar egress the averaging has to be done over ten adjacent channels owing to the very weak intensity of the star. No averaging is done as a function of altitude for any occultation.

An additional consideration for the Voyager 2 stellar ingress occultation is that it suffered from contamination by the rings. This contamination is evident in the data as “bite-outs” (localized dips) in the signal as a function of radius.

Because these “bite-outs” affect every wavelength, it is easy to distinguish these occurrences from actual atmospheric absorption. The regions affected are isolated and removed from the data and fortuitously do not significantly affect either the region of absorption or the range of reference spectra that are needed. Only one small gap in the H₂ absorption region is evident in the retrievals.

Figures 9, 10, and 11 (left panels) show the H₂ and CH₄ profiles retrieved from the Voyager 2 stellar egress, Voyager 2 stellar ingress, and Voyager 1 stellar egress occultations, respectively. Those figures also show comparisons of the data light curves to light curves synthesized using the retrieved density profiles. The two panels on the right of each figure show wavelength regions dominated by H₂ (top right panels) and CH₄ (bottom right panels) absorption. Despite the weaker nature of the stars, the retrievals for these occultations have yielded good measurements of the H₂ and CH₄ density profiles.

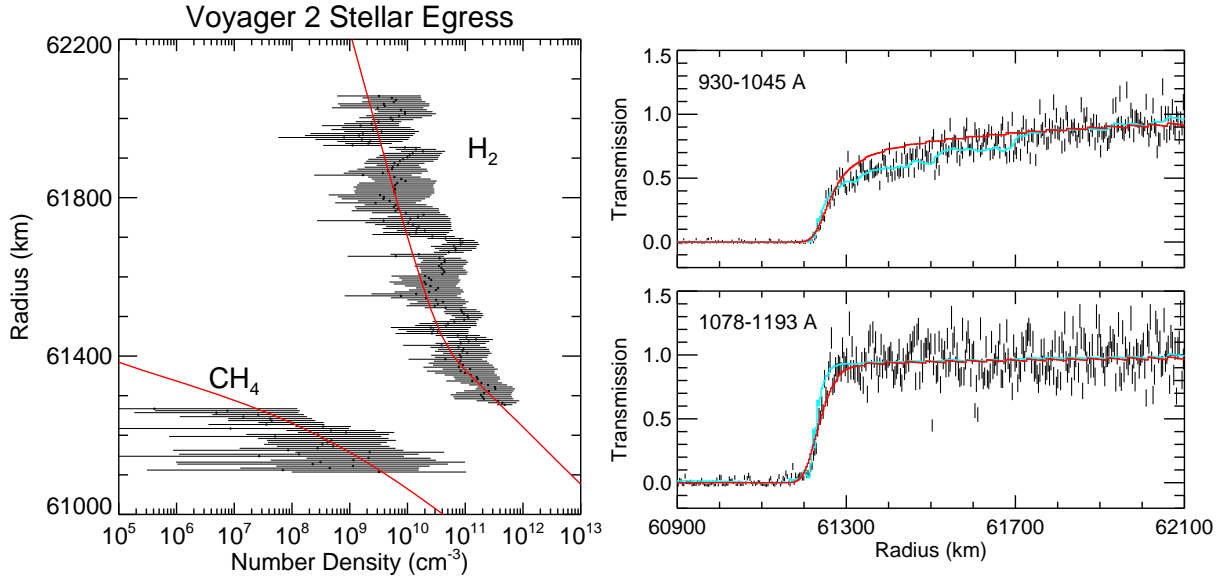


Fig. 9. The density profiles (left panel) from our forward model (red curve) for the Voyager 2 stellar egress occultation at 3.8° latitude are compared with the densities retrieved from our data inversions (black symbols, with associated one-sigma uncertainties). Profiles for H_2 and CH_4 are shown. Light curves (right panels) for this occultation are compared with synthetic light curves generated from our photochemical model (red) and from the retrieved density profiles (light blue). The data are shown as black bars representing the one-sigma levels at each point. These curves are averages of several channels and span the wavelength ranges indicated in each panel (including limit-cycle-induced shifts). Both panels show absorption due to H_2 and CH_4 ; H_2 dominates in the top panel and CH_4 in the bottom.

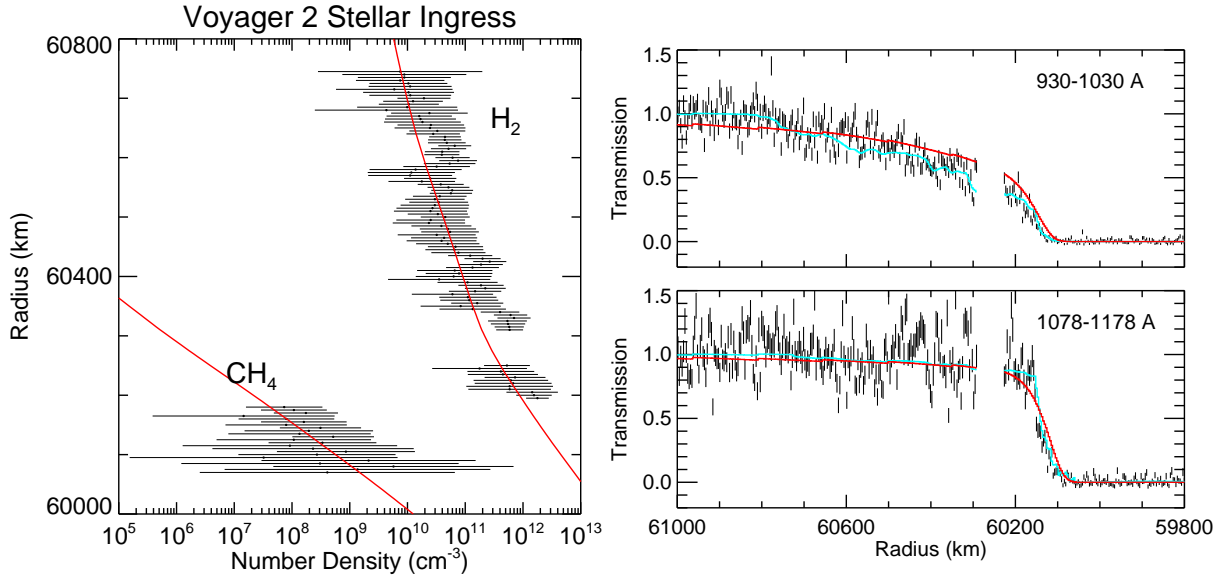


Fig. 10. The density profiles (left panel) from our forward model (red curve) for the Voyager 2 stellar ingress occultation at -21.5° latitude are compared with the densities retrieved from our data inversions (black symbols, with associated one-sigma uncertainties). Profiles for H_2 and CH_4 are shown. Light curves (right panels) for this occultation are compared with synthetic light curves generated from our photochemical model (red) and from the retrieved density profiles (light blue). The data are shown as black bars representing the one-sigma levels at each point. These curves are averages of several channels and span the wavelength ranges indicated in each panel (including limit-cycle-induced shifts). Both panels show absorption due to H_2 and CH_4 ; H_2 dominates in the top panel and CH_4 in the bottom. The gap is a region where spectra had to be eliminated owing to interference from Saturn's rings.

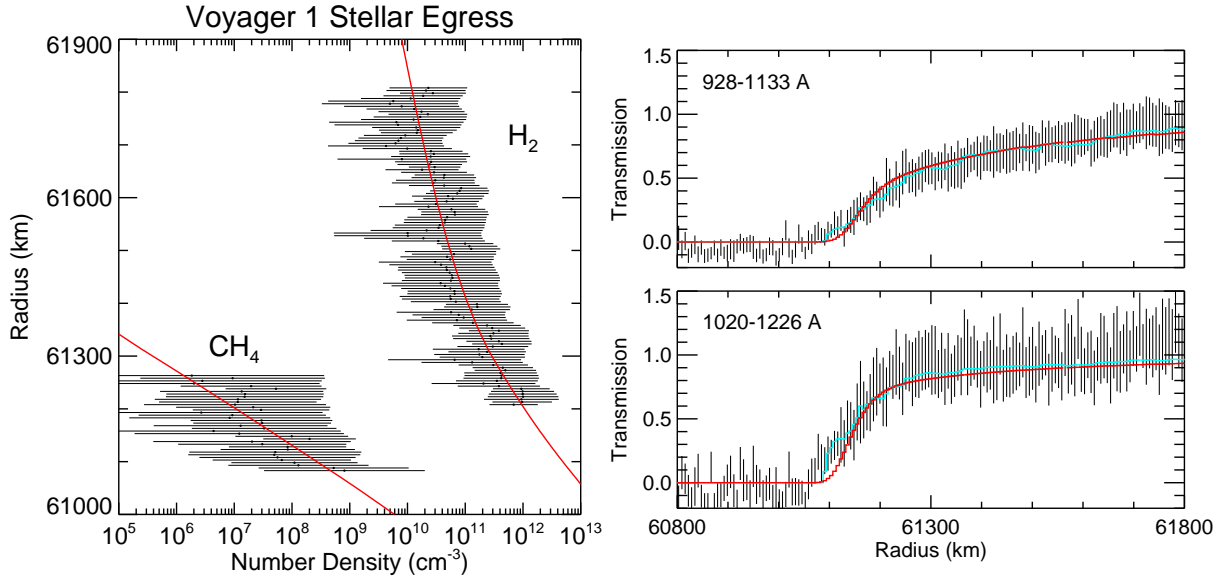


Fig. 11. The density profiles (left panel) from our forward model (red curve) for the Voyager 1 stellar egress occultation at -4.8° latitude are compared with the densities retrieved from our data inversions (black symbols, with associated one-sigma uncertainties). Profiles for H_2 and CH_4 are shown. Light curves (right panels) for this occultation are compared with synthetic light curves generated from our photochemical model (red) and from the retrieved density profiles (light blue). The data are shown as black bars representing the one-sigma levels at each point. These curves are averages of several channels and span the wavelength ranges indicated in each panel (including limit-cycle-induced shifts). Both panels show absorption due to H_2 and CH_4 ; H_2 dominates in the top panel and CH_4 in the bottom.

We note that this is the first time the Voyager 2 stellar ingress and Voyager 1 stellar egress have been analyzed. In the case of the former, the interference by the rings made the processing and retrieval complicated enough that it was never examined in detail despite its good quality otherwise. In the case of the latter, the weak star made for a very limited analysis. However, to provide greater latitudinal coverage, we have extracted as much information as possible from this occultation.

5.3.2 Photochemical Modeling

The retrieved H₂ and CH₄ density profiles for each stellar occultation are of high enough quality that we can generate forward models to at least determine the methane homopause levels or the values of K_{zz} at relevant altitude or pressure levels. Figures 9, 10, and 11 show how our forward models compare with the density retrievals, as well as how synthetic light curves from these models compare with the observations. Our model assumptions about the temperature and K_{zz} profiles are shown in Fig. 12.

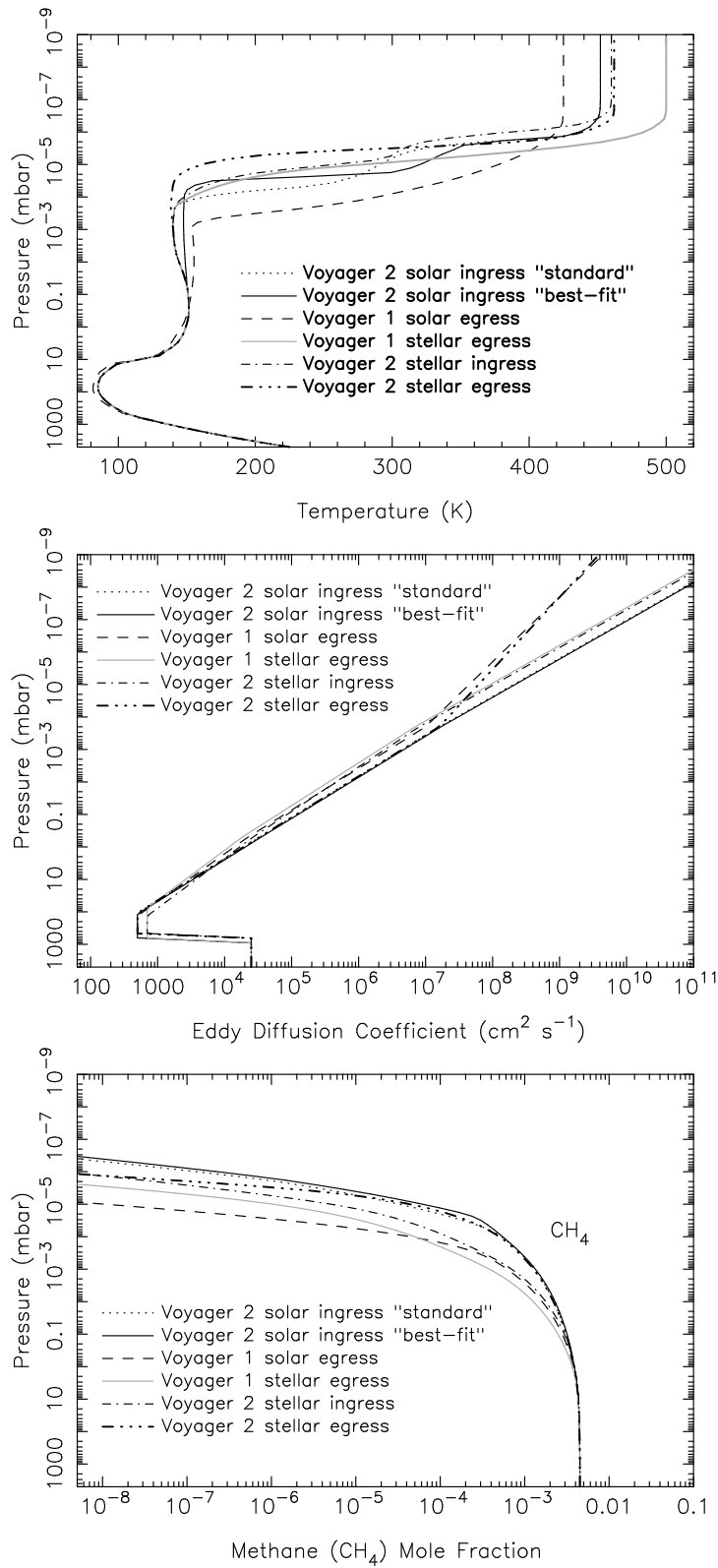


Fig. 12. The temperature profiles (top) and eddy diffusion coefficient profiles (middle) assumed for our forward models. The resulting model CH_4 profiles are shown in the bottom figure.

The models do an acceptable job of reproducing both the retrieved densities and the light curves. The signal-to-noise in the stellar occultations is low enough that the slopes of the CH₄ profiles — and hence the K_{zz} profiles — are hard to uniquely constrain, but we can at least provide some constraints on the heights to which the methane is carried. For the Voyager 1 stellar egress occultation at -4.8° latitude, the half-light point for the methane-sensitive wavelengths is at 61142 km (929 km above the 1-bar radius), corresponding to a model pressure level of $\sim 6.0 \times 10^{-5}$, at which point $K_{zz} \approx 2.0 \times 10^7 \text{ cm}^2 \text{ s}^{-1}$. For the Voyager 2 stellar ingress occultation at -21.5° latitude, the half-light point for the methane-sensitive wavelengths is at 60124 km (864 km above the 1-bar radius), corresponding to a model pressure level of $\sim 6.6 \times 10^{-5}$, at which point $K_{zz} \approx 2.1 \times 10^7 \text{ cm}^2 \text{ s}^{-1}$. For the Voyager 2 stellar egress occultation at 3.8° latitude, the half-light point for the methane-sensitive wavelengths is 61232 km (1000 km above the 1-bar radius), corresponding to a model pressure level of $\sim 1.8 \times 10^{-5}$ mbar, at which point $K_{zz} \approx 4.7 \times 10^7 \text{ cm}^2 \text{ s}^{-1}$. Those heights are best illustrated by the mixing-ratio plot in Fig. 12, which shows a significant variation between the different occultations. A convenient measure of the differences of the strengths of eddy mixing between the different latitudes is the pressure level at which the methane mole fraction drops to 5×10^{-5} in the models, and the K_{zz} value corresponding to that pressure level (see Table 4). That mole fraction value is sampled within the occultation regions for all the different models. Note from Fig. 12 and Table 4 that atmospheric mixing was very vigorous at 29° and 3.8° latitude at the time of the Voyager 2 solar ingress and stellar egress occultations and much less vigorous at -27° and -4.8° latitude at the time of the Voyager 1 solar egress and Voyager 1 stellar egress occultations.

Table 4

Model Parameters at Level Where CH₄ Mole Fraction is 5×10^{-5}

	Planetocentric	Pressure	K_{zz}	Local Time ^a
Occultation	Latitude	(mbar)	(cm ² s ⁻¹)	(average)
Voyager 2 solar ingress	29°			8.245
“standard model”		1.3×10^{-5}	1.6×10^8	
“best-fit hydrocarbon”		8.9×10^{-6}	2.4×10^8	
Voyager 2 stellar egress	3.8°	1.1×10^{-5}	6.0×10^7	9.63
Voyager 1 stellar egress	-4.8°	1.0×10^{-4}	1.3×10^7	10.56
Voyager 2 stellar ingress	-21.5°	4.1×10^{-5}	3.1×10^7	4.65
Voyager 1 solar egress	-27°	1.1×10^{-4}	1.4×10^7	2.77

^a Local time is defined using a Saturn rotational period of 10.76 hours (i.e., “noon” is 5.38 and “midnight” is 10.76). These are averages of the values in Table 1.

5.3.3 *On the Different Temperatures Derived from the Voyager 2 Stellar Egress Occultation*

We are now in a position to address the possible reasons for the vastly different temperatures derived for the Voyager 2 δ Sco stellar egress occultation at 3.8° latitude, for which Festou and Atreya (1982) favored an exospheric temperature of 800^{+150}_{-120} K, whereas Smith et al. (1983) favored 420 ± 30 K. Both analyses adopted a forward-modeling technique with a reference level within the occultation region. The data themselves help constrain the H_2 density at this reference level, so both groups have reasonable H_2 densities for at least part of the radial profiles. We argue that the differences between Smith et al. (1983) and Festou and Atreya (1982) likely result from data-quality issues, from pitfalls associated with attempts to derive temperatures from forward models using noisy data, and from attempts to use stellar occultations rather than solar occultations at H_2 continuum wavelengths to derive exospheric temperatures.

As an example of these problems and pitfalls, Figure 13 shows two assumed forward-model temperature profiles we developed for the δ Sco egress occultation region probed by Voyager 2. One profile (red curve) has a ~ 450 K exospheric temperature similar to that derived by Smith et al. (1983), whereas the other profile (blue curve) has an 800-K exospheric temperature and a profile similar to that derived by Festou and Atreya (1982). All other forward model parameters are the same between these two models, and all models go through the $\text{H}_2 = 1.2 \times 10^{12} \text{ cm}^{-3}$ point at 61212 km, as cited by Festou and Atreya (1982). Also shown in Figure 13 are the model results from the latest reanalysis of this occultation by Shemansky and Liu (2012) (green curve), and the unsmoothed H_2 density structure from our retrievals described

earlier in section 5.3. The triangles mark the radius-H₂ density points cited by Festou and Atreya (1982) in their text. Note, in particular, that the derived H₂ density of $5.0_{-1.8}^{+3.6} \times 10^9 \text{ cm}^{-3}$ at 61780 km compares very well with our H₂ retrieval at the same altitude.

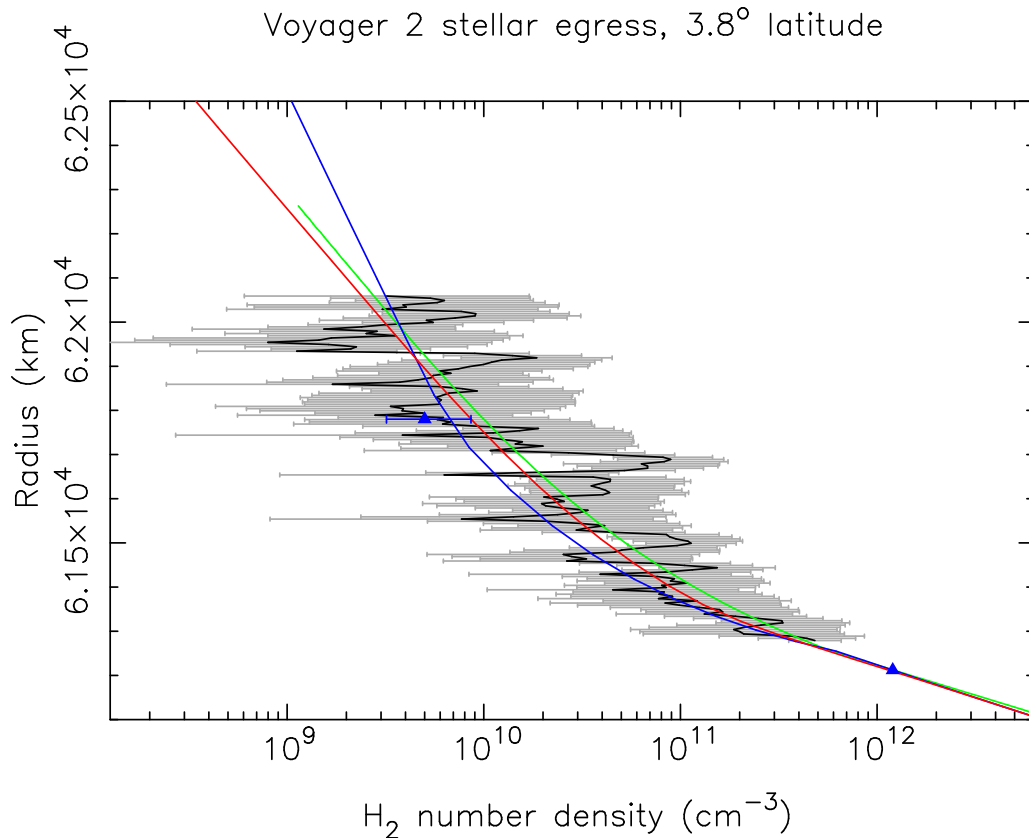


Fig. 13. The H_2 number density as a function of radius for the Voyager 2 δ Sco stellar egress occultation at 3.8° latitude from our data retrieval (black with associated gray error bars), compared with the model derived from the Shemansky and Liu (2012) reanalysis of this occultation (green), and two of our own forward models that assume an exospheric temperature of 450 K (red) and 800 K (blue). The blue triangles represent the H_2 density at two specific points discussed in the occultation analysis of Festou and Atreya (1982). Note the similarities in the H_2 densities inferred from all these techniques, despite the widely different assumed or derived temperature profiles. This non-uniqueness is the likely cause of the different derived exospheric temperatures from Festou and Atreya (1982) and Smith et al. (1983) from the same occultation. This comparison highlights the potential pitfalls of using forward models alone to determine temperatures from ultraviolet occultations.

Although our retrieved H₂ profile provides the best mathematical fit to the occultation light-curve data, all three model profiles with their very different thermal structures provide a reasonable fit (to within the noise level of the data) to the light curves at wavelengths sensitive to H₂ absorption. This exercise illustrates the non-uniqueness of the forward modeling (see also Appendix A), and, in particular, the difficulty in constraining temperatures from forward models. Forward modeling of noisy stellar occultation data is thus limited in its ability to uniquely determine the exospheric temperatures on Saturn, and care should be exercised in interpreting such results.

5.4 Voyager 1 Solar Ingress

Among the Voyager UVS occultations, the Voyager 1 solar ingress occultation is highly unique owing to its location at -83° latitude. Unfortunately, the passage of Voyager under Saturn's southern pole caused the spacecraft trajectory to change rapidly during the occultation. In order for the scan platform to keep the UVS boresight oriented on the Sun, it had to slew at regular intervals. Data acquired during a slew are not good, and because there is a finite settle time after a slew, data immediately after a slew are also not viable. The usable range of data therefore consists of a number of small ranges of radii separated by gaps.

A further complication is that each time the scan platform executes a slew, the limit cycle information, which is a relative measure of position, resets. Therefore, in order to generate the transmission spectra, each segment of good data has to be tied to the adjacent segment so that reference spectra acquired early in the occultation can be placed in the same limit cycle frame as the

absorption region spectra. To do this, the position of the H Lyman α line is used as a reference point in each spectrum and the limit cycle for each spectrum is tied to the known shift of the H Lyman α line relative to its on-axis position. In this manner, a consistent limit cycle frame for the entire occultation can be constructed.

Although retrievals of H₂ and H are possible, unfortunately no hydrocarbon retrievals can be carried out for two reasons. First, hydrocarbon absorption generally takes place very rapidly at the homopause level owing to the nature of the hydrocarbon profiles as a function of radius (i.e., fast fall-off near the homopause). It just happens that the majority of the range of hydrocarbon absorption falls into one of the unusable gaps. Second, once the H Lyman α line is absorbed, the remaining segments of good data cannot be tied to the others with high confidence. Thus, even though there are some few spectra for which retrievals may be possible, they cannot be placed in the same frame as the others.

Figure 14 shows the H₂ and H profiles retrieved from the Voyager 1 solar ingress occultation. The multiple slews of the scan platform are the cause of the large gaps in the profiles. The difficulty in relating the reference spectra to the attenuated spectra across these slews likely leaves some residual artifacts in the profiles; nonetheless, they compare well with profiles from the other Voyager UVS occultations. As the only profiles measured in the polar region of Saturn, we consider the extra work required to determine these profiles worth the effort. However, because only the H₂ and H profiles can be retrieved, we do not carry out any photochemical modeling of this occultation.

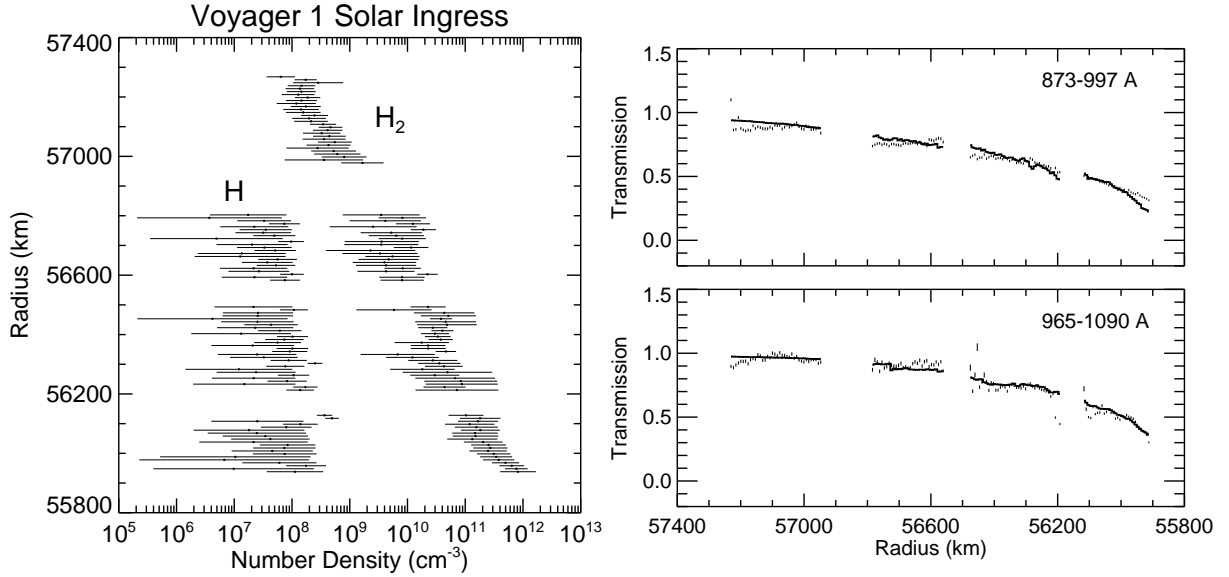


Fig. 14. The density profiles (left panel) retrieved from our data inversion (black symbols, with associated one-sigma uncertainties) for the Voyager 1 solar ingress occultation at -83° latitude. Profiles for H_2 and H are shown; only every other point in these retrieved density profiles is plotted for clarity. Light curves (right panels) for this occultation are compared with synthetic light curves generated from the retrieved density profiles. The data are shown as black bars representing the one-sigma levels at each point. These curves are averages of several channels and span the wavelength ranges indicated in each panel (including limit-cycle-induced shifts). Only every third point in the data light curves is shown for clarity. The top panel shows absorption due to H_2 and H ; the bottom panel is absorption by H_2 . The large gaps are caused by scan platform slews as described in the text.

5.5 Further Considerations From the Data Retrievals

At this point, it is illustrative to compare the retrievals from all six occultations. However, to do this we have to place the occultation results on a common scale.

One such common scale is pressure, and in Fig. 15 we have plotted the retrieved H₂ profiles for five of the occultations versus pressure. To derive the pressure, the retrieved profiles are smoothed to eliminate the point-to-point noise and then integrated according to

$$P(r) = \int_r^{\infty} m_{\text{H}_2} g(r') n(r') dr', \quad (6)$$

where m_{H_2} is the mass of molecular hydrogen (dominates the mass profile over our retrieved range) and $g(r)$ is gravity. The density profiles are assumed to fall off exponentially at the top. Because of the large gaps in the Voyager 1 solar ingress occultation, we cannot derive a pressure profile for this occultation.

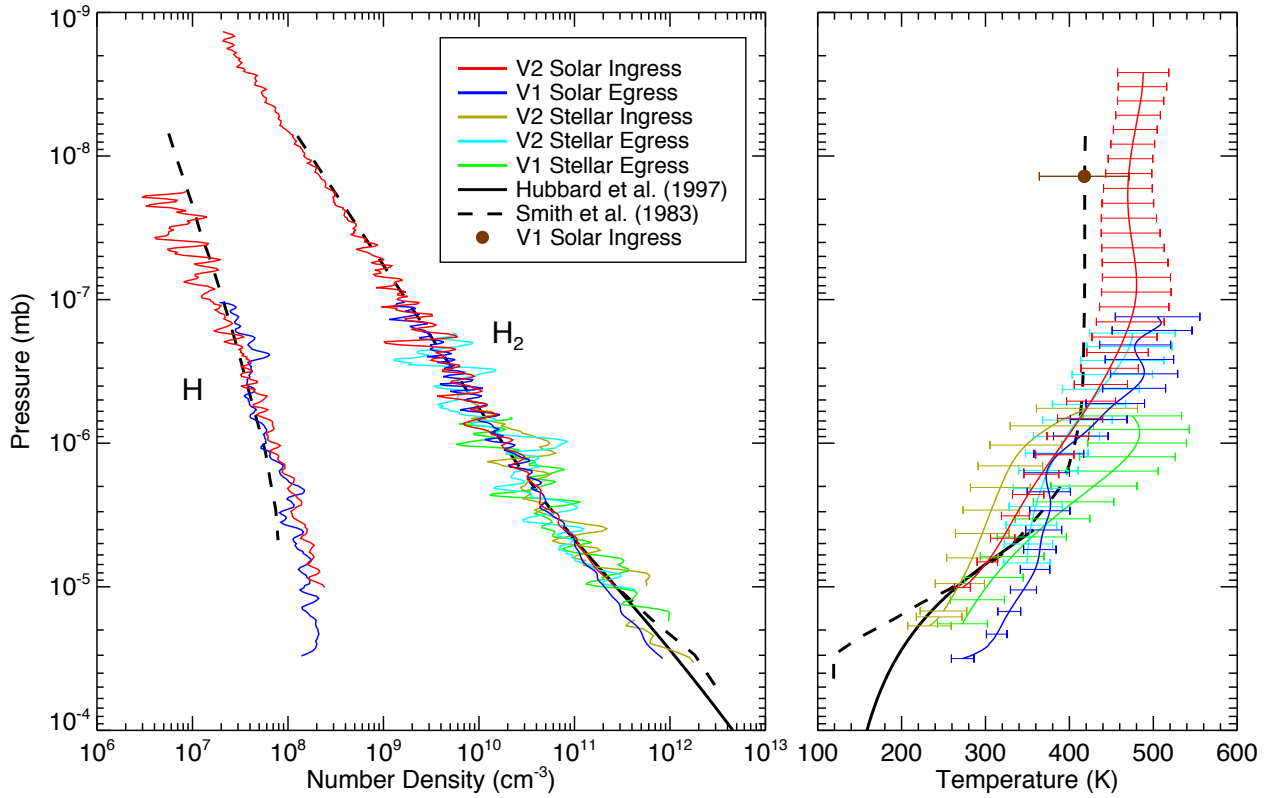


Fig. 15. Summary figures showing the retrieved H₂ and H density profiles (left panel) and inferred temperature profiles (right panel) as a function of pressure. Comparisons are made to the analyses of Smith et al. (1983) and Hubbard et al. (1997). The pressure and temperature derivations, as well as the implications of the comparisons, are discussed in the text.

Fig. 15 shows that retrieved H₂ density profiles for the five occultations compare well, as do the H profiles for the two solar occultations. Also shown on the figure are the profiles from the Smith et al. (1983) and Hubbard et al. (1997) analyses. In general, the agreement with the Smith et al. results is reasonably good, although there are deviations near the top and bottom of the H profile and at the bottom of the H₂ profile. The latter difference is notable because this is the region where Hubbard et al. had difficulty matching the Smith et al. results. Indeed, there is a clear deviation of the Smith et al. H₂ profile from the Hubbard et al. profile. Our retrieved H₂ profiles, as well as the Smith et al. profile, merge well with the Hubbard et al. profile at pressures less than 10 nanobars. This consistency at high altitudes but not low altitudes suggests that perhaps the Smith et al. retrieval pushed the transmission spectra a bit too far at the bottom end of the range. We restrict our retrievals to transmission levels between 0.1 and 0.9 because outside this range, the uncertainties in the retrievals rapidly increase as the absorption signatures approach the signal-to-noise limits of the transmission spectra. Smith et al. presented model profiles rather than retrieved profiles, so there were no uncertainties presented, and we cannot say for sure if this is the case. In any event, the good agreement between the retrievals presented here and the Hubbard et al. profile in the region of overlap, as well as between the Smith et al. and Hubbard et al. profiles away from pressures greater than 10 nanobars, demonstrates that the UVS and ground-based occultation datasets are compatible and can merge smoothly.

An advantage of determining the pressure at each radius is that we can also get an estimate of the temperature profile from the density profile using the ideal-gas-law relationship $P = nkT$. In this case, we assume the total density n is

just the H₂ density, a reasonable assumption for the range we are considering, and solve for T at each pressure. Uncertainties in the temperature can be determined by propagating the uncertainties in the density through the entire process of integrating to get P and then solving for T .

The resultant temperature profiles are shown in right panel of Fig. 15. It should be noted that these are not exact representations of the temperature profile but are rather general indications. The feedback between the assumed temperature profile and the H₂ band absorption cross sections in the retrieval process makes it difficult to pin the temperature down in the H₂ band absorption region with great accuracy. High-resolution measurements that reveal the detailed ro-vibrational band structure of H₂ are required and must be combined with modeling of the sort described in Hallett et al. (2005b). Such high-resolution spectra are beyond the capability of the Voyager UVS and Cassini UVIS instruments, although the UVIS does provide higher resolution than the UVS. Nevertheless, the general comparison among the various profiles indicates on a basic level the potential variation in the temperatures at these pressure levels.

All of the UVS temperature profiles exhibit a generally similar shape in the region of overlap, suggesting that latitudinal variations in temperature at these levels of the atmosphere are relatively small ($\lesssim 100$ K) but still exist. Some wave-like structures are suggested in both the density retrievals and the inferred temperatures; however, these small-scale “wiggles” should be taken with a grain of salt given that the temperature retrievals in particular are only bulk estimates, as described above.

Also shown in Fig. 15 are the temperature profiles of Smith et al. (1983) and

Hubbard et al. (1997). In the region of overlap, the agreement between the temperature profiles inferred from our work and that of Hubbard et al. (1997) is good, although the Voyager 1 solar egress profile does appear to show more deviation at lower altitudes than the other profiles do (note that the same is true at the lower altitudes of the density-pressure profile on the left). The Smith et al. (1983) temperatures agree well in the middle of the profile, but their profile deviates at the lowest and highest altitudes. We have already addressed the deviation of the Smith et al. density-pressure profile from the Hubbard et al. (1997) profile, so it is not surprising to find similar deviations in the temperatures at low altitudes. Again, we do not know the exact circumstances by which Smith et al. (1983) derived their temperature profile, but there does not appear to be supporting evidence for their low-altitude structure in the Voyager UVS datasets, which on the whole are more consistent with the Hubbard et al. (1997) profile. As for the differences between our results and the Smith et al. (1983) profile at higher altitudes, we find slightly higher temperatures: roughly 460-490 K versus the 420 K determined by Smith et al. (1983).

Our results can also be compared to the thermospheric temperatures derived from the Cassini UVIS solar and stellar occultations (Shemansky and Liu, 2012; Koskinen et al., 2013) and to temperatures inferred from auroral H_3^+ emission (e.g., Melin et al., 2007; Melin et al., 2011; Stallard et al., 2012; O'Donoghue et al., 2014). The temperatures at the highest altitudes of the Voyager 2 solar ingress occultation are derived from the H_2 densities determined from the H_2 continuum region. Because the H_2 continuum cross sections are generally insensitive to temperature, the density determination and subsequent temperature inferral for the Voyager 2 solar ingress occultation are robust results.

Koskinen et al. (2013) performed a similar analysis of the Cassini UVIS solar occultations in the H₂ continuum region, and they derived exospheric temperatures ranging from 370 to 540 K, which appear to be fully consistent with our results. Koskinen et al. also find a statistically significant difference between exospheric temperatures at high and low latitudes, with the poles being 100-150 K warmer than the equator. Our Voyager 2 solar ingress and Voyager 1 solar egress results are consistent with results from similar latitudes in the Koskinen et al. (2013) analysis, but our derived temperature for the -83° Voyager 1 solar ingress is closer to 400 K than the ~ 540 K temperature derived for a similar latitude by Koskinen et al. (2013). The single thermospheric temperature value for this Voyager 1 solar ingress occultation is derived through fitting an exponential profile to the H₂ densities in the radial range 56900–57300 km, where the best-determined H₂ densities are located for that occultation. The temperature is then obtained from the scale height of the fit, and the pressure for plotting purposes is inferred from $P = nkT$. Given the spacecraft slewing and potential anomalous channel behavior during the Voyager 1 solar egress, we do not place much significance on this high-latitude discrepancy between our results and those of Koskinen et al. (2013).

Shemansky and Liu (2012), in contrast, have analyzed Cassini UVIS stellar occultations, for which signal in the H₂ continuum region is unavailable owing to absorption of the stellar source by interplanetary hydrogen. The UVIS temperature determination at the higher altitudes is therefore based on complex modeling of H₂ band absorption (e.g., Hallett et al., 2005b; Shemansky and Liu, 2012). Deriving temperatures from such modeling is difficult without high spectral-resolution data, and — as we noted in section 5.1 — the temperature can vary over a great range and have only small effects on the H₂

densities. From an analysis of the occultation spectra over the full available wavelength range, including the H₂ band region, Shemansky and Liu (2012) derive thermospheric temperatures ranging from 318 to 612 K for three stellar occultations at latitudes of -42.7° , -3.6° , and 15.2° , with the near-equatorial results being the hottest and the higher latitude results being the coldest, in contrast to the general trend found by Koskinen et al. (2013). Given the small number of occultations analyzed in both our Voyager analysis and that of Shemansky and Liu (2012), discrepancies between their results and ours may not be meaningful, but we do note that the thermal profiles derived by Shemansky and Liu (2012) exhibit more variability from occultation to occultation than we see with our retrieved temperatures.

Temperatures have also been inferred from H₃⁺ auroral emission (e.g., Melin et al., 2007; Melin et al., 2011; Stallard et al., 2012; O’Donoghue et al., 2013, 2014), where temporal and hemispheric variability have been noted. Temperatures derived this way have ranged from 380 ± 70 K in 1999 and 420 ± 70 K in 2004 (Melin et al., 2007), to 440 ± 50 K in 2008 (Melin et al., 2011), to 560–620 K in 2007, with the latter observations showing significant variability on time scales of a few hours (Stallard et al., 2012). Recent observations from 2011 reported by O’Donoghue et al. (2014) suggest that the southern aurora at 583 ± 13 K is on average hotter than the 527 ± 18 K northern aurora, perhaps because the thermospheric heating rate from Joule heating and ion drag is inversely proportional to magnetic field strength, and the larger field strength in the north results in less total heating. The Voyager UVS data and the Cassini UVIS data reported to date are too sparsely sampled to comment on whether there is a statistically significant difference between the derived temperatures in the north versus south.

Because the retrieved H₂ profiles do not extend to the levels at which the hydrocarbons are retrieved, we cannot plot the retrieved hydrocarbons as a function of pressure. Instead, we show in Figure 16 the profiles retrieved from all six occultations after they have been shifted in radius to a common reference grid for comparison and again smoothed to minimize the the profile-to-profile noise. The process is carried out by shifting each H₂ profile in radius only until it gives the best match to the final model of Hubbard et al. (1997) in the region of overlap between the H₂ density profiles as determined by a chi-squared comparison. The shift in radius determined for H₂ is then applied to the radial scales for all the density profiles for that occultation. Shifting the profiles in this manner establishes a crude “equatorial equivalent” scale but does provide a means for comparing the density profiles for the occultations to each other and to other data or models referenced in a similar fashion. The Hubbard et al. (1997) profile is chosen as the reference because it is a commonly cited profile.

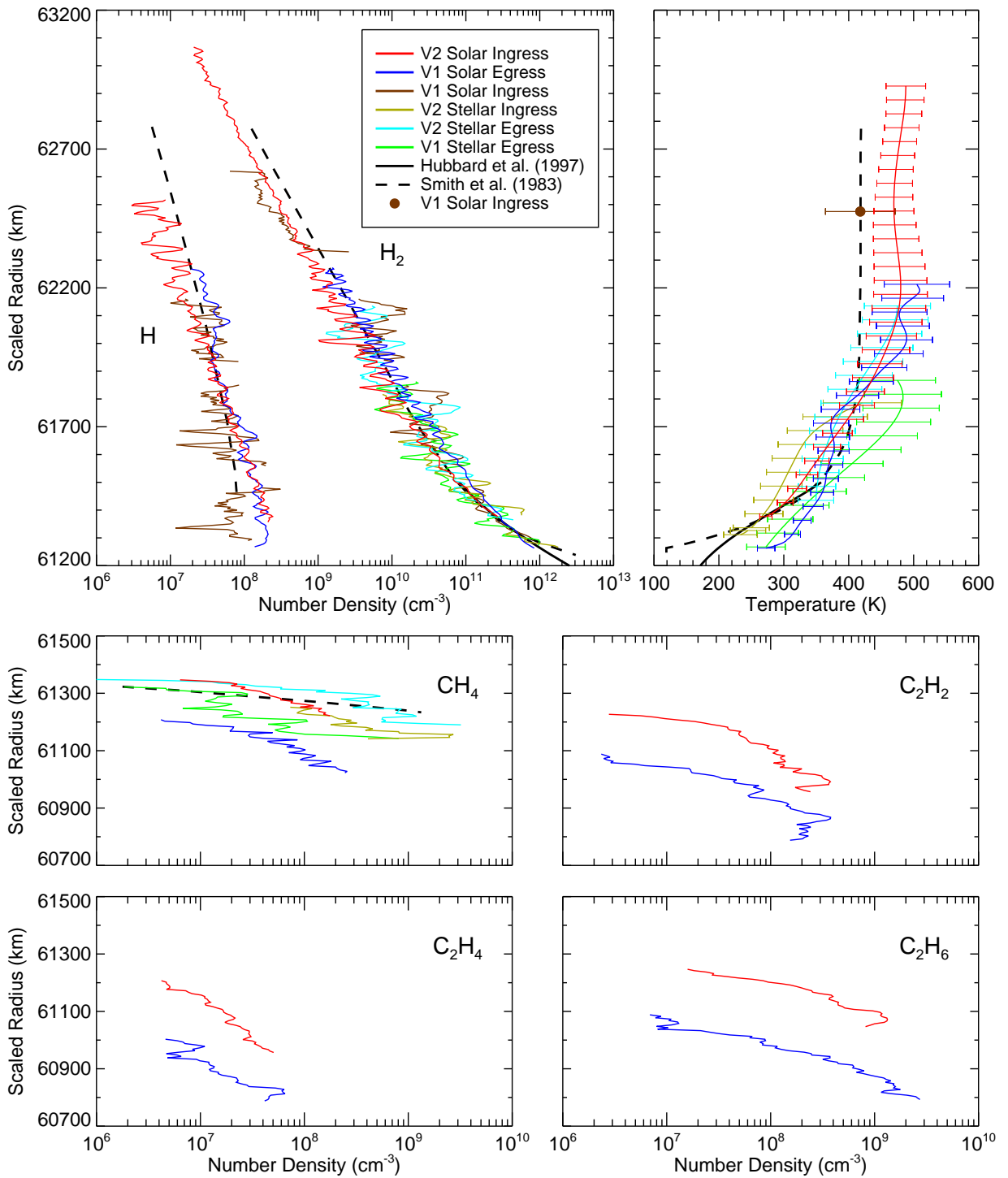


Fig. 16. Summary figures showing the retrieved H₂ and H density profiles (top left panel), hydrocarbon profiles (bottom four panels), and inferred temperature profiles (top right panel) on an “equatorial equivalent” radial grid. Comparisons are made to the analyses of Smith et al. (1983) and Hubbard et al. (1997). Derivation of the radial grid and implications of the comparisons are discussed in the text.

As seen in Figure 16, the H_2 and H profiles compare favorably for all the occultations and merge relatively smoothly with the Hubbard et al. (1997) profile, not unexpected given the good agreement among the profiles as a function of pressure shown in Fig. 15. Figure 16 also shows the profiles from Smith et al. (1983). The deviation of the Smith et al. H_2 profile from the Hubbard et al. profile is again clearly seen near the bottom of the H_2 profiles but is not exhibited by the H_2 profiles retrieved in the current analysis. We find that the only way we can reproduce the turn-up at the bottom of the Smith et al. profile is to retrieve H_2 independently of CH_4 . In other words, it is possible that the Smith et al. profile for H_2 includes some opacity that should have been assigned to CH_4 and vice versa. Thus, we conclude that the Smith et al. profile is in error at the lowest altitudes and that the Voyager UVS data are consistent with the results of Hubbard et al. (1997).

Although the H_2 and H profiles compare well, the hydrocarbon profiles are a different story. Most surprising is the shift between the Voyager 1 solar egress (blue) and Voyager 2 solar ingress (red) profiles. When the radial scales are shifted such that the H_2 and H profiles agree well, there is a 150–200 km altitude discrepancy between the hydrocarbon profiles despite the similar shapes of the profiles. Shemansky and Liu (2012) saw similar large variability in the hydrocarbon profiles from different occultations in their Cassini UVIS analysis. Although problems related to the determination of the radii, perhaps caused by errors in the pointing knowledge, cannot be ruled out, we think it is more likely to be a dynamical effect. As is discussed in section 5.2, a variable eddy diffusion coefficient as a function of latitude is certainly plausible and could explain the differences in the CH_4 profiles for all of the occultations. Similarly, a large-scale circulation pattern could cause this variation, with

methane restricted to high pressures in downwelling regions, and methane carried to low pressures in upwelling regions. If this process is occurring, temperatures may also be affected through adiabatic heating and cooling, and a detailed comparison of the CIRS limb data that allow retrievals of temperatures and hydrocarbon abundances in the middle atmosphere (e.g., Guerlet et al., 2009, 2010) with the numerous Cassini UVIS occultation data that will allow determinations of temperatures and abundances in the mesopause region (Shemansky et al., 2005; Nagy et al., 2009) might prove fruitful in deriving or constraining middle-atmospheric circulation on Saturn. Further comparison with the Voyager data described here would shed light on the time scales and seasonality of that circulation. Comparisons with stratospheric general circulation models (e.g., Friedson and Moses, 2012) might also shed light on the observed behavior.

Figure 16 also shows the temperature profiles derived from the H₂ density profiles. These are the same temperature profiles shown in the right panel of Fig. 15, just plotted on the scaled radius grid. It is interesting to note that the Voyager 2 solar ingress temperature profile is shifted with respect to the Voyager 1 solar egress profile in the lower portion of the profiles by about the same radial amount as the shift noted for the hydrocarbon profiles. This similarity in the vertical shift for both the hydrocarbons and temperatures is consistent with the cooling being correlated with the C₂H_x hydrocarbon abundances. A similar correlation between the temperature profiles and the CH₄ profiles for the other occultations may also be the case, though within the uncertainties of the temperature profiles, that possibility is not clear.

The ultimate heat source driving the high thermospheric temperatures on the giant planets is currently unknown (see the reviews of Yelle and Miller, 2004;

Nagy et al., 2009). As such, it is difficult to speculate about the source of the variability seen in the retrieved temperature profiles for the different occultations. The heat source itself may be temporally or spatially variable, such as an auroral or Joule-heating source at high latitudes accompanied by dynamical redistribution of that heat (e.g., Smith et al., 2007; Smith and Aylward, 2008; Müller-Wodarg et al., 2006; Müller-Wodarg et al., 2012). Waves propagating through the upper atmosphere could introduce structure to the profiles, although thermal conduction would smooth out such structures on the time scale of hours (I. Müller-Wodarg, personal communication, 2008). The major coolants H_3^+ in the thermosphere and C_2H_2 (and CH_4 , C_2H_6) in the mesopause region have abundances that vary with location and time. Given that the methane homopause level appears to vary across the planet (see Fig. 16) and that the hydrocarbons are effective coolants at these altitudes, one might expect the thermosphere to begin at lower altitudes (higher pressures) in regions where the methane homopause is lowest. There is evidence for this supposition in the retrieved profiles shown in Fig.16, but other physics is obviously playing a role as well. Overall, the variability in the thermal structure with location and/or time is not very dramatic and appears to be the most prominent at lower-thermospheric altitudes.

6 Concluding Remarks

Both the density retrievals and the forward models suggest considerable compositional and some temperature variability in the homopause region on Saturn as a function of time and/or location. The canonical view of vigorous atmospheric mixing in Saturn's middle atmosphere does not hold true for all oc-

occultations at all latitudes. The inferred pressure levels for the half-light points for the light curves at methane-sensitive wavelengths differ by as much as a factor of 70 between the Voyager occultations. These differences likely result from atmospheric dynamics. Vertical transport via either turbulent diffusion or vertical winds seems to be variable with latitude/time on Saturn, significantly altering the vertical profile of methane and the other hydrocarbons at different latitudes/times. Results from the analysis of the first Cassini UVIS stellar occultations (Shemansky and Liu, 2012; see also Nagy et al., 2009) support this view, with the inferred methane homopause level being particularly deep in the atmosphere at -42.7° latitude at the time of the UVIS δ Ori occultation.

Ultraviolet occultations provide critical atmospheric structural information in an atmospheric region difficult to probe by any other means. Our analysis suggests that UV occultations might be a particularly sensitive probe of vertical winds and/or atmospheric mixing at high altitudes. The six Voyager UVS occultations do not represent a large enough sample to provide constraints on middle atmospheric circulation on Saturn or even to make general observations with regard to latitude or seasonal trends in the methane homopause level. The two northern hemisphere occultations appear to show methane carried to higher altitudes (lower pressures) than the southern hemisphere occultations, but this observation is not statistically significant. There appears to be no correlation with time of day, despite the fact that the two occultations with the highest inferred methane homopause altitudes (i.e., Voyager 2 solar ingress and Voyager 2 stellar egress) were acquired at local dusk and slightly before midnight. Hydrocarbon chemical lifetimes are longer than a Saturn day throughout the atmosphere, so there should be no diurnal variations due to chemistry. If atmospheric tides or diurnal winds

are causing the methane concentration variability, very large vertical winds with ~ 10 meter per second diurnal variation would be required to explain the observations of the Voyager 2 solar ingress (dusk) compared with the Voyager 1 solar egress (dawn). Such strong winds are not predicted by the general circulation models (Müller-Wodarg et al., 2006; Müller-Wodarg et al., 2012; Smith et al., 2007; Smith and Aylward, 2008; Friedson and Moses, 2012), nor are they seen in the Earth's mesosphere from atmospheric tides. The most likely culprit of the observed variability is meridional circulation in the middle atmosphere, with more modest vertical winds operating over longer time scales (e.g., Conrath et al., 1990; Barnet et al., 1992; Guerlet et al., 2009, 2010; Friedson and Moses, 2012; Sinclair et al., 2013, 2014). The homopause level would be suppressed in downwelling regions and inflated in upwelling regions. Vertically propagating waves could also affect the profiles, and evidence for such waves in the middle atmosphere is provided by ground-based and Cassini mid-infrared observations (e.g., Fouchet et al., 2008; Orton et al., 2008; Guerlet et al., 2011; Li et al., 2011).

The Cassini UVIS experiment has obtained numerous solar and stellar occultations for Saturn, and results are starting to appear in the literature (Nagy et al., 2009; Shemansky and Liu, 2012; Koskinen et al., 2013). The full UVIS data set promises to reveal much more about the structure and variability of the homopause region on Saturn. Used in combination with temperature structure information and maps acquired from the Cassini radio occultations and CIRS observations, middle-atmospheric circulation patterns may be revealed for the first time on Saturn. Comparisons with our Voyager-era analysis may shed light on time-variable processes in Saturn's upper atmosphere.

Acknowledgements

We thank Bill Hubbard for providing the refractivity profiles from the ground-based observations of the 28 Sgr occultation by Saturn, as well as providing his calculations of the 1-bar radius as a function of latitude, Don Shemansky for providing the preliminary results from his analysis of the -43° latitude Cassini UVIS occultation and for helpful discussions, Tommi Koskinen and Jacques Gustin for useful conversations, and Chris Brion, Glyn Cooper, Peter Smith, and John Samson for providing their highest resolution photoabsorption cross section data. This work has benefitted from collaborative discussions during the ISSI workshop “ISSI International Team on Saturn Aeronomy, Number 166”. Support for this project was provided by NASA Planetary Atmospheres grant NAG5-11051 to The Johns Hopkins University Applied Physics Laboratory and NASA Outer Planets Research Program grant NNG05GG65G to the Lunar and Planetary Institute (LPI). J. Moses also acknowledges support from LPI during the initial stages of this project (LPI is operated by the Universities Space Research Association under contract with NASA), and for recent support from NASA OPR grant grant NNX13AK93G.

Appendix A. Sensitivity Tests: How Unique Are Forward Models?

Most of the ultraviolet occultation analyses for Saturn to date have used some kind of forward-modeling technique (Broadfoot et al., 1981a; Sandel et al., 1982b; Festou and Atreya, 1982; Smith et al., 1983; Shemansky and Liu, 2012), as well as other, sometimes simplified, equations and arguments to back out the atmospheric scale height, temperatures, and densities in the occultation

regions. Exceptions are the retrievals from Koskinen et al. (2013) and our own work. The high sensitivity of the forward models to uncertain model inputs — along with noisy data — may explain some of the differences between the derived exospheric temperature and density structure from these various groups (see section 5.3). As is discussed in section 4, the forward models are nonunique, and assumptions about the temperature variation with altitude, the atmospheric mean molecular mass and its variation with altitude, the zonal wind velocities and their variation with altitude and latitude (and other factors that influence the gravitational acceleration), and the 1-bar (or other constant pressure) radius and its variation with latitude can strongly affect the inferred properties of the occultation regions. The first three parameters — temperature, mean molecular mass, gravitational acceleration — all affect the atmospheric scale height and control how extended or compressed the atmosphere is. The last parameter (radius of geopotential surface) affects not only the assumptions about the gravity profile but also helps set the scale for the occultation observations, from which radial profiles are obtained. In this appendix, we illustrate the sensitivity of the models to certain changes in the model assumptions.

One of the main uncertainties in the models is the temperature structure in the lower atmosphere at altitudes below (or above) those in which the occultations are most sensitive. When constructing a forward model, investigators generally fix their base “reference” level at some region in which the temperature and radius are reasonably well known for some pressure level. This reference-level information is needed to set the boundary conditions for solving the hydrostatic equilibrium equation. For the giant planets, the 1-bar or 100-mbar pressure levels, the “cloud tops”, or some level defined by the light-curve

transmission have all been used for this reference level. The density-radius structure away from this base level can be derived using the hydrostatic equilibrium equation, after making assumptions about the thermal structure and other model parameters in the intervening region. In our forward models, as in those of Shemansky and Liu (2012), we use the 1-bar radius as our base level, and we build the model by making assumptions about the temperature profile from 1 bar on up to the occultation region. This procedure is particularly dangerous, as it relies on a good knowledge of all the atmospheric parameters from the 1-bar region over many scale heights up to the occultation altitudes.

Measurements of the temperature profile in Saturn's troposphere and stratosphere from Voyager RSS or IRIS observations were not obtained at the same time and location as the UVS occultations, although some overlap in the latitude coverage of the Voyager IRIS data and the UVS occultation regions does exist (e.g., Conrath and Pirraglia, 1983; Conrath et al., 1984, 1990; Conrath et al., 1998). Moreover, temperature derivations from RSS and IRIS data do not extend to pressures less than ~ 0.5 mbar, leaving gaps in our knowledge of the thermal structure. Ground-based stellar occultation observations (e.g., Hubbard et al., 1997) or high-spectral-resolution infrared observations can potentially fill these gaps, but no such observations were performed at the time of the Voyager UVS occultations. Therefore, our knowledge of the thermal structure at the occultation latitudes is sparse, and the forward models that use the 1-bar level or cloud tops as their base level are poorly constrained.

This situation is improved in the Cassini era, as numerous occultations have been recorded by Cassini UVIS (e.g., Nagy et al., 2009; Shemansky and Liu, 2012; Koskinen et al., 2013), and several other techniques and instruments are available to help constrain temperatures and atmospheric structure at

the occultation latitudes. Of particular note are the CIRS limb observations (Fouchet et al., 2008; Guerlet et al., 2009, 2010, 2011), which can reliably track stratospheric temperatures up to $\sim 10^{-2}$ mbar, and the VIMS stellar occultations (e.g., Nicholson et al., 2006; Bellucci et al., 2009; Kim et al., 2012), which should eventually help place stratospheric radius scales on a pressure grid.

For the Voyager occultations, the lack of constraints on the tropospheric and stratospheric temperatures can complicate the derivation of temperatures in the occultation regions from forward models. For example, Figure 17 shows three fictitious temperature profiles, and the resulting density structure when all other atmospheric parameters (e.g., rotation rate, mean molecular mass, latitude, 1-bar radius) are held constant. The model represented by a solid line assumes the thermal structure derived by the Cassini CIRS limb observations for -30° planetographic latitude (Guerlet et al., 2009) from 1 bar to 6×10^{-5} mbar, blending to an ad hoc thermospheric profile at pressures less than 6×10^{-5} mbar. The model represented by a dashed line uses the colder Voyager radio occultation profile as reported by Lindal (1992) for pressures greater than 0.5 mbar, but is otherwise identical to the model represented by a solid line. The model represented by a dotted line assumes a preliminary Cassini UVIS temperature profile from -42.7° latitude as reported by Shemansky et al. (2005), which has since been revised (Shemansky and Liu, 2012), from 1 bar to 7×10^{-5} mbar, but again blends into the ad hoc thermospheric profile at pressures less than 7×10^{-5} mbar. Note that the stratosphere in this model is much colder than the other two models. All model calculations were performed for -27° planetocentric latitude, assuming a 1-bar radius of 58770.6 km, an altitude-independent rotation rate of 10.55 hr

(which includes zonal winds), and an altitude-independent atmospheric mean molecular mass of 2.28 amu (10% He, 0.45% CH₄).

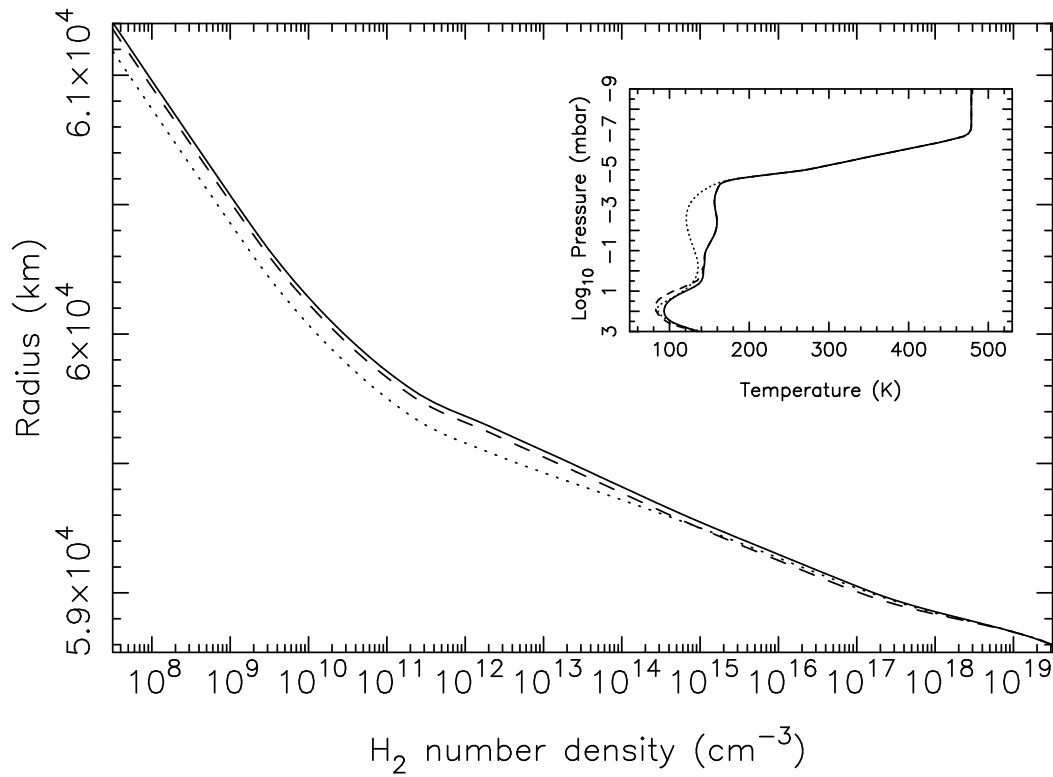


Fig. 17. The H_2 density profile derived from solving the hydrostatic equilibrium equation for three different assumptions about the temperature profile (insert). All other model parameters are held constant. Differences in the assumed temperature structure in the lower atmosphere can greatly affect densities at the higher altitudes probed by the ultraviolet occultations.

The resulting H₂ density structure for these models is shown in Fig. 17. Because of the colder stratosphere assumed for the dotted-line model, the density at any particular radius in the region typically probed by the UVS occultations (i.e., at H₂ densities less than a few times 10¹¹ cm⁻³) is much smaller in this model than the other models, despite the identical thermospheric temperature profile. The offset in radius at any particular density is about 25 km between the solid and dashed models and ~100 km between the solid and dotted models for H₂ densities probed by the UVS occultations. Similarly, at any particular radius level, the H₂ density for the dotted model can be as much as a factor of six smaller than that of the solid-line model. Assumptions about the lower-atmospheric temperature structure can clearly affect the predicted density structure when the base level is far from the occultation region.

Although the slope of the occultation light curves and/or retrieved H₂ density profile can help the forward modelers determine the exospheric temperature, the temperatures in the lower thermosphere are difficult to obtain from forward models (without additional information provided by the spectra themselves) because of uncertainties in the temperature gradients and lower-atmospheric temperatures. For example, if a forward modeler were to assume the base of the thermosphere began at higher pressures than the dotted model shown in Fig. 17, such that the rapid increase in temperature with height were located deeper in the atmosphere, then the density structure of the dotted-line model in Fig. 17 could be brought into better agreement with the other models. There is clearly a trade-off between assumptions about lower-atmospheric temperatures and assumptions about the temperature gradient in the lower thermosphere actually probed by the ultraviolet occultations — if the tropospheric and stratospheric temperatures adopted by the forward modelers are

not realistic, the resulting inferences about the lower-thermospheric temperatures will likely be in error. Similarly, the temperature gradients in the lower thermosphere are not uniquely constrained from forward models.

Such non-uniqueness problems severely curtail the usefulness of forward-modeling techniques as a means for determining temperatures in the lower regions of the thermosphere; the hybrid retrieval technique described in this paper is a more reliable method. However, if the spectral resolution of the observations were higher than that of the UVS instrument, it might be possible to exploit temperature-dependent spectral behavior to help derive temperatures through forward modeling (see the Cassini UVIS analysis and discussion of Shemansky and Liu (2012)), but without very high resolution that resolves the ro-vibrational structure in the H₂ lines, elements of non-uniqueness would likely remain.

The temperature structure is not the only model parameter that can have a large effect on the resulting density structure. The mean molecular mass also affects the atmospheric scale height, and given the uncertainties in the helium abundance and its variation with altitude on Saturn, the resulting uncertainties in the atmospheric density structure are large. Models with three different assumed mean-molecular-mass profiles are shown in Fig. 18. The models have the same temperature structure and other model parameters (see above) as shown by the solid curve in Fig. 17. For the model represented by a solid line in Fig. 18, we assume that the atmospheric mean molecular mass is constant with height, with a value 2.135 amu (i.e., 6% He, 94% H₂, no methane), as was assumed by Hubbard et al. (1997) and several other Voyager-era investigators. For the model represented by a dashed line in Fig. 18, we assume a constant value of 2.357 amu (i.e., 14% He, 0.45% CH₄, with the

rest being H₂), the upper limit from Conrath and Gautier (2000). The dotted line represents a more realistic model in which we assume a mean molecular mass of 2.278 amu (10% He and 0.45% CH₄ in the troposphere) but use a photochemistry/diffusion model to calculate the fall off in mean molecular mass with altitude due to molecular diffusion. Fig. 18 shows that the mean molecular mass can strongly influence the density structure in the models. For a constant atmospheric density of 10⁸ cm⁻³, the difference between the dotted model and the dashed model is a very large 275 km in radius. For a constant radius of 61500 km, the difference in the predicted atmospheric density between the 2.357-amu model and the others is a factor of 2.5.

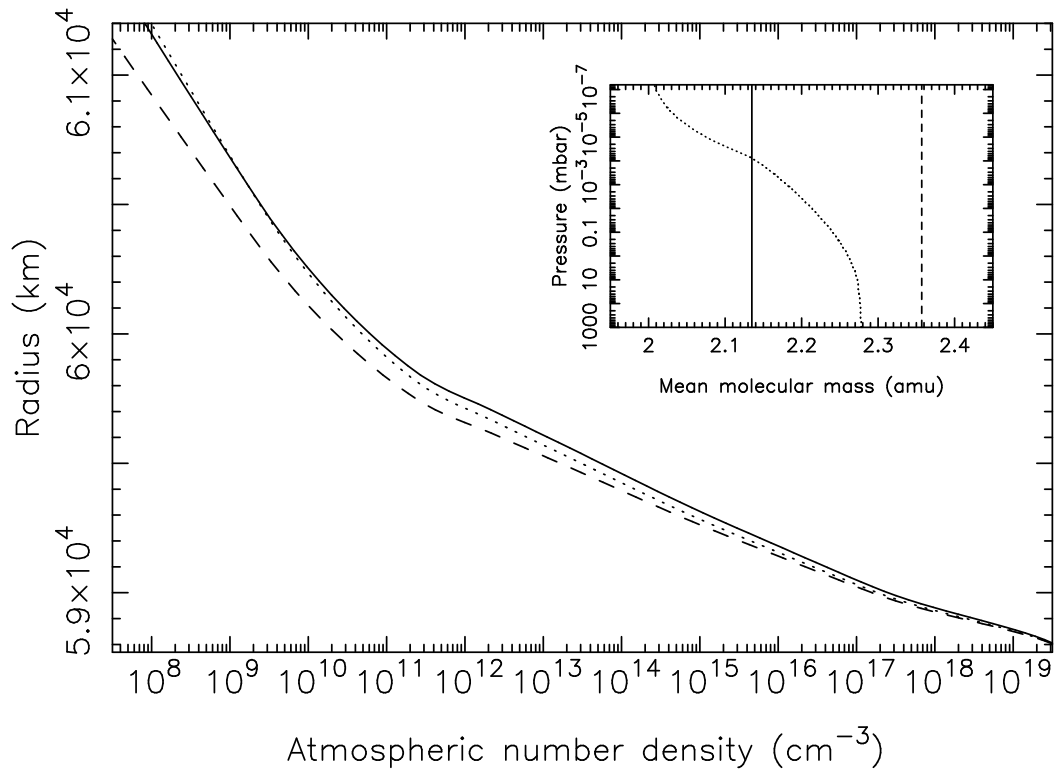


Fig. 18. The atmospheric density profile derived solving the hydrostatic equilibrium equation for three different assumptions about the atmospheric mean molecular mass profile (insert). All other model parameters are held constant. Differences in the assumed atmospheric mean molecular mass and its variation with altitude can greatly affect densities at the higher altitudes probed by the ultraviolet occultations.

An incorrect assumption about the atmospheric mean molecular mass profile can therefore lead to incorrect derivations of atmospheric densities and temperatures. An overestimate in the mean molecular mass will lead to an overestimate in the temperatures needed to derive the same H_2 density and light-curve absorption. Note that both Festou and Atreya (1982) and Smith et al. (1983) appear to assume a pure H_2 atmosphere in the thermosphere, which is a reasonable assumption for this region. However, if the actual slope of the mean molecular mass profile varies with altitude in Saturn's thermosphere, which is likely, this assumption could have an effect on the resulting derived slope for the atmospheric temperatures in this region. The assumed mean molecular mass profile will have a larger effect on models whose reference base level is far from the occultation region.

The local gravity is a third parameter that can affect the density structure in forward models (see Koskinen et al., 2013). Although the radial gravity structure is more straightforward as an input parameter in the forward models, some uncertainties do exist because of uncertainties in zonal wind speeds and their variation with height. Saturn's rapid rotation must be included in the terms for calculating the gravitational acceleration at any radius (Lindal et al., 1985), and the strong zonal winds affect the local rotation rate, especially at low latitudes on Saturn. Adopting incorrect zonal winds speeds would result in only a few km error in the atmospheric density profiles in the occultation regions provided that the base level radius is accurately constrained; however, neglecting rotation entirely in the gravity equation can lead to much larger errors, and the winds themselves strongly perturb the isobaric radius surfaces. This latter consideration is very important. As an example, the standard reference ellipsoid for Saturn assumes an equatorial radius of 60268 km and a

polar radius of 54364 km at the 1-bar level. At -45.3° planetocentric latitude, that would correspond to a 1-bar radius of 57057.6 km for the ellipsoid model, as compared with the 56947.6 km 1-bar radius derived from the Cassini radio occultation data (Paul Schinder, personal communication, 2009) — a difference of 110 km. By the same token, the 1-bar radius can change by 100 km within a one-degree latitude range at mid latitudes, which complicates forward modeling of the occultations that span a wider range of latitudes.

The overall uncertainties in the geopotential radii for Saturn can lead to relatively large uncertainties in temperature derivations from the forward models, as an offset in the radius of the base level would require a relatively large temperature adjustment to bring the H_2 densities in line with what is required from the light-curve observations. As an example, the switch from the reference ellipsoid model to a more realistic 1-bar radius as defined by the Cassini radio-science experiments, changes the temperatures derived for the Cassini UVIS -42.7° latitude occultation from 121 K to ~ 179 K at a radius of 58149 km (i.e., a 48% increase; D. Shemansky, personal communication, 2009).

The bottom line from the above discussion is that forward models cannot uniquely constrain temperatures from ultraviolet occultations in general, not unless there is some temperature-sensitive spectral behavior that can be exploited from the observations, and not unless the inputs to the models are better constrained. These limitations must always be kept in mind when considering temperatures derived from forward models.

References

- Allen, M., Yung, Y. L., Waters, J. W., 1981. Vertical transport and photochemistry in the terrestrial mesosphere and lower thermosphere (50-120 km). *J. Geophys. Res.* 86, 3617–3627.
- Atreya, S. K., 1982. Eddy mixing coefficient on Saturn. *Planet. Space Sci.* 30, 849–854.
- Atreya, S. K., Waite, Jr., J. H., Donahue, T. M., Nagy, A. F., McConnell, J. C., 1984. Theory, measurements, and models of the upper atmosphere and ionosphere of Saturn. In: Gehrels, T., Matthews, M. S. (Eds.), *Saturn*. The University of Arizona Press, Tucson, pp. 239–277.
- Au, J. W., Cooper, G., Burton, G. R., Olney, T. N., Brion, C. E., 1993. The valence shell photoabsorption of the linear alkanes, C_nH_{2n+2} ($n=1-8$): absolute oscillator strengths (7–220 eV). *Chem. Phys.* 173, 209–239.
- Barnet, C. D., Beebe, R. F., Conrath, B. J., 1992. A seasonal radiative-dynamic model of Saturn's troposphere. *Icarus* 98, 94–107.
- Bellucci, A., Sicardy, B., Drossart, P., Rannou, P., Nicholson, P. D., Hedman, M., Baines, K. H., Burrati, B., 2009. Titan solar occultation observed by Cassini/VIMS: Gas absorption and constraints on aerosol composition. *Icarus* 201, 198–216.
- Ben Jaffel, L., Prangé, R., Sandel, B. R., Yelle, R. V., Emerich, C., Feng, D., Hall, D. T., 1995. New analysis of the Voyager UVS H Lyman-alpha emission of Saturn. *Icarus* 113, 91–102.
- Bevington, P. R., Robinson, D. K., 1992. *Data Reduction and Error Analysis for the Physical Sciences*, 2nd Edition. McGraw-Hill, New York.
- Bézar, B., Greathouse, T., Lacy, J., Richter, M., Moses, J., Griffith, C., 2002. High spectral resolution observations of Jupiter and Saturn near 10 micron:

- Ethylene and the $\text{CH}_3\text{D}/\text{CH}_4$ ratio. In: Jupiter after Galileo and Cassini Meeting Abstracts, Lisbon, 17-21 June.
- Bézar, B., Griffith, C. A., Kelly, D. M., Lacy, J. H., Greathouse, T., Orton, G., 1997. Thermal infrared imaging spectroscopy of Shoemaker-Levy 9 impact sites: Temperatures and HCN retrievals. *Icarus* 125, 94–120.
- Broadfoot, A. L., Sandel, B. R., 1977. Self-scanned anode array with a microchannel plate electron multiplier: the SSANACON. *Appl. Opt.* 16, 1533–1538.
- Broadfoot, A. L., Sandel, B. R., Shemansky, D. E., Atreya, S. K., Donahue, T. M., Moos, H. W., Bertaux, J. L., Blamont, J. E., Ajello, J. M., Strobel, D. F., McConnell, J. C., Dalgarno, A., Goody, R., McElroy, M. B., Yung, Y. L., 1977. Ultraviolet spectrometer experiment for the Voyager mission. *Space Sci. Rev.* 21, 183–205.
- Broadfoot, A. L., Sandel, B. R., Shemansky, D. E., Holberg, J. B., Smith, G. R., Strobel, D. F., McConnell, J. C., Kumar, S., Hunten, D. M., Atreya, S. K., Donahue, T. M., Moos, H. W., Bertaux, J. L., Blamont, J. E., Pomphrey, R. B., Linick, S., 1981a. Extreme ultraviolet observations from Voyager 1 encounter with Saturn. *Science* 212, 206–211.
- Broadfoot, A. L., Sandel, B. R., Shemansky, D. E., McConnell, J. C., Smith, G. R., Holberg, J. B., Atreya, S. K., Donahue, T. M., Strobel, D. F., Bertaux, J. L., 1981b. Overview of the Voyager ultraviolet spectrometry results through Jupiter encounter. *J. Geophys. Res.* 86, 8259–8284.
- Chan, W. F., Cooper, G., Brion, C. E., 1992. Absolute optical oscillator strengths (11–20 eV) and transition moments for the photoabsorption of molecular hydrogen in the Lyman and Werner bands. *Chem. Phys.* 168, 375–388.
- Chen, F., Judge, D. L., Wu, C. Y. R., Caldwell, J., White, H. P., Wagener,

- R., 1991. High-resolution, low-temperature photoabsorption cross sections of C_2H_2 , PH_3 , AsH_3 , and GeH_4 , with application to Saturn's atmosphere. *J. Geophys. Res.* 96, 17,519–17,527.
- Conrath, B. J., Gautier, D., 2000. Saturn helium abundance: A reanalysis of Voyager measurements. *Icarus* 144, 124–134.
- Conrath, B. J., Gautier, D., Hanel, R. A., Hornstein, J. S., 1984. The helium abundance of Saturn from Voyager measurements. *Astrophys. J.* 282, 807–815.
- Conrath, B. J., Gierasch, P. J., Leroy, S. S., 1990. Temperature and circulation in the stratosphere of the outer planets. *Icarus* 83, 255–281.
- Conrath, B. J., Gierasch, P. J., Ustinov, E. A., 1998. Thermal structure and para hydrogen fraction on the outer planets from Voyager IRIS measurements. *Icarus* 135, 501–517.
- Conrath, B. J., Pirraglia, J. A., 1983. Thermal structure of Saturn from Voyager infrared measurements - implications for atmospheric dynamics. *Icarus* 53, 286–292.
- Cooper, G., Burton, G. R., Brion, C. E., 1995a. Absolute UV and soft X-ray photoabsorption of acetylene by high resolution dipole (e,e) spectroscopy. *J. Electron Spectrosc. Relat. Phenom.* 73, 139–148.
- Cooper, G., Olney, T. N., Brion, C. E., 1995b. Absolute UV and soft X-ray photoabsorption of ethylene by high resolution dipole (e,e) spectroscopy. *Chem. Phys.* 194, 175–184.
- Cooray, A. R., Elliot, J. L., Bosh, A. S., Young, L. A., Shure, M. A., 1998. Stellar occultation observations of Saturn's north-polar temperature structure. *Icarus* 132, 298–310.
- Courtin, R., Gautier, D., Marten, A., Bezard, B., Hanel, R., 1984. The composition of Saturn's atmosphere at northern temperate latitudes from Voyager

- IRIS spectra: NH_3 , PH_3 , C_2H_2 , C_2H_6 , CH_3D , CH_4 , and the Saturnian D/H isotopic ratio. *Astrophys. J.* 287, 899–916.
- Dalgarno, A., Allison, A. C., 1969. Photodissociation of molecular hydrogen on Venus. *J. Geophys. Res.* 74, 4178–4180.
- Dobrijevic, M., Cavalié, T., Billebaud, F., 2011. A methodology to construct a reduced chemical scheme for 2D-3D photochemical models: Application to Saturn. *Icarus* 214, 275–285.
- Dobrijevic, M., Ollivier, J. L., Billebaud, F., Brillet, J., Parisot, J. P., 2003. Effect of chemical kinetic uncertainties on photochemical modeling results: Application to Saturn’s atmosphere. *Astron. Astrophys.* 398, 335–344.
- Emerich, C., Jaffel, L. B., Prangé, R., 1993. On the analysis of the H Lyman-alpha dayglow of Jupiter, Saturn, and Uranus. *Planet. Space Sci.* 41, 363–371.
- Feng, D. D., Ben-Jaffel, L., Herbert, F. L., Herman, B. M., 2005. Water and hydrocarbon distributions in Saturn’s upper atmosphere. *Eos Trans. AGU* 86(52), fall Meet. Suppl., Abstract #P11C-0131.
- Feng, D. S., 1991. Recovering the hydrocarbon distributions in Saturn’s upper atmosphere through mathematical inversion. Ph.D. dissertation, The University of Arizona, Tucson.
- Festou, M. C., Atreya, S. K., 1982. Voyager ultraviolet stellar occultation measurements of the composition and thermal profiles of the saturnian upper atmosphere. *Geophys. Res. Lett.* 9, 1147–1150.
- Festou, M. C., Atreya, S. K., Donahue, T. M., Sandel, B. R., Shemansky, D. E., Broadfoot, A. L., 1981. Composition and thermal profiles of the jovian upper atmosphere determined by the Voyager ultraviolet stellar occultation experiment. *J. Geophys. Res.* 86, 5715–5725.
- Flasar, F. M., Achterberg, R. K., Conrath, B. J., Pearl, J. C., Bjoraker, G. L.,

- Jennings, D. E., Romani, P. N., Simon-Miller, A. A., Kunde, V. G., Nixon, C. A., Bézard, B., Orton, G. S., Spilker, L. J., Spencer, J. R., Irwin, P. G. J., Teanby, N. A., Owen, T. C., Brasunas, J., Segura, M. E., Carlson, R. C., Mamoutkine, A., Gierasch, P. J., Schinder, P. J., Showalter, M. R., Ferrari, C., Barucci, A., Courtin, R., Coustenis, A., Fouchet, T., Gautier, D., Lellouch, E., Marten, A., Prangé, R., Strobel, D. F., Calcutt, S. B., Read, P. L., Taylor, F. W., Bowles, N., Samuelson, R. E., Abbas, M. M., Raulin, F., Ade, P., Edgington, S., Pilorz, S., Wallis, B., Wishnow, E. H., 2005. Temperatures, winds, and composition in the Saturn system. *Science* 307, 1247–1251.
- Flasar, F. M., Schinder, P. J., Achterberg, R. K., Conrath, B. J., Team, C. I., Team, C., 2008. On combining thermal-infrared and radio-occultation data of Saturn and Titan's. *Bull. Am. Astron. Soc.* 40, #53.07.
- Fletcher, L. N., Achterberg, R. K., Greathouse, T. K., Orton, G. S., Conrath, B. J., Simon-Miller, A. A., Teanby, N., Guerlet, S., Irwin, P. G. J., Flasar, F. M., 2010. Seasonal change on Saturn from Cassini/CIRS observations, 2004-2009. *Icarus* 208, 337–352.
- Fletcher, L. N., Irwin, P. G. J., Orton, G. S., Teanby, N. A., Achterberg, R. K., Bjoraker, G. L., Read, P. L., Simon-Miller, A. A., Howett, C., de Kok, R., Bowles, N., Calcutt, S. B., Hesman, B., Flasar, F. M., 2008. Temperature and composition of Saturn's polar hot spots and hexagon. *Science* 319, 79–81.
- Fletcher, L. N., Irwin, P. G. J., Teanby, N. A., Orton, G. S., Parrish, P. D., de Kok, R., Howett, C., Calcutt, S. B., Bowles, N., Taylor, F. W., 2007. Characterising Saturn's vertical temperature structure from Cassini/CIRS. *Icarus* 189, 457–478.
- Fletcher, L. N., Orton, G. S., Teanby, N. A., Irwin, P. G. J., Bjoraker, G. L.,

2009. Methane and its isotopologues on Saturn from Cassini/CIRS observations. *Icarus* 199, 351–367.
- Ford, A. L., Browne, J. C., 1973. Rayleigh and Raman cross sections for the hydrogen molecule. *Atomic Data* 5, 305–313.
- Fouchet, T., Guerlet, S., Strobel, D. F., Simon-Miller, A. A., Bézard, B., Flasar, F. M., 2008. An equatorial oscillation in Saturn’s middle atmosphere. *Nature* 453, 200–202.
- Fouchet, T., Moses, J. I., Conrath, B. J., 2009. Saturn: Composition and chemistry. In: Dougherty, M. K., Esposito, L. W., Krimigis, S. M. (Eds.), *Saturn from Cassini-Huygens*. Springer, Dordrecht, pp. 83–112.
- French, R. G., Harrington, J., Nicholson, P. D., Stecklum, B., Sicardy, B., Lacombe, F., Matthews, K., 1999. Three stellar occultations by the Saturn system in 1998. In: *AAS/Division for Planetary Sciences Meeting Abstracts*. Vol. 31. #55.04.
- Friedson, A. J., Moses, J. I., 2012. General circulation and transport in Saturn’s upper troposphere and stratosphere. *Icarus* 218, 861–875.
- Geballe, T. R., Jagod, M.-F., Oka, T., 1993. Detection of H_3^+ infrared emission lines in Saturn. *Astrophys. J. Lett.* 408, L109–L112.
- Gérard, J.-C., Bonfond, B., Gustin, J., Grodent, D., Clarke, J. T., Bisikalo, D., Shematovich, V., 2009. Altitude of Saturn’s aurora and its implications for the characteristic energy of precipitated electrons. *Geophys. Res. Lett.* 36, L02202.
- Gérard, J. C., Dols, V., Grodent, D., Waite, J. H., Gladstone, G. R., Prangé, R., 1995. Simultaneous observations of the saturnian aurora and polar haze with the HST/FOC. *Geophys. Res. Lett.* 22, 2685–2688.
- Gérard, J.-C., Grodent, D., Gustin, J., Saglam, A., Clarke, J. T., Trauger, J. T., 2004. Characteristics of Saturn’s FUV aurora observed with the

- Space Telescope Imaging Spectrograph. *J. Geophys. Res.* 109, A09207, doi:10.1029/2004JA010513.
- Greathouse, T. K., Gladstone, G. R., Moses, J. I., Stern, S. A., Retherford, K. D., Vervack, R. J., Slater, D. C., Versteeg, M. H., Davis, M. W., Young, L. A., Steffl, A. J., Throop, H., Parker, J. W., 2010. New Horizons Alice ultraviolet observations of a stellar occultation by Jupiter's atmosphere. *Icarus* 208, 293–305.
- Greathouse, T. K., Lacy, J. H., Bézard, B., Moses, J. I., Griffith, C. A., Richter, M. J., 2005. Meridional variations of temperature, C₂H₂ and C₂H₆ abundances in Saturn's stratosphere at southern summer solstice. *Icarus* 177, 18–31.
- Guerlet, S., Fouchet, T., Bézard, B., Flasar, F. M., Simon-Miller, A. A., 2011. Evolution of the equatorial oscillation in Saturn's stratosphere between 2005 and 2010 from Cassini/CIRS limb data analysis. *Geophys. Res. Lett.* 38, L09201.
- Guerlet, S., Fouchet, T., Bézard, B., Moses, J. I., Fletcher, L. N., Simon-Miller, A. A., Flasar, F. M., 2010. Meridional distribution of CH₃C₂H and C₄H₂ in Saturn's stratosphere from CIRS/Cassini limb and nadir observations. *Icarus* 209, 682–695.
- Guerlet, S., Fouchet, T., Bézard, B., Simon-Miller, A. A., Fletcher, L. N., Simon-Miller, A. A., Flasar, F. M., 2009. Vertical and meridional distribution of ethane, acetylene and propane in Saturn's stratosphere from CIRS/Cassini limb observations. *Icarus* 203, 214–232.
- Gustin, J., Gérard, J.-C., Pryor, W., Feldman, P. D., Grodent, D., Holsclaw, G., 2009. Characteristics of Saturn's polar atmosphere and auroral electrons derived from HST/STIS, FUSE and Cassini/UVIS spectra. *Icarus* 200, 176–187.

- Gustin, J., Moses, J. I., Gerard, J. M., dec 2012. Saturn temperature profiles at low, medium and high latitudes derived from UVIS EUV solar occultations. AGU Fall Meeting Abstracts, B2257.
- Hallett, J. T., Shemansky, D. E., Liu, X., 2005a. Comparison of recent Cassini UVIS observations of Saturn H₂ dayglow emission. EOS Trans. AGU 86, Fall Meet. Suppl., Abstract #P11C-0127.
- Hallett, J. T., Shemansky, D. E., Liu, X., 2005b. A rotational-level hydrogen physical chemistry model for general astrophysical application. *Astrophys. J.* 624, 448–461.
- Harrington, J., French, R. G., Matcheva, K., 2010. The 1998 November 14 occultation of GSC 0622-00345 by Saturn. II. Stratospheric thermal profile, power spectrum, and gravity waves. *Astrophys. J.* 716, 404–416.
- Hinteregger, H. E., Fukui, K., Gilson, B. R., 1981. Observational, reference and model data on solar EUV, from measurements on AE-E. *Geophys. Res. Lett.* 8, 1147–1150.
- Ho, G. H., Lin, M. S., Wang, Y. L., Chang, T. W., 1998. Photoabsorption and photoionization of propyne. *J. Chem. Phys.* 109, 5868–5879.
- Holberg, J. B., Forrester, W. T., Shemansky, D. E., Barry, D. C., 1982. *Voyager* absolute far-ultraviolet spectrophotometry of hot stars. *Astrophys. J.* 257, 656–671.
- Hubbard, W. B., Hammerle, V., Porco, C. C., Rieke, G. H., Rieke, M. J., 1995. The occultation of SAO 78505 by Jupiter. *Icarus* 113, 103–109.
- Hubbard, W. B., Porco, C. C., Hunten, D. M., Rieke, G. H., Rieke, M. J., McCarthy, D. W., Haemmerle, V., Haller, J., McLeod, B., Lebofsky, L. A., Marcialis, R., Holberg, J. B., Landau, R., Carrasco, L., Elias, J., Buie, M. W., Dunham, E. W., Persson, S. E., Boroson, T., West, S., French, R. G., Harrington, J., Elliot, J. L., Forrest, W. J., Pipher, J. L., Stover,

- R. J., Brahic, A., Grenier, I., 1997. Structure of Saturn's mesosphere from the 28 Sgr occultations. *Icarus* 130, 404–425.
- Ingersoll, A. P., Beebe, R. F., Conrath, B. J., Hunt, G. E., 1984. Structure and dynamics of Saturn's atmosphere. In: Gehrels, T., Matthews, M. S. (Eds.), *Saturn*. The University of Arizona Press, Tucson, pp. 195–238.
- Karkoschka, E., Tomasko, M. G., 1992. Saturn's upper troposphere 1986-1989. *Icarus* 97, 161–181.
- Kerola, D. X., Larson, H. P., Tomasko, M. G., 1997. Analysis of the near-IR spectrum of Saturn: A comprehensive radiative transfer model of its middle and upper troposphere. *Icarus* 127, 190–212.
- Killen, R. M., 1988. Longitudinal variations in the Saturnian atmosphere. i - Equatorial region. *Icarus* 73, 227–247.
- Kim, S. J., Sim, C. K., Lee, D. W., Courtin, R., Moses, J. I., Minh, Y. C., 2012. The three-micron spectral feature of the Saturnian haze: Implications for the haze composition and formation process. *Planet. Space Sci.* 65, 122–129.
- Koskinen, T. T., Sandel, B. R., Yelle, R. V., Capalbo, F. J., Holsclaw, G. M., McClintock, W. E., Edgington, S., 2013. The density and temperature structure near the exobase of saturn from Cassini UVIS solar occultations. *Icarus* 226, 1318–1330.
- Lellouch, E., Bézard, B., Fouchet, T., Feuchtgruber, H., Encrenaz, T., de Graauw, T., 2001. The deuterium abundance in Jupiter and Saturn from ISO-SWS observations. *Astron. Astrophys.* 370, 610–622.
- Li, L., Achterberg, R. K., Conrath, B. J., Gierasch, P. J., Smith, M. A., Simon-Miller, A. A., Nixon, C. A., Orton, G. S., Flasar, F. M., Jiang, X., Baines, K. H., Morales-Juberías, R., Ingersoll, A. P., Vasavada, A. R., Del Genio, A. D., West, R. A., Ewald, S. P., 2013. Strong temporal variation over one Saturnian year: From Voyager to Cassini. *Scientific Reports* 3, 2410.

- Li, L., Jiang, X., Ingersoll, A. P., Del Genio, A. D., Porco, C. C., West, R. A., Vasavada, A. R., Ewald, S. P., Conrath, B. J., Gierasch, P. J., Simon-Miller, A. A., Nixon, C. A., Achterberg, R. K., Orton, G. S., Fletcher, L. N., Baines, K. H., 2011. Equatorial winds on Saturn and the stratospheric oscillation. *Nature Geoscience* 4, 750–752.
- Liming, L., Gierasch, P. J., Achterberg, R. K., Conrath, B. J., Flasar, F. M., Vasavada, A. R., Ingersoll, A. P., Banfield, D., Simon-Miller, A. A., Fletcher, L. N., 2008. Strong jet and a new thermal wave in Saturn’s equatorial stratosphere. *Geophys. Res. Lett.* 35, L23208.
- Lindal, G. F., 1992. The atmosphere of Neptune - an analysis of radio occultation data acquired with Voyager 2. *Astron. J.* 103, 967–982.
- Lindal, G. F., Sweetnam, D. N., Eshleman, V. R., 1985. The atmosphere of Saturn: An analysis of the Voyager radio occultation measurements. *Astron. J.* 90, 1136–1146.
- Liu, W., Dalgarno, A., 1996. The ultraviolet spectrum of the Jovian dayglow. *Astrophys. J.* 462, 502–518.
- Marrero, T. R., Mason, E. A., 1972. Gaseous diffusion coefficients. *J. Phys. Chem. Ref. Data* 1, 3–118.
- Marten, A., DeBergh, C., Owen, T., Gautier, D., Maillard, J. P., Drossart, P., Lutz, B., Orton, G. S., 1994. Four micron high-resolution spectra of Jupiter in the North Equatorial Belt: H_3^+ emissions and the $^{12}\text{C}/^{13}\text{C}$ ratio. *Planet Space Sci.* 42, 391–399.
- McGrath, M. A., Clarke, J. T., 1992. H I Lyman alpha emission from Saturn (1980-1990). *J. Geophys. Res.* 97, 13,691–13,703.
- Melin, H., Miller, S., Stallard, T., Trafton, L. M., Geballe, T. R., 2007. Variability in the H_3^+ emission of Saturn: Consequences for ionisation rates and temperature. *Icarus* 186, 234–241.

- Melin, H., Stallard, T., Miller, S., Gustin, J., Galand, M., Badman, S. V., Pryor, W. R., O'Donoghue, J., Brown, R. H., Baines, K. H., 2011. Simultaneous Cassini VIMS and UVIS observations of Saturn's southern aurora: Comparing emissions from H, H₂ and H₃⁺ at a high spatial resolution. *Geophys. Res. Lett.* 38, L15203.
- Menke, W., 1989. *Geophysical Data Analysis: Discrete Inverse Theory*. Academic Press, New York.
- Miller, S., Achilleos, N., Ballester, G. E., Geballe, T. R., Joseph, R. D., Prangé, R., Rego, D., Stallard, T., Tennyson, J., Trafton, L. M., Waite, Jr., J. H., 2000. The role of H₃⁺ in planetary atmospheres. *Phil. Trans. Roy. Soc.* 358, 2485–2502.
- Moses, J. I., Bézard, B., Lellouch, E., Gladstone, G. R., Feuchtgruber, H., Allen, M., 2000. Photochemistry of Saturn's atmosphere. I. Hydrocarbon chemistry and comparisons with ISO observations. *Icarus* 143, 244–298.
- Moses, J. I., Fouchet, T., Bézard, B., Gladstone, G. R., Lellouch, E., Feuchtgruber, H., 2005. Photochemistry and diffusion in Jupiter's stratosphere: Constraints from ISO observations and comparisons with other giant planets. *J. Geophys. Res.* 110, E08001, doi:10.1029/2005JE002411.
- Moses, J. I., Greathouse, T. K., 2005. Latitudinal and seasonal models of stratospheric photochemistry on Saturn: Comparison with infrared data from IRTF/TEXES. *J. Geophys. Res.* 110, E09007, doi:10.1029/2005JE002450.
- Mount, G. H., Moos, H. W., 1978. Photoabsorption cross sections of methane and ethane, 1300–1600 Å, at $T = 295$ K and $T = 200$ K. *Astrophys. J. Lett.* 224, L35–L38.
- Mount, G. H., Warden, E. S., Moos, H. W., 1977. Photoabsorption cross sections of methane from 1400 to 1850 Å. *Astrophys. J. Lett.* 214, L47–L49.

- Müller-Wodarg, I. C. F., Mendillo, M., Yelle, R. V., Aylward, A. D., 2006. A global circulation model of Saturn's thermosphere. *Icarus* 180, 147–160.
- Müller-Wodarg, I. C. F., Moore, L., Galand, M., Miller, S., Mendillo, M., 2012. Magnetosphere-atmosphere coupling at Saturn: 1 - Response of thermosphere and ionosphere to steady state polar forcing. *Icarus* 221, 481–494.
- Nagy, A. F., Kliore, A. J., Mendillo, M., Miller, S., Moore, L., Moses, J. I., Müller-Wodarg, I., Shemansky, D., 2009. Upper atmosphere and ionosphere of Saturn. In: Dougherty, M. K., Esposito, L. W., Krimigis, S. M. (Eds.), *Saturn from Cassini-Huygens*. Springer, Dordrecht, pp. 181–201.
- Nicholson, P. D., Cooke, M. L., Pelton, E., 1990. An absolute radius scale for Saturn's rings. *Astron. J.* 100, 1339–1362.
- Nicholson, P. D., Hedman, M. M., Gierasch, P. J., Cassini VIMS Team, 2006. Probing Saturn's atmosphere with Procyon. In: *AAS/Division for Planetary Sciences Meeting Abstracts*. Vol. 38. p. 555.
- Nicholson, P. D., Porco, C. C., 1988. A new constraint on Saturn's zonal gravity harmonics from Voyager observations of an eccentric ringlet. *J. Geophys. Res.* 93, 10,209–10,224.
- Noll, K. S., Knacke, R. F., Tokunaga, A. T., Lacy, J. H., Beck, S., Serabyn, E., 1986. The abundances of ethane and acetylene in the atmospheres of Jupiter and Saturn. *Icarus* 65, 257–263.
- O'Donoghue, J., Stallard, T. S., Melin, H., Cowley, S. W. H., Badman, S. V., Moore, L., Miller, S., Tao, C., Baines, K. H., Blake, J. S. D., 2014. Conjugate observations of Saturn's northern and southern H_3^+ aurorae. *Icarus* 229, 214–220.
- O'Donoghue, J., Stallard, T. S., Melin, H., Jones, G. H., Cowley, S. W. H., Miller, S., Baines, K. H., Blake, J. S. D., 2013. The domination of Saturn's low-latitude ionosphere by ring 'rain'. *Nature* 496, 193–195.

- Okabe, H., 1983. Photochemistry of acetylene. *Can. J. Chem.* 61, 850–855.
- Ollivier, J. L., Dobrijévic, M., Parisot, J. P., 2000. New photochemical model of Saturn's atmosphere. *Planet. Space Sci.* 48, 699–716.
- Orkin, V. L., Huie, R. E., Kurylo, J., 1997. Rate constants for the reactions of OH with HFC-245cb ($\text{CH}_3\text{CF}_2\text{CF}_3$) and some fluoroalkenes (CH_2CHCF_3 , $\text{CH}_2\text{CF}_2\text{CF}_3$, CF_2CF_2). *J. Phys. Chem. A* 101, 9118–9124.
- Orton, G. S., Yanamandra-Fisher, P. A., Fisher, B. M., Friedson, A. J., Parrish, P. D., Nelson, J. F., Bauermeister, A. S., Fletcher, L., Gezari, D. Y., Varosi, F., Tokunaga, A. T., Caldwell, J., Baines, K. H., Hora, J. L., Ressler, M. E., Fujiyoshi, T., Fuse, T., Hagopian, H., Martin, T. Z., Bergstralh, J. T., Howett, C., Hoffmann, W. F., Deutsch, L. K., Cleve, J. E. V., Noe, E., Adams, J. D., Kassis, M., Tollestrup, E., 2008. Semi-annual oscillations in Saturn's low-latitude stratospheric temperatures. *Nature* 453, 196–199.
- Parkinson, C. D., Griffioen, E., McConnell, J. C., Gladstone, G. R., Sandel, B. R., 1998. He 584 Å daylow at Saturn: A reassessment. *Icarus* 133, 210–220.
- Press, W. H., Teukolsky, S. A., Vetterling, W. T., Flannery, B. P., 1992. *Numerical Recipes in FORTRAN*, 2nd Edition. Cambridge University Press, New York.
- Reid, R. C., Prausnitz, J. M., Poling, B. E., 1987. *The Properties of Gases and Liquids*. McGraw-Hill, New York.
- Sada, P. V., Bjoraker, G. L., Jennings, D. E., Romani, P. N., McCabe, G. H., 2005. Observations of C_2H_6 and C_2H_2 in the stratosphere of Saturn. *Icarus* 173, 499–507.
- Sada, P. V., McCabe, G. H., Bjoraker, G. L., Jennings, D. E., Reuter, D. C., 1996. ^{13}C -ethane in the atmospheres of Jupiter and Saturn. *Astrophys. J.* 472, 903–907.

- Sadeghpour, H. R., Dalgarno, A., 1992. Rayleigh and Raman scattering by hydrogen and caesium. *J. Phys. B: At. Mol. Opt. Phys.* 25, 4801–4809.
- Samson, J. A. R., 1966. The measurement of the photoionization cross sections of the atomic gases. *Adv. At. Mol. Phys.* 2, 177–261.
- Samson, J. A. R., Haddad, G. N., 1994. Total photoabsorption cross sections of H₂ from 18 to 113 eV. *J. Opt. Soc. Am. B* 11, 277–279.
- Samson, J. A. R., Haddad, G. N., Masuoka, T., Pareek, P. N., Kilcoyne, D. A. L., 1989. Ionization yields, total absorption, and dissociative photoionization cross sections of CH₄ from 110–950 Å. *J. Chem. Phys.* 90, 6925–6932.
- Samson, J. A. R., Marmo, F. F., Watanabe, K., 1962. Absorption and photoionization coefficients of propylene and butene-1 in the vacuum ultraviolet. *J. Chem. Phys.* 36, 783–786.
- Sanchez-Lavega, A., Rojas, J. F., Sada, P. V., 2000. Saturn zonal winds at cloud level. *Icarus* 147, 405–420.
- Sandel, B. R., McConnell, J. C., Strobel, D. F., 1982a. Eddy diffusion at Saturn’s homopause. *Geophys. Res. Lett.* 9, 1077–1080.
- Sandel, B. R., Shemansky, D. E., Broadfoot, A. L., Holberg, J. B., Smith, G. R., McConnell, J. C., Strobel, D. F., Atreya, S. K., Donahue, T. M., Moos, H. W., Hunten, D. M., Pomphrey, R. B., Linick, S., 1982b. Extreme ultraviolet observations from the Voyager 2 encounter with Saturn. *Science* 215, 548–553.
- Seiff, A., Kirk, D. B., Knight, T. C. D., Young, L. A., Milos, F. S., Venkatapathy, E., Mihalov, J. D., Blanchard, R. C., Young, R. E., Schubert, G., 1997. Thermal structure of Jupiter’s upper atmosphere derived from the Galileo probe. *Science* 276, 102–104.
- Shemansky, D. E., Hallett, J. T., Liu, X., 2005. The first Cassini UVIS stellar occultation of the Saturn atmosphere. *EOS Trans. AGU* 86, Fall Meet.

- Suppl., Abstract #P23D-04.
- Shemansky, D. E., Liu, X., 2012. Saturn upper atmospheric structure from Cassini EUV and FUV occultations. *Canadian Journal of Physics* 90, 817–831.
- Sinclair, J. A., Irwin, P. G. J., Fletcher, L. N., Greathouse, T., Guerlet, S., Hurley, J., Merlet, C., 2014. From Voyager-IRIS to Cassini-CIRS: Interannual variability in Saturn’s stratosphere? *Icarus* 233, 281–292.
- Sinclair, J. A., Irwin, P. G. J., Fletcher, L. N., Moses, J. I., Greathouse, T. K., Friedson, A. J., Hesman, B., Hurley, J., Merlet, C., 2013. Seasonal variations of temperature, acetylene and ethane in Saturn’s atmosphere from 2005 to 2010, as observed by Cassini-CIRS. *Icarus* 225, 257–271.
- Smith, C. G. A., Aylward, A. D., 2008. Coupled rotational dynamics of Saturn’s thermosphere and magnetosphere: a thermospheric modelling study. *Annales Geophysicae* 26, 1007–1027.
- Smith, C. G. A., Aylward, A. D., Millward, G. H., Miller, S., Moore, L. E., 2007. An unexpected cooling effect in Saturn’s upper atmosphere. *Nature* 445, 399–401.
- Smith, G. P., 2003. Rate theory of methyl recombination at the low temperatures and pressures of planetary atmospheres. *Chem. Phys. Lett.* 376, 381–388.
- Smith, G. R., Hunten, D. M., 1990. Study of planetary atmospheres by absorptive occultations. *Rev. Geophys.* 28, 117–143.
- Smith, G. R., Shemansky, D. E., Holberg, J. B., Broadfoot, A. L., Sandel, B. R., McConnell, J. C., 1983. Saturn’s upper atmosphere from the Voyager 2 EUV solar and stellar occultations. *J. Geophys. Res.* 88, 8667–8678.
- Smith, G. R., Strobel, D. F., Broadfoot, A. L., Sandel, B. R., Shemansky, D. E., Holberg, J. B., 1982. Titan’s upper atmosphere: Composition and

- temperature from the EUV solar occultation results. *J. Geophys. Res.* 87, 1351–1359.
- Smith, P. L., Yoshino, K., Parkinson, W. H., Ito, K., Stark, G., 1991. High-resolution, VUV (147–201 nm) photoabsorption cross sections for C₂H₂ at 195 and 295 K. *J. Geophys. Res.* 96, 17,529–17,533.
- Stallard, T. S., Melin, H., Miller, S., O’Donoghue, J., Cowley, S. W. H., Badman, S. V., Adriani, A., Brown, R. H., Baines, K. H., 2012. Temperature changes and energy inputs in giant planet atmospheres: what we are learning from H₃⁺. *Royal Society of London Philosophical Transactions Series A* 370, 5213–5224.
- Suto, M., Lee, L. C., 1984. Quantitative photoexcitation and fluorescence studies of C₂H₂ in vacuum ultraviolet. *J. Chem. Phys.* 80, 4824–4831.
- Tomasko, M. G., Doose, L. R., 1984. Polarimetry and photometry of Saturn from Pioneer 11 observations and constraints on the distribution and properties of cloud and aerosol particles. *Icarus* 58, 1–34.
- Trafton, L., 1985. Long-term changes in Saturn’s troposphere. *Icarus* 63, 374–405.
- Twomey, S., 1977. *Introduction to the Mathematics of Inversion in Remote Sensing and Indirect Measurements*. Elsevier, New York.
- Vervack, Jr., R. J., 1997. Titan’s upper atmospheric structure derived from Voyager ultraviolet spectrometer observations. Ph.D. dissertation, The University of Arizona, Tucson.
- Vervack, Jr., R. J., Sandel, B. R., Strobel, D. F., 2004. New perspectives on Titan’s upper atmosphere from a reanalysis of the Voyager 1 UVS solar occultations. *Icarus* 170, 91–112.
- Waite, J. H., Young, D. T., Cravens, T. E., Coates, A. J., Crary, F. J., Magee, B., Westlake, J., 2007. The process of tholin formation in Titan’s upper

- atmosphere. *Science* 316, 870.
- Waite, Jr., J. H., Niemann, H., Yelle, R. V., Kasprzak, W. T., Cravens, T. E., Luhmann, J. G., McNutt, R. L., Ip, W.-H., Gell, D., Haye, V. D. L., Müller-Wordag, I., Magee, B., Borggren, N., Ledvina, S., Fletcher, G., Walter, E., Miller, R., Scherer, S., Thorpe, R., Xu, J., Block, B., Arnett, K., 2004. Ion neutral mass spectrometer results from the first flyby of Titan. *Science* 308, 982–986.
- Xia, T. J., Chien, T. S., Wu, C. Y. R., Judge, D. L., 1991. Photoabsorption and photoionization cross sections of NH_3 , PH_3 , H_2S , C_2H_2 , and C_2H_4 in the VUV region. *J. Quant. Spectrosc. Radiat. Transfer* 45, 77–91.
- Yelle, R. V., Griffith, C. A., Young, L. A., 2001. Structure of the jovian stratosphere at the Galileo probe entry site. *Icarus* 152, 331–346.
- Yelle, R. V., Herbert, F., Sandel, B. R., Vervack, Jr., R. J., Wentzel, T. M., 1993. The distribution of hydrocarbons in Neptune’s upper atmosphere. *Icarus* 104, 38–59.
- Yelle, R. V., Miller, S., 2004. Jupiter’s thermosphere and ionosphere. In: Bagenal, F., McKinnon, W., Dowling, T. (Eds.), *Jupiter: Planet, Satellites and Magnetosphere*. Cambridge University Press, pp. 185–218.
- Yelle, R. V., Young, L. A., Vervack, Jr., R. J., Young, R., Pfister, L., Sandel, B. R., 1996. The structure of Jupiter’s upper atmosphere: Predictions for Galileo. *J. Geophys. Res.* 101, 2149–2161.
- Zelikoff, M., Watanabe, K., 1953. Absorption coefficients of ethylene in the vacuum ultraviolet. *J. Opt. Soc. Am.* 43, 756–759.